Learning Rate Transfer and Feature Learning Across Depth for Constrained Spectral Optimizers: Complete Scion

Eline Pot *eline.pot@centralesupelec.fr*
CVN CentraleSupélec, 91190 Gif-sur-Yvette, France
Framatome, 92400 Courbevoie, France

Laurent Lefebvre *laurent.lefebvre@framatome.com*
Framatome, 92400 Courbevoie, France

Mathieu Segond *mathieu.segond@framatome.com*
Framatome, 92400 Courbevoie, France

Antonio Silveti-Falls *antonio.silveti-falls@centralesupelec.fr*
CVN CentraleSupélec, 91190 Gif-sur-Yvette, France

Reviewed on OpenReview: *https://openreview.net/forum?id=TGiJpGVPNA*

arXiv:2611.15291v1 [cs.LG] 11 Nov 2026

Abstract

Hyperparameter transfer across model depth is instrumental in training deep models, as it enables learning rates calibrated on shallow networks to be effectively applied to deeper architectures. The recent CompleteP framework establishes a $1/L$ residual scaling rule that demonstrates this for Adam-family optimizers. We study whether similar transfer extends to constrained optimization methods, specifically Frank-Wolfe and projected non-Euclidean normalized steepest descent, where updates are determined by linear minimization oracles. We derive scaling rules for these methods which confirm that the $1/L$ residual scaling applies, although the arguments differ from the Adam-family optimizers. Our analysis supports depth-wise transfer and width-wise transfer of the learning rate for the Scion algorithm while ensuring feature learning and avoiding the kernel-regime. In experiments on NLP transformers (nanoGPT on FineWeb), vision transformers (DeiT on ImageNet), and vision MLPs (MLP-Mixer on CIFAR-10), we observe learning rate transfer across depth and feature learning for appropriately chosen residual scaling [1].

1 Introduction

Since their successful use in ImageNet (Krizhevsky et al., 2012), deep neural networks have been increasingly used in complex tasks such as image classification (Simonyan & Zisserman, 2014; He et al., 2016; Szegedy et al., 2015), speech recognition (Hinton et al., 2012; Graves et al., 2013; Amodei et al., 2016), and natural language processing (Sutskever et al., 2014; Vaswani et al., 2017; Devlin et al., 2019), where they have led to significant performance gains across benchmarks and applications. They are deployed for both difficult and critical applications, including medicine (Esteva et al., 2017; Topol, 2019), aeronautics (Julian & Kochenderfer, 2019; Sun & Wang, 2019), and nuclear engineering (Tang et al., 2022; Hu et al., 2021). Performance on complex tasks has been observed to increase with model scale, motivating the use of larger and heavier neural architectures, involving a high number of parameters.

There are many ways to scale deep neural networks, with the most common being increasing its width or depth. However, increased performance is not the only consequence of scale. Indeed, as the scale increases

[1] The code is available at `https://github.com/elinepot/CompleteSCION`.

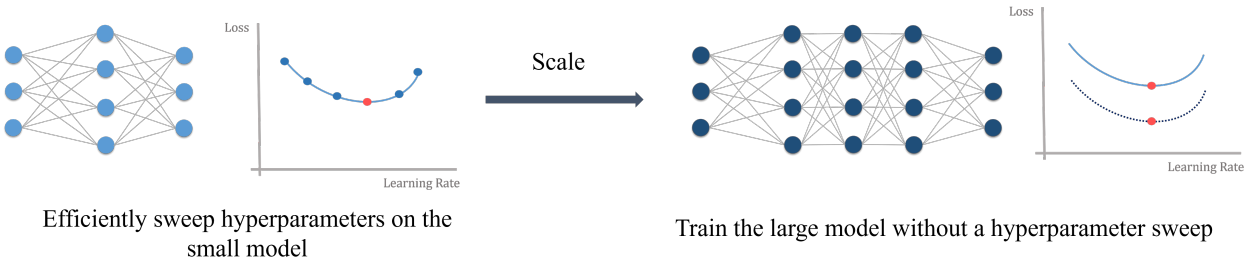


Figure 1: Practical learning rate transfer (Yang et al., 2021). Define a small, computationally inexpensive version of the model (i.e. with small dimensions) and run a hyperparameter sweep to find the optimal learning rate γ^*. Then, train the large-scale target model directly using the optimal γ^*, bypassing expensive tuning at scale.

so does the cost of training and tuning the models, making the ability to reuse hyperparameters across scales a pressing practical concern.

The Maximal Update Parametrization (μP) framework (Yang & Hu, 2021; Yang & Littwin, 2023) provides techniques to ensure that optimal hyperparameters remain invariant when the width of the model increases. This allows optimal hyperparameters found by tuning small scale models to be reliably transferred to larger ones. Figure 1 provides practitioners a step-by-step framework for implementing and using the learning rate transfer. A well-designed parametrization guarantees that the optimal hyperparameter remains invariant across scales. Additionally, μP prescribes parameter and learning-rate scalings that preserve non-degenerate feature learning dynamics, in which the internal representations evolve to fit the data (Yang & Hu, 2021). This avoids the lazy training regime where the model dynamics behave like their linearization (Chizat et al., 2019). However, the optimizer landscape has evolved significantly beyond the Stochastic Gradient Descent (SGD) and Adam (Kingma & Ba, 2014) updates originally considered in μP, leaving a gap.

Despite being introduced more than ten years ago (Carlson et al., 2015a;b;c), optimizers based on the spectral norm have recently reemerged as strong alternatives to standard coordinate-wise methods. In particular, Scion (Pethick et al., 2025b) (which also has an unconstrained variant) is a Conditional-Gradient-based algorithm (Frank & Wolfe, 1956) that relies on a Linear Minimization Oracle (LMO) over norm-ball constraints and explores the choice of a norm across layers. Varying the norm at each layer induces layer-wise update magnitudes, which control the relative update scales between layers. Updates based on the spectral norm have also attracted attention through their use in the Muon optimizer (Jordan et al., 2024b), which has gained popularity due to its performance in speed-running benchmarks (Jordan et al., 2024a) and training industrial-scale large language models like the Kimi, DeepSeek, and the Trinity series models (Kimi Team et al., 2025; 2026a; DeepSeek-AI, 2026; Singh et al., 2026). Unlike SGD or Adam, these methods precondition the update to weight matrices in a layer-wise manner using matrix-level operations such as the matrix sign, rather than using coordinate-wise scaling. As a result, the update structure is fundamentally different, meaning that the standard μP parametrization and the Tensor Programs (TP) analytic framework (Yang & Hu, 2021; Yang et al., 2023b) do not directly apply.

While μP provides a principled framework for width-wise hyperparameter transfer, it does not directly address the effect of increasing depth. Several extensions have explored depth-wise hyperparameter transfer (Yang et al., 2023b; Bordelon et al., 2024b; Dey et al., 2026; Qiu et al., 2025). Among them, CompleteP (Dey et al., 2026) identifies three desiderata that enable joint width-and-depth-wise transfer: stable initialization, maximal feature updates, and a layer-wise non-lazy training regime. The lazy regime, related to the Neural Tangent Kernel regime, is one where features evolve like their linearization with respect to the parameters during training (Yang et al., 2021; Dey et al., 2026). However, existing instantiations of CompleteP focus on SGD-like optimizers and do not cover spectral-norm-based update rules.

In this work, we study the compatibility of the CompleteP parametrization with Scion, referring to their combination as Complete Scion, and show that it satisfies all the desiderata outlined in CompleteP. More precisely, we show that the learning rate tuned at small scale transfers to larger models without additional

tuning, assuming a residual scaling of the form $L^{-\alpha}$ with $\alpha \in [1/2, 1]$ and a learning rate scaled as $\gamma \propto L^{\alpha-1}$, for both Scion and Unconstrained Scion.

Our theoretical analysis establishes both width-wise and depth-wise hyperparameter transfer. For depth scaling, we confirm that the CompleteP desiderata (stable initialization and stable feature updates) hold for Scion and Unconstrained Scion, establishing depth-wise learning rate transfer. We show that stable feature updates are achieved in the $\alpha = 1$ regime. We emphasize that, while our final optimization objectives align with the CompleteP framework, our derivations and proofs differ.

Existing analyses in CompleteP focus on well-normalized coordinate-wise optimization methods such as Adam, whose updates are applied independently across parameters. In contrast, we focus on spectral optimizers like Scion, which compute geometry-aware updates that are not regularized coordinate-wise, instead using linear minimization oracles over matrix-norm-ball constraints. As a consequence, the analytical techniques developed for coordinate-wise optimizers do not directly apply, and establishing depth-wise hyperparameter transfer requires a different derivation adapted to constrained and unconstrained spectral optimization.

For width scaling, we prove that the optimal learning rate is independent of hidden-layer width for Scion (with weight decay), extending prior width-transfer results (Pethick et al., 2025b; Yang et al., 2023a) to the constrained spectral setting. Finally, we consider a variant of Scion which proposes to constrain the weights to be in a spectral ball or Stiefel manifold by using spectral clipping. We observe in our experiments that this projected version admits width-transfer.

We empirically validate these theoretical depth-wise and width-wise hyperparameter transfer results and the feature learning in multiple experiments across both vision and language tasks. Learning rate transfer experiments on transformers (nanoGPT (Karpathy, 2023) trained on FineWeb, and DeiT (Touvron et al., 2021) on ImageNet) and on MLPs (MLP-Mixer (Tolstikhin et al., 2021) trained on CIFAR-10) show that hyperparameters tuned at small width and depth successfully transfer to larger models.

From a practical standpoint, by enabling principled width and depth-wise hyperparameter transfer, our results make these spectral-norm-based optimizers significantly cheaper to tune, in the same way that μP enabled practical scaling for Adam and SGD related optimization methods.

We summarize our contributions as follows:

- We confirm that the CompleteP desiderata (stable initialization and stable feature updates) hold for Scion and Unconstrained Scion, under the $L^{-\alpha}$ residual scaling ($\alpha \in \{1/2, 1\}$) with an appropriately scaled learning rate $\gamma \propto L^{\alpha-1}$, establishing depth-wise learning rate transfer. Our analysis is tailored to updates that take matrix structure into account, which are not addressed by the coordinate-wise analyses used in existing CompleteP formulations.
- We prove width-wise hyperparameter transfer for Scion (with weight decay) and we empirically show it for Spectral Clipping, extending the width-transfer results of Pethick et al. (2025b); Yang et al. (2023a) to the constrained setting.
- We give practitioners a guide to tune layer-wise scale, and empirically validate the theoretical depth-wise and width-wise hyperparameter transfer results, as well as complete feature learning ($\alpha = 1$ vs. $\alpha = 1/2$), on both transformers (modded nanoGPT on FineWeb, and DeiT on ImageNet) and MLPs (MLP-Mixer on CIFAR-10) across vision and language datasets.

2 Related Work

Width-wise hyperparameter transfer The Maximal Update Parametrization (μP) (Yang & Hu, 2021; Yang & Littwin, 2023) initiated the Tensor Programs framework for hyperparameter transfer that determines how hyperparameters such as the learning rate or the initialization should vary with the model width going to infinity, ensuring that each layer exhibits stable learning and meaningful features (maximal feature learning). μP enables optimal hyperparameters tuned on a narrow model to transfer to wider models. This line of work

established that width-wise hyperparameter transfer is well understood for coordinate-wise optimizers such as SGD and Adam, and inspired further analyses for width scaling (Yang et al., 2021; 2023a; Bordelon & Pehlevan, 2022; Vankadara et al., 2024).

Kosson et al. (2025) study learning-rate transfer for Adam under μP, showing that the geometric alignment assumptions underlying μP hold only briefly at the start of training in practical large-scale settings. They demonstrate that for Adam, it is instead independent weight decay that stabilizes representation updates across widths for most of training, reframing μP's effect as an implicit learning-rate warmup.

Despite these refinements, works building on the μP framework focus on coordinate-wise update structures and do not directly cover spectral-norm-based optimization methods. More recent analyses have begun extending width-scaling to operator norm optimizers (Pethick et al., 2025a; Xu et al., 2026), but do not address the depth-wise feature-learning framework studied in this paper.

Depth-wise hyperparameter transfer This idea has been extended, both in the Tensor Programs framework and beyond, to depth scaling for residual networks (Yang et al., 2023b; Bordelon et al., 2024b; Dey et al., 2026; Qiu et al., 2025). The insight behind these works is to scale the residual branch by a factor $L^{-\alpha}$ that depends on the depth L of the network, with $\alpha \in [1/2, 1]$, and to scale the learning rate accordingly.

More recently, CompleteP (Dey et al., 2026) formalized depth-wise hyperparameter transfer by introducing three desiderata: stable initialization, stable feature updates, and a non-lazy training regime. Within this framework, CompleteP shows that $\alpha = 1$ ensures complete feature learning and improved performance compared to $\alpha = 1/2$ for Adam-based optimizers.[2] While CompleteP provides a general conceptual framework, its concrete instantiations and proofs focus on SGD-like update rules, leaving open the question of whether these desiderata can be satisfied by optimizers with fundamentally different update structures.

Shigida et al. (2026) focus on the nGPT framework, restricting the model to a narrow class of architectures, and demonstrate learning rate transfer across both model dimension and token horizon. Ren et al. (2026) constrain the model by design and implement a variant of μP using Frobenius norms for hypersphere parametrization. Utilizing the Muon optimizer under this Frobenius-sphere constraint, they achieve learning rate transfer across model width, depth, and training tokens by modifying the parametrization of the network itself. In contrast, we operate in a more general setting, with constraints guaranteed through the optimization.

Zheng et al. (2026) study width-depth scaling in the μP setting from a spectral-condition perspective. In contrast, our work focuses on extending CompleteP-style depth-wise transfer to Scion and Unconstrained Scion, i.e. to a different optimizer class with geometry-aware spectral updates.

Our work builds on the CompleteP framework and instantiates it for a new family of optimizers. We adopt the same architectural setting and depth-dependent residual scaling, but study a different update rule based on Scion. We show that, under appropriate scaling, both Scion and Unconstrained Scion satisfy the CompleteP desiderata, and we provide new proofs tailored to Scion 's update dynamics. In this sense, our contribution extends CompleteP to a broader class of optimization methods.

Spectral-norm and geometry-based optimizers. A parallel line of work studies optimization methods that incorporate geometric or spectral information into their updates. Shampoo (Gupta et al., 2018) introduces a tensor-wise preconditioning method, based on Kronecker-factored matrices. Shampoo uses these preconditioning matrices to whiten features along the left and right dimensions of the weight matrices. This significantly reduces the memory and computational cost compared to storing the full Hessian matrices at large scale. SOAP (Vyas et al., 2025) extends Shampoo by combining tensor-structured preconditioning with Adam updates. It applies on-the-fly adaptive updates in the eigen-basis of the Kronecker preconditioner matrices (Pethick et al., 2025a), improving the stability and reducing the computational cost of the training while preserving the scaling ability of Shampoo. In this work, we focus specifically on instant versions via LMO, noting that methods like Scion operate precisely as instant Shampoo.

[2]The authors of Dey et al. (2026) argue that their results extend to any "well-normed" optimizer, and provide explicit derivations for SignSGD.

Spectral-norm-based optimizers constitute a distinct and increasingly popular class. Muon (Jordan et al., 2024b) combines SGD with momentum and matrix normalization using Newton–Schulz iterations to produce orthogonal updates. The orthogonalization prevents updates from being dominated by a few directions, resulting in more balanced and robust training dynamics. Muon demonstrates rapid convergence and strong performances on large-scale deep learning tasks, including a speed record on CIFAR-10.

Recent work (Filatov et al., 2026) has also emphasized that the operator norm used for the last layer is fundamental to the scaling behavior in Scion. Filatov et al. (2026) study scaling across both architecture and dataset with $\alpha = 1$. Our work complements this perspective by analyzing the effect of α on both the scaling and feature learning aspects of Scion. Similar to their work, we provide empirical results in Section 5 showing transfer of the layerwise learning rates as well.

Scion (Pethick et al., 2025b) is a Conditional Gradient algorithm that utilizes the LMO subject to norm-ball constraints, allowing for choice of layer-wise norms. From this perspective, Scion plays a role for sign-based optimization (Riedmiller & Braun, 1993) analogous to that of Shampoo for Adam. Indeed, as Shampoo enriches Adam with structured matrix preconditioning, Scion augments sign updates with explicit and more general geometric constraints. Scion provides a unified framework on existing methods such as Muon (Jordan et al., 2024b), SignSGD (Bernstein et al., 2018) and NormalizedSGD (Hazan et al., 2015), that arise as special cases of unconstrained Stochastic Conditional Gradient under different norms (the spectral, the max-, and the Euclidean L_2 norms, respectively). Thus, Scion covers a broad family of geometric-aware methods, and has been implemented in the NVIDIA NeMo Emerging Optimizers library (NVIDIA NeMo Team, 2025).

Closest to this setting is the Modular Norm framework (Large et al., 2024), which establishes width-wise and depth-wise hyperparameter transfer using layer-wise normalized SGD. This direction was further developed and analyzed using linear minimization oracles in Pethick et al. (2025b), which proves width-wise transfer for Unconstrained Scion and serves as the primary foundation for our analysis. We highlight two important aspects that distinguish our work from Large et al. (2024). First, we study the Scion framework based on linear minimization oracles rather than layer-wise normalized SGD given in Large et al. (2024); the update directions in Scion are fundamentally different. Second, we study the effect of α beyond $\alpha = 1$ on both hyperparameter transfer and feature learning.

Relatedly, Qiu et al. (2025) study the width and depth scaling of the learning rate and the weight decay for matrix-preconditioned optimizers such as Shampoo, SOAP, and Muon+AdamW. They do not consider α besides $\alpha = 1$ and focus also on scaling the dataset size; in contrast, we are concerned with constrained optimizers, and the effect of α on their feature learning.

Additionally, Islamov et al. (2026) analyze hyperparameter scaling from a data-budget perspective, establishing principled rules for scaling the batch size, sequence length, and step size specifically for stochastic conditional gradient methods like Scion.

3 Complete Scion

We first restate the desiderata required for effective feature learning and hyperparameter transfer. We then show that these desiderata are satisfied by Scion, both in its constrained and unconstrained forms.

3.1 Optimization problem

We consider training a neural network with L hidden layers. We denote the full set of model parameters as $\mathbf{\Theta} = \{\theta^{(0)}, \theta^{(1)}, \ldots, \theta^{(L+1)}\}$, where each $\theta^{(\ell)}, \ell \in \{0, \ldots, L+1\}$ represents the parameters specific to layer ℓ. Each $\theta^{(\ell)} = (\theta^{(\ell,k)})_k$ collects all the parameters of the layer ℓ. The training goal is to minimize the loss $\mathcal{L}(\mathbf{\Theta})$, formulated as

$$\min_{\mathbf{\Theta} \in \mathcal{X}} \mathcal{L}(\mathbf{\Theta}) \tag{1}$$

where $\mathcal{X}$ represents the parameter set, that is either unconstrained (full parameter space) or constrained to $\mathcal{X} = \mathcal{D}$. We denote the partial gradient with respect to the ℓ-th layer parameters as $\nabla_{\theta^{(\ell)}} \mathcal{L}(\mathbf{\Theta})$. The

dependence on the full family of parameters $\mathbf{\Theta}$ will be implicit in the remainder of the paper, and we will simply write $\nabla_{\theta^{(\ell)}}\mathcal{L}$ and omit the dependence on $\mathbf{\Theta}$.

In contrast to many prior works on hyperparameter transfer, we will not always assume $\mathcal{X}$ is the full parameter space, instead allowing for some constraint set $\mathcal{D}$ which is defined as the Cartesian product of layer-wise norm-balls with radii $\{\rho^{(0)}, \ldots, \rho^{(L+1)}\}$, each constraining all parameter blocks of the corresponding layer.

$$\mathcal{D} = \prod_{\ell=0}^{L+1} \{\theta^{(\ell)} : \|\theta^{(\ell,k)}\| \leq \rho^{(\ell,k)}, \forall k\}. \tag{2}$$

There are two main ways to enforce these constraints: projection-based methods and Conditional-Gradient–type updates (Frank & Wolfe, 1956). In Conditional Gradient methods, each update is constructed as a convex combination of the current iterate and a point on the constraint set, ensuring that iterates remain within the feasible region. In contrast, projected gradient methods first take an unconstrained update step and then project the result back onto the constraint set at each iteration. An illustration of these two types of iterations can be found in Figure 2. In the next part, we detail the Stochastic version of Conditional Gradient, and the associated optimizer Scion.

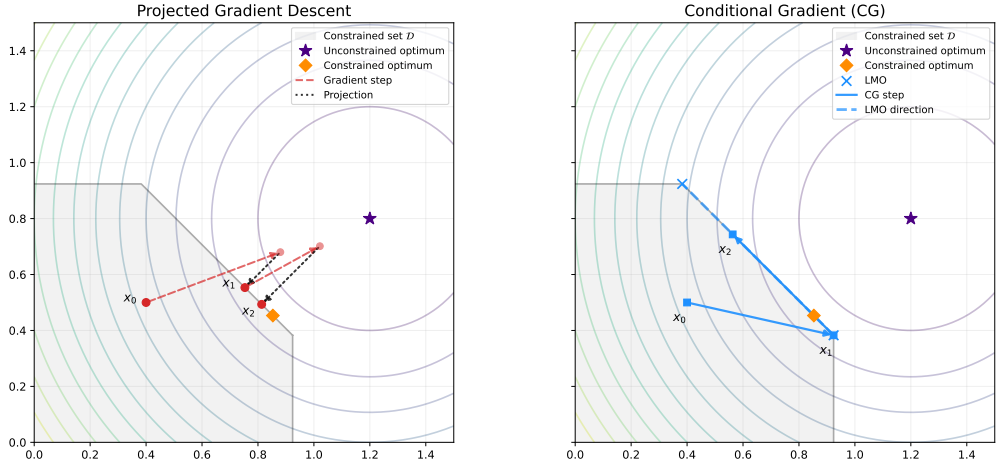


Figure 2: Projected gradient methods step outside the feasible set and then project back to the border of the constraint set, whereas Conditional Gradient methods preserve feasibility by updating through convex combinations with decreasing step sizes.

3.2 Scion and Unconstrained Scion

Scion is a stochastic optimization framework based on the Stochastic Conditional Gradient (SCG), and its unconstrained version (uSCG), presented in Algorithms 1 and 2, respectively. In uSCG, the parameters θ are optimized over an unconstrained parameter space denoted $\mathcal{X}$, as opposed to the constrained feasible set denoted $\mathcal{D}$ used in Scion. Importantly, the use of weight decay can be interpreted within this framework as an instance of constrained version, Scion, where the decay implicitly enforces norm-ball constraints on the parameters, as discussed in Pethick et al. (2025b;a).

SCG is classically used for constrained optimization problems as it ensures the iterates remain in a ball of constant norm. These algorithms adapt the geometry to the problem by using norm-constrained Linear Minimization Oracles (LMOs). The lmo is applied on the gradient, and its output minimizes a linear approximation to the function $\mathcal{L}$ we want to minimize under the norm-ball constraint set $\mathcal{D}$

$$\text{lmo}(\nabla_{\theta^{(\ell)}}\mathcal{L}) \in \arg\min_{\nu \in \mathcal{D}} \langle \nabla_{\theta^{(\ell)}}\mathcal{L}, \nu \rangle. \tag{3}$$

Algorithm 1 SCG

Input: Horizon n, initialization $\mathbf{\Theta}_1 \in \mathcal{D}$, $M_0 = 0$, momentum $\beta_t \in [0, 1)$, and stepsize $\gamma_t \in (0, 1)$

for $t = 1, \ldots, n$ **do**
  Sample data $x \sim \mathcal{P}$
  $M_t \leftarrow (1 - \beta_t)\nabla_{\mathbf{\Theta}_t}\mathcal{L} + \beta_t M_{t-1}$
  $\mathbf{\Theta}_{t+1} \leftarrow (1 - \gamma_t)\mathbf{\Theta}_t + \gamma_t \operatorname{lmo}(M_t)$
end for

Algorithm 2 Unconstrained SCG (uSCG)

Input: Horizon n, initialization $\mathbf{\Theta}_1 \in \mathcal{X}$, $M_0 = 0$, momentum $\beta_t \in [0, 1)$, and stepsize $\gamma_t \in (0, 1)$

for $t = 1, \ldots, n$ **do**
  Sample data $x \sim \mathcal{P}$
  $M_t \leftarrow (1 - \beta_t)\nabla_{\mathbf{\Theta}_t}\mathcal{L} + \beta_t M_{t-1}$
  $\mathbf{\Theta}_{t+1} \leftarrow \mathbf{\Theta}_t + \gamma_t \operatorname{lmo}(M_t)$
end for

We note that the lmo provides only the direction of the constrained steepest gradient descent. It does not give a step size or define the next iterate. Also, it is scale invariant: $\operatorname{lmo}(\mu s) = \operatorname{lmo}(s)$ for any $\mu > 0$.

Scion instantiates SCG and uSCG using layer-wise operator norms, resulting in the constrained variant (Scion) and the unconstrained variant (Unconstrained Scion), respectively. By choosing the norm based on the architecture to be optimized, Scion aligns the optimization direction with the model's structure, leading to faster and more efficient training, especially for large neural networks. Update rules, associated LMOs, and per-layer learning rate scales are provided in Table 1 for typical configurations. Specific examples of the Unconstrained Scion step and its layer-wise learning rate scales can be found in Equation (4) and Equation (5).

For instance, considering a one-step Unconstrained Scion update with a `Sign` $\to$ `Spectral` $\to$ `Sign` configuration for a 1-layer MLP with parameters $\{W^{(0)}, W^{(1)}, W^{(2)}\}$, the iterates at the iteration $t+1$ are given by:

$$
\begin{aligned}
\begin{bmatrix} W_{t+1}^{(0)} \\ W_{t+1}^{(1)} \\ W_{t+1}^{(2)} \end{bmatrix} &= \begin{bmatrix} W_t^{(0)} \\ W_t^{(1)} \\ W_t^{(2)} \end{bmatrix} + \gamma_t \operatorname{lmo}\left(\begin{bmatrix} M_t^{(0)} \\ M_t^{(1)} \\ M_t^{(2)} \end{bmatrix} \right) && \text{(by definition of Unconstrained Scion)} \\
&= \begin{bmatrix} W_t^{(0)} \\ W_t^{(1)} \\ W_t^{(2)} \end{bmatrix} + \gamma_t \begin{bmatrix} \operatorname{lmo}_{\|\cdot\|_{\mathrm{Sign}}}\left(M_t^{(0)}\right) \\ \operatorname{lmo}_{\|\cdot\|_{\mathcal{S}_\infty}}\left(M_t^{(1)}\right) \\ \operatorname{lmo}_{\|\cdot\|_{\mathrm{Sign}}}\left(M_t^{(2)}\right) \end{bmatrix} && \text{(the lmo is separable)} \\
&= \begin{bmatrix} W_t^{(0)} \\ W_t^{(1)} \\ W_t^{(2)} \end{bmatrix} - \gamma_t \begin{bmatrix} \rho_0\left(\frac{1}{d_{\text{in}}} \operatorname{sign}\left(M_t^{(0)}\right)\right) \\ \rho_1\left(\sqrt{\frac{d_1}{d_0}} \operatorname{orthog}\left(M_t^{(1)}\right)\right) \\ \rho_2\left(\frac{1}{d_1} \operatorname{sign}\left(M_t^{(2)}\right)\right) \end{bmatrix} && \text{(compute the LMOs with the layerwise radii)}
\end{aligned}
\tag{4}
$$

where we used the separability of the lmo for the max norm $\|\mathbf{\Theta}\| = \max_\ell\{\|\theta^{(\ell)}\|_\ell\}$.

Then, the difference between iteration $t+1$ and t for each layer ℓ, denoted $\Delta W^{(\ell)}$ can be expressed as:

$$
\begin{aligned}
\Delta W^{(0)} &= \gamma_t \operatorname{lmo}_{\|\cdot\|_{\mathrm{Sign}}}(M_t^{(0)}) = -\gamma_t \rho_0 \left(\frac{1}{d_{\text{in}}} \operatorname{sign}\left(M_t^{(0)}\right)\right) \\
\Delta W^{(1)} &= \gamma_t \operatorname{lmo}_{\|\cdot\|_{\mathcal{S}_\infty}}(M_t^{(1)}) = -\gamma_t \rho_1 \left(\sqrt{\frac{d_1}{d_0}} \operatorname{orthog}\left(M_t^{(1)}\right)\right) \\
\Delta W^{(2)} &= \gamma_t \operatorname{lmo}_{\|\cdot\|_{\mathrm{Sign}}}(M_t^{(2)}) = -\gamma_t \rho_2 \left(\frac{1}{d_1} \operatorname{sign}\left(M_t^{(2)}\right)\right).
\end{aligned}
\tag{5}
$$

Table 1: Update rules and learning rate (LR) scaling for different architectural layers. This example utilizes the norm configuration `Sign` $\to$ `Spectral` $\to$ `Sign` for the embedding, hidden, and un-embedding layers, respectively. We provide the specific operator norms and associated lmo applied to the average gradient $M^{(\ell)}$, whose reduced Singular Value Decomposition (SVD) is denoted $M^{(\ell)} = U^{(\ell)}\Sigma^{(\ell)}V^{(\ell)\top}$ for all layers ℓ. The parameters ρ_e, ρ_h, and ρ_u designate the radii of the balls for the embedding, hidden, and un-embedding weights respectively. Following Recommendation 3.1 of Pethick et al. (2025b), typical configurations include `Spectral` $\to$ `Spectral` $\to$ `Sign` for image data, or `ColNorm` $\to$ `Spectral` $\to$ `Sign` for 1-hot inputs. For an exhaustive list of norms and associated LMOs, one can refer to Pethick et al. (2025b;a).

	Embedding ($\ell = 0$)	$\to$	**Hidden Layers** ($\ell \in [1, L]$)	$\to$	**Un-embedding** ($\ell = L+1$)
Norm $\|\cdot\|$	$\|\cdot\|_{\text{Sign}}$		$\|\cdot\|_{\mathcal{S}_\infty}$		$\|\cdot\|_{\text{Sign}}$
LMO $\text{lmo}(M^{(\ell)})$	$-\rho_e \frac{1}{d_{\text{in}}}\text{sign}(M^{(0)})$		$-\rho_h \sqrt{\frac{d_\ell}{d_{\ell-1}}} U^{(\ell)}V^{(\ell)\top}$		$-\rho_u \frac{1}{d_L}\text{sign}(M^{(L+1)})$
Scaled LR γ_ℓ	γ_{base}		$L^{\alpha-1}\gamma_{\text{base}}$		γ_{base}
Unconstrained Scion Update $\Delta W^{(\ell)} = \gamma_\ell \,\text{lmo}(M^{(\ell)})$	$-\gamma_0\rho_e \frac{1}{d_{\text{in}}}\text{sign}(M^{(0)})$		$-\gamma_\ell\rho_h \sqrt{\frac{d_\ell}{d_{\ell-1}}} U^{(\ell)}V^{(\ell)\top}$		$-\gamma_{L+1}\rho_u \frac{1}{d_L}\text{sign}(M^{(L+1)})$
Scion Update $\Delta W^{(\ell)} = \gamma_\ell(\text{lmo}(M^{(\ell)}) - W^{(\ell)})$	$-\gamma_0(\rho_e \frac{1}{d_{\text{in}}}\text{sign}(M^{(0)}) + W^{(0)})$		$-\gamma_\ell(\rho_h \sqrt{\frac{d_\ell}{d_{\ell-1}}} U^{(\ell)}V^{(\ell)\top} + W^{(\ell)})$		$-\gamma_{L+1}(\rho_u \frac{1}{d_L}\text{sign}(M^{(L+1)}) + W^{(L+1)})$

3.3 Conditions for Depth-wise Transfer

Setup In this section, we consider a residual architecture of depth L, defined as

$$\begin{aligned} h^{(0)} &= W^{(0)}x \\ h^{(\ell)} &= Z^{(\ell)}h^{(\ell-1)} + L^{-\alpha}\mathcal{F}_\ell(h^{(\ell-1)};\theta_{\mathcal{F}}^{(\ell)}) \quad (\forall \ell \in \{1,\dots,L\}) \\ f &= W^{(L+1)}\phi(h^{(L)}), \end{aligned} \tag{6}$$

where $x \in \mathbb{R}^{d_{\text{in}}}$ are the input data, $h^{(\ell)} \in \mathbb{R}^{d_\ell}, \ell \in \{0,\dots,L\}$ are the hidden states, $Z^{(\ell)} \in \mathbb{R}^{d_\ell \times d_{\ell-1}}$, and $f \in \mathbb{R}^{d_{\text{out}}}$ is the output after nonlinear activation ϕ. The embedding and un-embedding matrices are respectively $W^{(0)} \in \mathbb{R}^{d_0 \times d_{\text{in}}}$ and $W^{(L+1)} \in \mathbb{R}^{d_{\text{out}} \times d_L}$. The residual block $\mathcal{F}_\ell(h^{(\ell-1)};\theta_{\mathcal{F}}^{(\ell)}), \ell \in \{1,\dots,L\}$ can be an attention block, or an MLP (cf. Figure 3), and $\theta_{\mathcal{F}}^{(\ell)}$ is its trainable parameter. Following the notation introduced in Section 3.1, the parameters for the hidden layer ℓ are represented by the set $\theta^{(\ell)} = \{Z^{(\ell)}, \theta_{\mathcal{F}}^{(\ell)}\}$, and the parameters for the embedding and un-embedding layers are represented by $\theta^{(0)} = \{W^{(0)}\}$ and $\theta^{(L+1)} = \{W^{(L+1)}\}$ respectively.

Essentially, the residual branch is scaled with a depth-dependent factor $L^{-\alpha}$, where the exponent α dictates how the contribution of each residual block scales as the total depth L grows. This parametrization follows the framework of Tensor Programs and infinite-depth limits (Yang et al., 2023b; Bordelon et al., 2024b).

The choice $\alpha = 1/2$ corresponds to the μP regime studied in Tensor Programs, where the cumulative contribution of the residual stream remains non-trivial in the infinite-depth limit and feature learning is preserved (Yang et al., 2023b; 2021; Bordelon et al., 2024a).

Conversely, recent work suggests advantages for linear scaling. Indeed, Dey et al. (2026) argue that $\alpha = 1$ is the only value that enables stable training, maximal updates and feature learning at infinite dimensions.

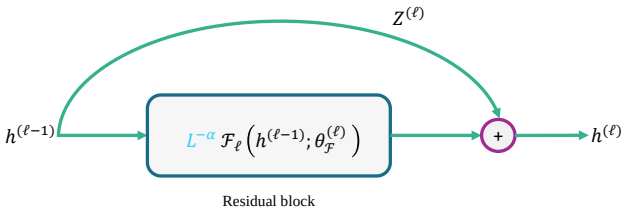


Figure 3: Residual block mechanism with depth-wise scaling $L^{-\alpha}$.

CompleteP (Dey et al., 2026) defines three desiderata, that provide a principled framework for understanding why this parametrization works, and what criteria the parametrization should respect in order to observe hyper-parameter transfer both in width and depth, as well as non-lazy learning.

Following the literature (Dey et al., 2026; Qiu et al., 2025; Zheng et al., 2026), we enumerate the desiderata for depth-scaling below.

Notation In the analysis, we will use the following notation:

$$\begin{aligned}
f(n) = \Theta(g(n)) &\iff \left(\exists\, (c, C) \in (0, +\infty)^2\right) \quad cg(n) \leq f(n) \leq Cg(n) \quad \text{as } n \to \infty, \\
f(n) = \mathcal{O}(g(n)) &\iff \left(\exists\, C \in (0, +\infty)\right) \quad f(n) \leq Cg(n) \quad \text{as } n \to \infty, \\
f(n) = \Omega(g(n)) &\iff \left(\exists\, c \in (0, +\infty)\right) \quad cg(n) \leq f(n) \quad \text{as } n \to \infty.
\end{aligned}$$

Note that the notation $\Theta()$ is different from the full parameter set mentioned in the previous subsections and written in bold as $\boldsymbol{\Theta}$.

We will also use $\|\cdot\|_2$ and $\|\cdot\|_{\mathcal{S}_\infty}$ to denote the Euclidean norm and the spectral norm, respectively.

Desideratum 1 (Stable Initialization)**.** *The hidden layers and the output remain stable (preventing signals from exploding or vanishing as they pass through many layers) at the initialization when L and d_ℓ become increasingly large:*

$$(\forall \ell \in \{1, \dots, L\}) \;\; \frac{1}{d_\ell} \|h^{(\ell)}\|_2^2 \in \Theta(1) \;\; \textit{and} \;\; \|f\|_2^2 \in \mathcal{O}(1), \quad \textit{as} \;\; d_\ell \to \infty, L \to \infty. \tag{7}$$

This property indicates how to adjust the variance of the initialization of the weights. In Dey et al. (2026), it is highlighted that this imposes $\alpha \geq \frac{1}{2}$, since otherwise the residual stream variance diverges when the depth is scaled.

Desideratum 2 (Stable Feature Update)**.** [3] *The weights of each residual block should contribute with order $1/L$ to feature movements, and each non-residual block should contribute with constant order (i.e. each non-residual block has a meaningful impact on the residual stream):*

$$\begin{aligned}
&\frac{1}{\sqrt{d_\ell}} \|\Delta_{\theta_{\mathcal{F}}^{(\ell)}, Z^{(\ell)}} h^{(\ell)}\|_2 \in \Theta\left(\frac{1}{L}\right) \quad (\forall \ell \in \{1, \dots, L\}), \\
&\frac{1}{\sqrt{d_0}} \|\Delta W^{(0)} x\|_2 \in \Theta(1), \\
&\frac{1}{\sqrt{d_{\text{out}}}} \|\Delta W^{(L+1)} h^{(L)}\|_2 \in \Theta(1),
\end{aligned} \tag{8}$$

where Δ designates the variation of the parameters between two successive iterations.

This criterion is the same as the maximal update condition when L is a fixed constant, since we have $\Theta(1/L) = \Theta(1)$ with respect to width-scaling (Yang & Hu, 2021; Yang et al., 2023a). Moreover, Dey et al. (2026) show that this criterion imposes $\alpha \leq 1$, a result also proven in Yang et al. (2023b).

As we shall see in the next subsections, the first and second desiderata can be guaranteed to be satisfied by Scion and Unconstrained Scion for any $\alpha \in [1/2, 1]$, under the condition that the learning rates, γ and γ_Z, used to optimize the parameters $\{\theta_{\mathcal{F}}^{(\ell)}\}_{\ell \in \{1,\dots,L\}}$ and the operators $\{Z^{(\ell)}\}_{\ell \in \{1,\dots,L\}}$, respectively, are scaled as follows:

$$\gamma = \gamma_{\text{base}} L^{\alpha - 1} \quad \text{and} \quad \gamma_Z = \gamma_{Z\,\text{base}} L^{-1}. \tag{9}$$

The learning rates relative to the embedding and un-embedding parameters do not need depth-wise scaling,

$$\gamma_{W^{(0)}} = \gamma_{W^{(0)}\,\text{base}} \quad \text{and} \quad \gamma_{W^{(L+1)}} = \gamma_{W^{(L+1)}\,\text{base}}. \tag{10}$$

[3] The corresponding Desideratum in Dey et al. (2026) has $\frac{1}{d_\ell} \|\Delta_{\theta^{(\ell)}} h^{(\ell)}\|_2^2 = \Theta(\frac{1}{L})$, which slightly differs from ours, as we discuss in Appendix E.

We can interpret this in the unconstrained case as a scale-dependent operator norm that encodes the scaling geometry automatically, so that the optimal learning rate does not change and these scalings are encoded solely in the norm choice. Specifically, the fixed magnitude of the lmo induces a guaranteed bound on the maximum norm of the parameters, ensuring stable scaling.

3.4 Scion and Unconstrained Scion satisfy Desiderata 1 and 2

3.4.1 Fundamental setup

As a simplified model, consider the block $\mathcal{F}_\ell(h^{(\ell-1)}; \theta_{\mathcal{F}}^{(\ell)})$ given by a one-layer MLP, for $\ell \in \{1, \dots, L\}$, that is

$$h^{(\ell)} = Z^{(\ell)} h^{(\ell-1)} + L^{-\alpha} W^{(\ell)} \phi(h^{(\ell-1)}) \tag{11}$$

where ϕ is a Lipschitz-continuous activation function. In this case, the trainable parameter of the residual block $\theta_{\mathcal{F}}^{(\ell)}$ is the weight matrix $W^{(\ell)} \in \mathbb{R}^{d_\ell \times d_{\ell-1}}$ for $\ell \in \{1, \dots, L\}$. In our analysis, we consider that the operator matrices applied to the residual stream $Z^{(\ell)} \in \mathbb{R}^{d_\ell \times d_{\ell-1}}$ for $\ell \in \{1, \dots, L\}$, are learned and updated during training. This generalizes the standard identity shortcut to a learnable linear transformation, aligning with recent architectural paradigms that introduce parameterized transformations into the residual path.

For instance, manifold-constrained hyper-connections (mHC) (Xie et al., 2025), which uses the lmo for the Birkhoff polytope, utilizes learnable mixing to mix features in the residual stream, and Kimi Team et al. (2026b) use an attention mechanism over the preceding layer output. In this case, following the notation defined in Section 3.1, the parameters for the hidden layer ℓ are simply the pair of matrices $\theta^{(\ell)} = \{Z^{(\ell)}, W^{(\ell)}\}$, and the parameters for the embedding and un-embedding layers are $\theta^{(0)} = \{W^{(0)}\}$ and $\theta^{(L+1)} = \{W^{(L+1)}\}$, respectively. In our analysis, we omit biases, but, in practice, when included they are scaled in the same way as the weight matrices, consistent with Dey et al. (2026).

3.4.2 Modeling assumptions

We focus on the worst-case analysis for a batch size of 1. In practice and in our experiments, large batches are used and the results remain in accordance with our theoretical conclusions.

Initialization As in Pethick et al. (2025b), we suppose we initialize with either a semi-orthogonal or Gaussian matrix, and apply the lmo with the spectral norm for every layer ℓ. We note that using a scaled sign operator norm on the embedding or un-embedding layers is also viable, consistent with the analysis in Dey et al. (2026).

In particular, this leads (with high probability) to

$$\|W^{(\ell)}\|_{\mathcal{S}_\infty} = \Theta\left(\sqrt{\frac{d_\ell}{d_{\ell-1}}}\right) \quad \text{and} \quad \|\Delta W^{(\ell)}\|_{\mathcal{S}_\infty} = \Theta\left(\sqrt{\frac{d_\ell}{d_{\ell-1}}}\right). \tag{12}$$

We suppose the same assumptions apply for the matrices $Z^{(\ell)}, \ell \in \{1, \dots, L\}$.

For technical purposes, we will furthermore assume that the data x follows some distribution $\mathcal{P}$ such that $\|x\|_2 = \Theta(\sqrt{d_{in}})$. This is often the case for images (Yang et al., 2023a) for instance.

Scale of the activation function ϕ We assume that the hidden features $\phi(h^{(\ell)})$ have the same scale before and after the application of the activation function ϕ for all the layers ℓ:

$$\|\phi(h^{(\ell)})\|_2 = \Theta(\|h^{(\ell)}\|_2). \tag{13}$$

It is the same assumption as in the Assumption 2 of Yang et al. (2023a). This behavior is typical for most activation functions since they are designed to operate on inputs of order one and produce outputs that neither blow up nor collapse.

Alignment of weight matrices We assume that, for any step t, for all layers ℓ, we have

$$\begin{aligned} \|W^{(\ell)}\phi(h^{(\ell-1)})\|_2^2 &= \Theta(\|W^{(\ell)}\|_{\mathcal{S}_\infty}^2 \|\phi(h^{(\ell-1)})\|_2^2), \\ \|W^{(\ell)}h^{(\ell-1)}\|_2^2 &= \Theta(\|W^{(\ell)}\|_{\mathcal{S}_\infty}^2 \|h^{(\ell-1)}\|_2^2). \end{aligned} \tag{14}$$

While this modeling assumption is not universally applicable, it has been empirically validated (Yang et al., 2023a) and consistently yields predictive results.

We suppose the same assumptions apply for the matrices $Z^{(\ell)}, \ell \in \{1, \dots, L\}$.

In Figure 26, we empirically verify that this is a reasonable assumption, showing that it holds for various depths and multiple steps.

Non-cancellation assumptions We make the following assumptions on the alignment between updates and the current parameters. For any layer ℓ, and training step t:

1. The addition of the residual block with the previous state does not perfectly cancel.

$$\|h^{(\ell)}\|_2^2 = \Theta\left(\|Z^{(\ell)}h^{(\ell-1)}\|_2^2 + \frac{1}{L^{2\alpha}}\|W^{(\ell)}\phi(h^{(\ell-1)})\|_2^2\right). \tag{15}$$

2. The updates of $Z^{(\ell)}$ and $W^{(\ell)}$ do not perfectly cancel.

$$\|\Delta_{W^{(\ell)},Z^{(\ell)}}h^{(\ell)}\|_2^2 = \Theta\left(\|\Delta Z^{(\ell)}h^{(\ell-1)}\|_2^2 + \frac{1}{L^{2\alpha}}\|\Delta W^{(\ell)}\phi(h^{(\ell-1)})\|_2^2\right). \tag{16}$$

3. The updates and the current quantities do not perfectly cancel.

$$\begin{aligned} \|W_{t+1}^{(\ell)}\|_{\mathcal{S}_\infty}^2 &= \Theta\left(\|W_t^{(\ell)}\|_{\mathcal{S}_\infty}^2 + \|\Delta W^{(\ell)}\|_{\mathcal{S}_\infty}^2\right) \\ \text{and} \quad \|Z_{t+1}^{(\ell)}\|_{\mathcal{S}_\infty}^2 &= \Theta\left(\|Z_t^{(\ell)}\|_{\mathcal{S}_\infty}^2 + \|\Delta Z^{(\ell)}\|_{\mathcal{S}_\infty}^2\right) \end{aligned} \tag{17}$$

4. The current quantities and the lmos do not perfectly cancel.

$$\begin{aligned} \|\Delta W^{(\ell)}\phi(h^{(\ell-1)})\|_2^2 &= \Theta\left(\|\gamma W^{(\ell)}\phi(h^{(\ell-1)})\|_2^2 + \|\gamma\,\mathrm{lmo}(M_t^{W^{(\ell)}})\phi(h^{(\ell-1)})\|_2^2\right) \\ \text{and} \quad \|\Delta Z^{(\ell)}h^{(\ell-1)}\|_2^2 &= \Theta\left(\|\gamma_Z Z^{(\ell)}h^{(\ell-1)}\|_2^2 + \|\gamma_Z\,\mathrm{lmo}(M_t^{Z^{(\ell)}})h^{(\ell-1)}\|_2^2\right). \end{aligned} \tag{18}$$

These assumptions are empirically verified across depths and optimization steps, in Figures 27, 28, and 29 (the second row of Figure 30 also gives an analogous result to Equation (17)).

Update expression of $W^{(\ell)}$ Since we consider a residual network, we need to compute, for every layer ℓ

$$\Delta W^{(\ell)} = \begin{cases} \gamma\,\mathrm{lmo}(\nabla_{W^{(\ell)}}\mathcal{L}) & \text{with Unconstrained Scion} \\ \gamma\,\mathrm{lmo}(\nabla_{W^{(\ell)}}\mathcal{L}) - \gamma W^{(\ell)} & \text{with Scion.} \end{cases} \tag{19}$$

Further details about the updates and the LMOs expressions can be found in Table 1, in Equation (4) and in Equation (5).

The same update expressions apply for the matrices $Z^{(\ell)}, \ell \in \{1, \dots, L\}$.

To simplify the analysis, we consider the momentum $\beta^{(\ell)} = 0$ for each layer ℓ. As established in our analysis, the desiderata can be ensured by imposing suitable conditions on the spectral norm of the updates. Since the LMO has a fixed spectral norm regardless of whether momentum is used, we expect its behavior to remain unchanged. This expectation is further supported by our experiments, in which we considered nonzero momentum values.

3.4.3 Desideratum 1 is satisfied for SCION and UNCONSTRAINED SCION

Our next result considers semi-orthogonally initialized matrices with $\|W^{(\ell)}\|_{\mathcal{S}_\infty} = \Theta(\sqrt{\frac{d_\ell}{d_{\ell-1}}})$ and $\|Z^{(\ell)}\|_{\mathcal{S}_\infty} = \Theta(\sqrt{\frac{d_\ell}{d_{\ell-1}}}), \forall \ell \in \{1, \dots, L\}$, and shows that Desideratum 1 holds, extending the result in Dey et al. (2026) for Gaussian variables initialization.

Proposition 1 (SCION and UNCONSTRAINED SCION verify Desideratum 1)**.** *Under the assumptions defined in the subsection 3.4.2, the hidden layers and the output remain stable at the initialization when L and d_ℓ become increasingly large.*

We provide a sketch of the demonstration for SCION and UNCONSTRAINED SCION, where the same arguments hold. Complete derivations are available in Appendix C.3.

Proof sketch of Proposition 1. Let $\ell \in \{1, \dots, L\}$. By using the alignment of weight matrices in Equation (14), the scale of the activation function ϕ in Equation (13), and the weight initialization in Equation (12), we have

$$\begin{aligned}
\|h^{(\ell)}\|_2^2 &= \Theta(\|Z^{(\ell)} h^{(\ell-1)}\|_2^2 + \frac{1}{L^{2\alpha}} \|W^{(\ell)} \phi(h^{(\ell-1)})\|_2^2) \\
&= \Theta\left(\|Z^{(\ell)}\|_{\mathcal{S}_\infty}^2 \|h^{(\ell-1)}\|_2^2 + \frac{1}{L^{2\alpha}} \|W^{(\ell)}\|_{\mathcal{S}_\infty}^2 \|h^{(\ell-1)}\|_2^2 \right) \\
&= \Theta\left(\prod_{k=1}^{\ell} (\frac{d_k}{d_{k-1}} \times (1 + \frac{1}{L^{2\alpha}})) d_0 \right) \\
&= \Theta\left(d_\ell \prod_{k=1}^{\ell} (1 + \frac{1}{L^{2\alpha}}) \right).
\end{aligned}$$

Then, $\frac{1}{d_L}\|h^{(L)}\|_2^2 = \Theta\left((1 + \frac{1}{L^{2\alpha}})^L\right)$ converges when L goes to infinity if and only if $\alpha \geq \frac{1}{2}$.

Moreover,

$$\frac{1}{d_\ell}\|h^{(\ell)}\|_2^2 = \Theta(1) \quad \forall \ell \in \{1, \dots, L\} \text{ for } \alpha \geq \frac{1}{2}, \tag{20}$$

and, for $f = W^{(L+1)}\phi(h^{(L)})$, we have

$$\|f\|_2^2 = \Theta(\|W^{(L+1)}\|_{\mathcal{S}_\infty}^2 \|h^{(L)}\|_2^2) = \Theta(\frac{d_{\text{out}}}{d_L} \times d_L) = \mathcal{O}(1). \tag{21}$$

□

3.4.4 Desideratum 2 is satisfied for SCION and UNCONSTRAINED SCION

Following the formulation of Desideratum 2, we study the change in $h^{(\ell)}$ when we update $\theta^{(\ell)}$ and $Z^{(\ell)}$ only. In our setting, we analyze the change in $h^{(\ell)}$ induced by the updates of $W^{(\ell)}$ and $Z^{(\ell)}$.

Proposition 2 (SCION and UNCONSTRAINED SCION verify Desideratum 2)**.** *Under the assumptions defined in subsection 3.4.2, for* SCION *or* UNCONSTRAINED SCION*, for any training step t, the weights of each block contribute with order $1/L$ to feature movements, and each non-residual block contributes with constant order when L becomes increasingly large.*

We provide a sketch of the demonstrations for SCION. Complete derivations for SCION and UNCONSTRAINED SCION are available in Appendix C.4.2 and C.4.1 for the first training step. In Appendix C.5, we provide a proof that Propositions 1 and 2 hold for any training step t.

Proof sketch of Proposition 2 for SCION . Let $\ell \in \{1, \dots, L\}$. We have

$$\begin{aligned}\|\Delta_{W^{(\ell)},Z^{(\ell)}} h^{(\ell)}\|_2^2 &= \|\Delta Z^{(\ell)} h_t^{(\ell-1)} + L^{-\alpha} \Delta W^{(\ell)} \phi(h_t^{(\ell-1)})\|_2^2 \\ &= \Theta\Big(\|\gamma_Z Z^{(\ell)} h_t^{(\ell-1)}\|_2^2 + \|\gamma_Z \operatorname{lmo}(\nabla_{Z^{(\ell)}}\mathcal{L}) h_t^{(\ell-1)}\|_2^2 \\ &\quad + \|L^{-\alpha}\gamma W^{(\ell)} \phi(h_t^{(\ell-1)})\|_2^2 + \|L^{-\alpha}\gamma \operatorname{lmo}(\nabla_{W^{(\ell)}}\mathcal{L})\phi(h_t^{(\ell-1)})\|_2^2\Big).\end{aligned} \tag{22}$$

For the first term, using the alignment of the weights in Equation (14) and the weights initialization in Equation (12), we have

$$\begin{aligned}\|\gamma_Z Z^{(\ell)} h_t^{(\ell-1)}\|_2^2 &= \Theta\left(\gamma_Z^2 \|Z^{(\ell)}\|_{\mathcal{S}_\infty}^2 \|h_t^{(\ell-1)}\|_2^2\right) \\ &= \Theta\left(\gamma_Z^2 d_\ell\right) \quad \text{from Desideratum 1.}\end{aligned} \tag{23}$$

For the third term, using the alignment of the weights in Equation (14) and the scale of the activation function ϕ in Equation (13) as well as the weights initialization in Equation (12), we have

$$\begin{aligned}\|L^{-\alpha}\gamma W^{(\ell)} \phi(h_t^{(\ell-1)})\|_2^2 &= \Theta\left(L^{-2\alpha}\gamma^2 \|W^{(\ell)}\|_{\mathcal{S}_\infty}^2 \|h_t^{(\ell-1)}\|_2^2\right) \\ &= \Theta\left(L^{-2\alpha}\gamma^2 d_\ell\right) \quad \text{from Desideratum 1.}\end{aligned} \tag{24}$$

For the second and fourth terms, plugging spectral lmo expressions leads to

$$\begin{aligned}&\|\gamma_Z \operatorname{lmo}(\nabla_{Z^{(\ell)}}\mathcal{L}) h_t^{(\ell-1)}\|_2^2 + \|L^{-\alpha}\gamma \operatorname{lmo}(\nabla_{W^{(\ell)}}\mathcal{L})\phi(h_t^{(\ell-1)})\|_2^2 \\ =\ &\Theta\left(\frac{d_\ell}{d_{\ell-1}}\gamma_Z^2 \|h_t^{(\ell-1)}\|_2^2 + L^{-2\alpha}\frac{d_\ell}{d_{\ell-1}}\gamma^2 \|\phi(h_t^{(\ell-1)})\|_2^2\right).\end{aligned}$$

Using the scale of the activation function assumption in Equation (13), and Desideratum 1, we have

$$\begin{aligned}&\|\gamma_Z \operatorname{lmo}(\nabla_{Z^{(\ell)}}\mathcal{L}) h_t^{(\ell-1)}\|_2^2 + \|L^{-\alpha}\gamma \operatorname{lmo}(\nabla_{W^{(\ell)}}\mathcal{L})\phi(h_t^{(\ell-1)})\|_2^2 \\ =\ &\Theta\left(d_\ell(\gamma_Z^2 + L^{-2\alpha}\gamma^2)\right).\end{aligned}$$

Finally, we have

$$\|\Delta_{W^{(\ell)},Z^{(\ell)}} h^{(\ell)}\|_2^2 = \Theta\left(d_\ell(\gamma_Z^2 + L^{-2\alpha}\gamma^2)\right). \tag{25}$$

Therefore, to ensure that the entries of $\Delta h^{(\ell)}$ are $\Theta(1/L)$, we must set

$$\gamma = \gamma_{\text{base}} L^{\alpha-1}, \text{ and } \gamma_Z = \gamma_{Z\,\text{base}} L^{-1}. \tag{26}$$

□

Remark: If we do not learn the $Z^{(\ell)}$, then we have that $Z_{t+1}^{(\ell)} = Z_t^{(\ell)}$, and $\Delta Z^{(\ell)} = 0$, and we conclude by only requiring $\gamma = \gamma_{\text{base}} L^{\alpha-1}$.

In Figure 4, we empirically verify the feature learning condition by performing a coordinate check (Yang et al., 2023b). As we scale the depth L, we measure the magnitude changes at the final residual representation $h^{(L)}$ and at the output logits f. We observe that these magnitudes remain stable across scales, confirming successful feature learning.

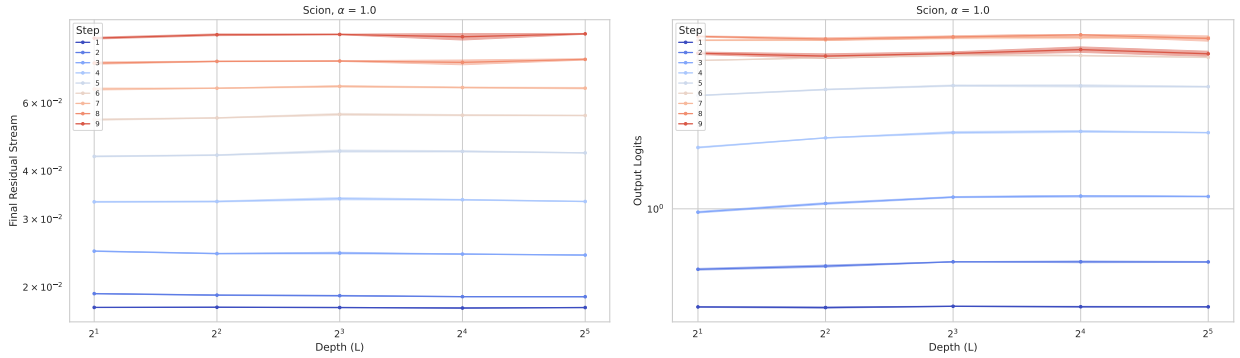


Figure 4: Coordinate checks for SCION, on nanoGPT trained on FineWeb, with $\alpha = 1.0$, and learning rate $\gamma_{\text{base}} = 2^{-11}$. We plot the change at the final residual representation $\|h_t^{(L)} - h_1^{(L)}\|_2$ (left plot) and at the output logits $\|f_t - f_1\|_2$ (right plot). More details on configuration can be found in Table 2 in Appendix B.

3.5 Complete Feature Learning

This criterion is not necessary for hyperparameter transfer, but it distinguishes $\alpha = 1$ from the other values in $[1/2, 1]$ as the only value for which the dynamics stay non-linear in its parameter, for every scale.

To present this criterion, we need two definitions described below.

Linearization The linearization $h^{\text{lin},\theta}$ of the function $h(\theta)$ with respect to θ about θ_0 is

$$h^{\text{lin},\theta}(\theta, \theta_0) = h(\theta_0) + \langle \nabla_\theta h(\theta)|_{\theta_0}, \theta - \theta_0 \rangle. \tag{27}$$

We say h is linear in θ if $h = h^{\text{lin},\theta}$.

Lazy-regime We say a layer $\phi(h^{(\ell)})$ is lazy with respect to a subset of parameters $\theta \subset \{\theta_j\}_{j<\ell}$ if at finite depth and width, $\phi(h^{(\ell)})$ is not linear in θ and the change $\Delta_\theta \phi(h^{(\ell)})$ at initialization from updating only θ (i.e. $\theta \mapsto \theta + \Delta\theta$) is asymptotically the same as the change to the linearization of h:

$$\frac{|\Delta_\theta h^{(\ell)} - \Delta_\theta h^{\text{lin},\theta}|}{|\Delta_\theta h^{\text{lin},\theta}|} = o(1) \quad \text{as } d_\ell, L \to \infty. \tag{28}$$

Empirically, better generalization is observed when the network parametrization satisfies complete feature learning, i.e. when neither the hidden layers $\{\phi(h^{(\ell)})\}_{\ell \in \{1,\dots,L\}}$, nor the output model f are lazy with respect to any subset of model parameters. We reproduce the experiment from Dey et al. (2026) for the SCION and UNCONSTRAINED SCION optimizers in Figure 5, which reports the best validation loss achieved across learning rates as a function of depth L, for $\alpha \in \{0, 1/2, 1\}$. Consistently with the complete feature learning criterion, $\alpha = 1$ is the only value that yields systematically lower loss as depth increases, for both SCION and UNCONSTRAINED SCION.

3.5.1 Non-lazy regime for SCION

Another way to measure whether or not a parametrization results in the lazy regime is to measure the relative distance from initialization compared to the linearization. This gives a way to empirically verify which values of α enable a training in a non-lazy regime.

We reproduce the experiment of Dey et al. (2026) for SCION and UNCONSTRAINED SCION in Figure 6, where we plot:

$$\frac{|\Delta_\theta h^{(\ell)} - \Delta_\theta h^{\text{lin},\theta}|}{|\Delta_\theta h^{\text{lin},\theta}|} \tag{29}$$

for multiple depths and $\alpha \in \{0, 1/2, 1\}$, and we verify empirically that SCION and UNCONSTRAINED SCION are not lazy for $\alpha = 1$ and $\alpha = 0$.

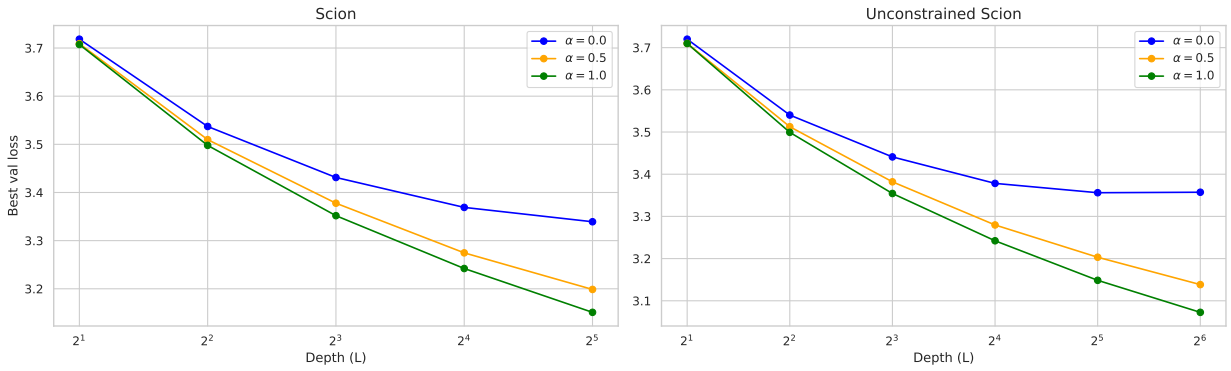


Figure 5: Best loss per learning rate in function of the depth L for $\alpha \in \{0, 1/2, 1\}$, with SCION and UNCONSTRAINED SCION, on nanoGPT, trained on FineWeb, on 1 seed. We observe that the choice $\alpha = 1$ provides the best performances overall. Note that the case $\alpha = 0$ is analogous to the SP/μP setup for Adam (Yang & Hu, 2021; Dey et al., 2026).

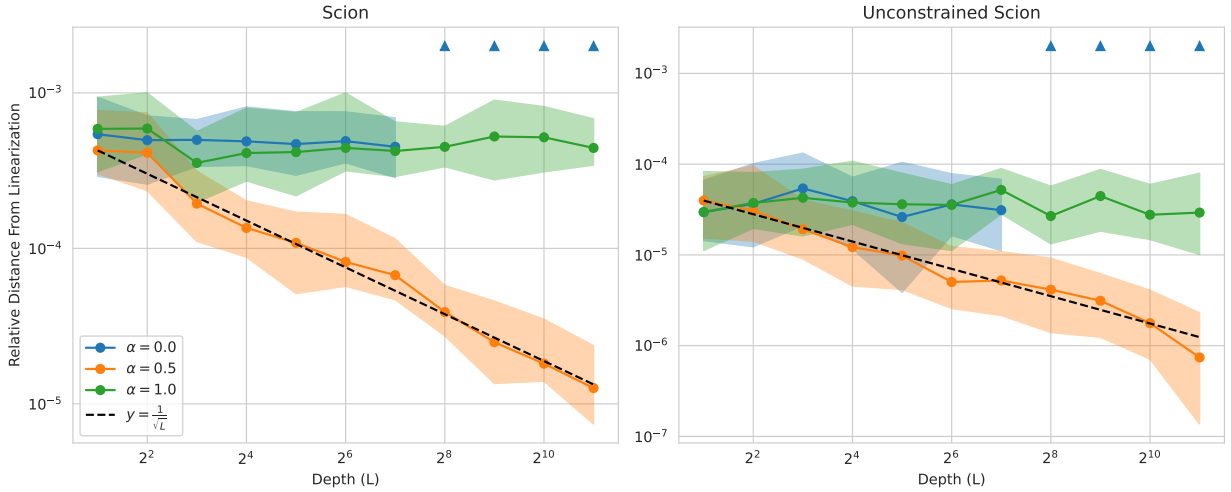


Figure 6: Relative distance from linearization for SCION and UNCONSTRAINED SCION on a 2-layer-per-block residual network, trained on MNIST, on 50 seeds. The y-axis represents Equation (29). The blue triangles represent the divergence of the case $\alpha = 0$ at large depth. Only $\alpha = 1$ results in complete and stable feature learning. $\alpha = 1/2$ approaches a linearized regime, at a rate of $\frac{1}{\sqrt{L}}$. Experimental details can be found in Table 6 in Appendix B.

3.6 Experiments

The architectures considered in the following experiments have no learnable $Z^{(\ell)}$ matrices, which are fixed to the identity. The hidden-layer width is constant, and training is restricted to the $W^{(\ell)}$ operators. We additionally conducted experiments with the learnable linear operators $Z^{(\ell)}$ on the residual stream in Figure 22 in Appendix G.1.

3.6.1 NanoGPT on FineWeb

We ran experiments on nanoGPT that we adapt from the code in Pethick et al. (2025b), which is based on modded-nanoGPT snapshot of Jordan et al. (2024a), itself based on the original nanoGPT of Karpathy (2023).

More experimental details can be found in Appendix B.

The architecture employs transformer blocks to implement the residual function $\mathcal{F}_\ell(h^{(\ell-1)}; \theta_{\mathcal{F}}^{(\ell)})$ for all hidden layers $\ell \in \{1, \ldots, L\}$. We perform orthogonalization for the query, key, value (Q, K, V), and MLP weight matrices separately, rather than applying the transformation to their concatenation.

Figures 7 and 8 show the depth-wise hyperparameter transfer for Scion and Unconstrained Scion, with the choice $\alpha = 1$ and $\alpha = 1/2$ respectively.

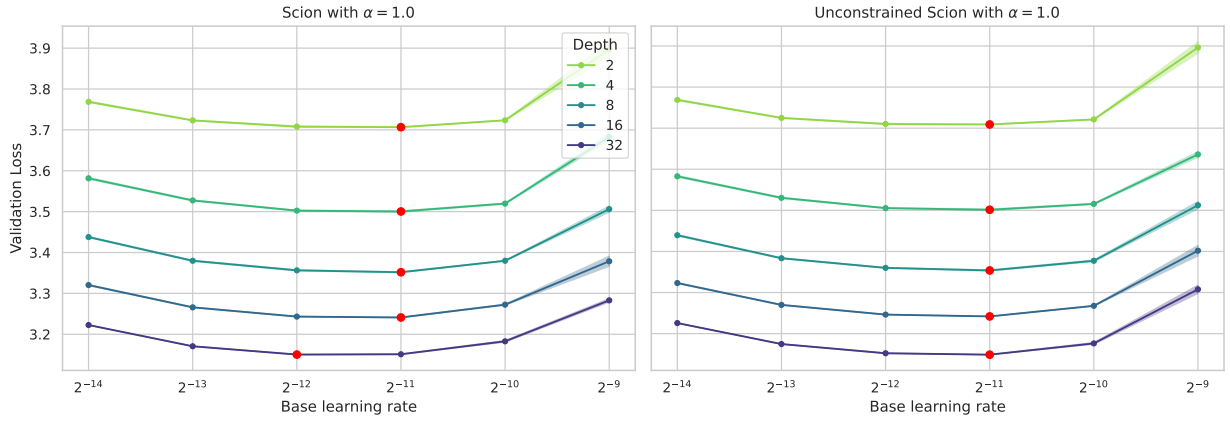


Figure 7: Scion and Unconstrained Scion on nanoGPT trained on FineWeb, with $\alpha = 1$, on 3 seeds. Depth-aligned and parallel loss curves indicate that the optimal base learning rate remains invariant with depth. When the minimizers of the curves do not exactly coincide, the loss values remain very close in this flat region. For the Scion case (left plot), the relative difference in loss value between base learning rate 2^{-12} and 2^{-11} for the deepest model is 0.024%.

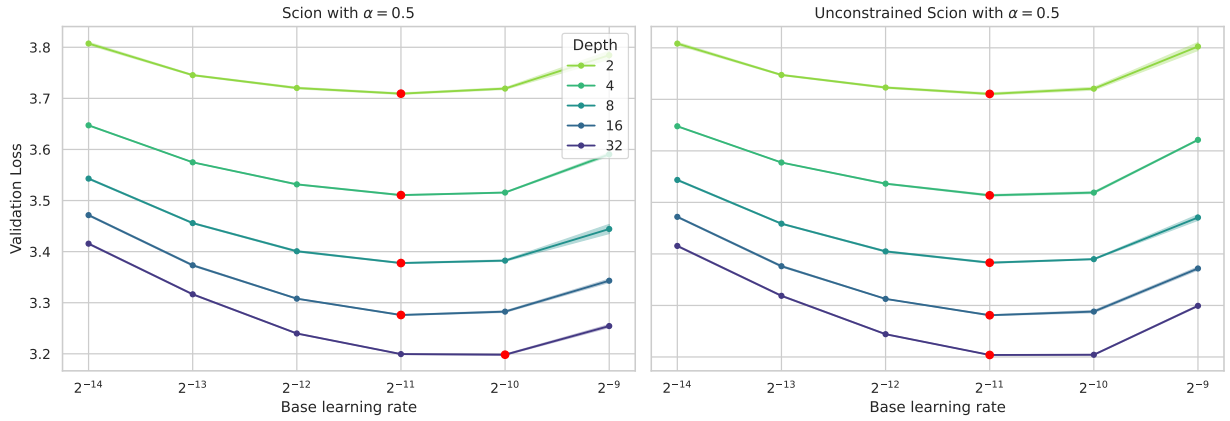


Figure 8: Scion and Unconstrained Scion on nanoGPT trained on FineWeb, with $\alpha = 0.5$, on 3 seeds. The value $\alpha = 0.5$ with the appropriate learning rate scaling also exhibits hyperparameter transfer with respect to the depth, as shown by the depth-aligned loss curves. For the Scion case (left plot), the minimizers of the curves do not exactly coincide in the flat region, and the relative difference in loss value between base learning rate 2^{-11} and 2^{-10} for the deepest model is 0.037%.

3.6.2 MLP-Mixer on CIFAR-10

We also used Scion on the MLP-Mixer architecture for image classification tasks (Tolstikhin et al., 2021), which offers the advantage of relying solely on MLP layers rather than convolutions, closely matching the modeling assumptions we made. Experimental details can be found in Appendix B.

Figures 9 and 10 show the depth-wise hyperparameter transfer for Scion and Unconstrained Scion, with the choice $\alpha = 1$ and $\alpha = 1/2$ respectively.

Again, we observe in Figures 9 and 10 that the minimizers of the curves are mostly aligned, and, when small deviations occur, the minimal values remain very close.

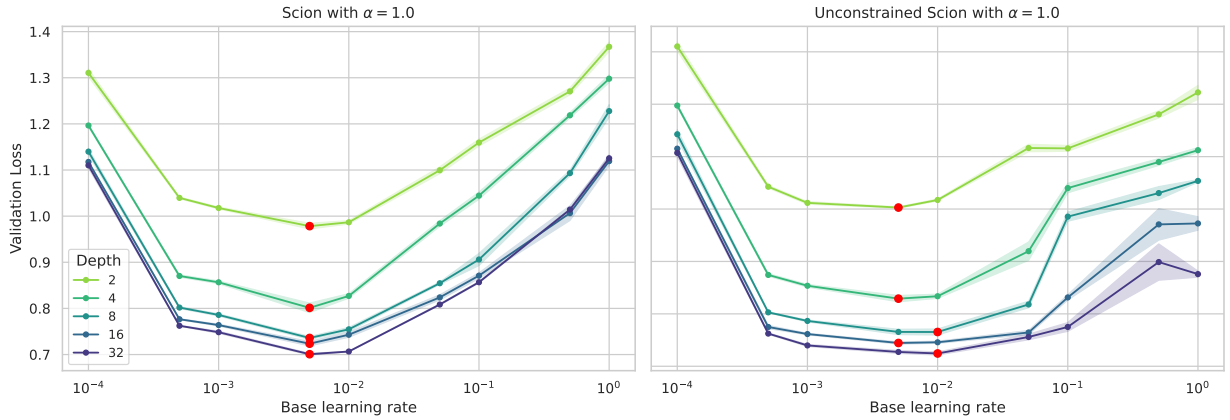


Figure 9: Scion and Unconstrained Scion on MLP-Mixer trained on CIFAR-10, with $\alpha = 1$, on 3 seeds. The curves exhibit different shapes and are not perfectly parallel, in contrast to the behavior observed in Figures 7 and 8. Nevertheless, the locations of the minimizers are largely aligned, and when deviations occur, the attained minimal values remain very close. For Unconstrained Scion (right plot), the relative difference in loss values for base learning rates 5×10^{-3} and 10^{-2} for the deepest model is approximately 0.62%.

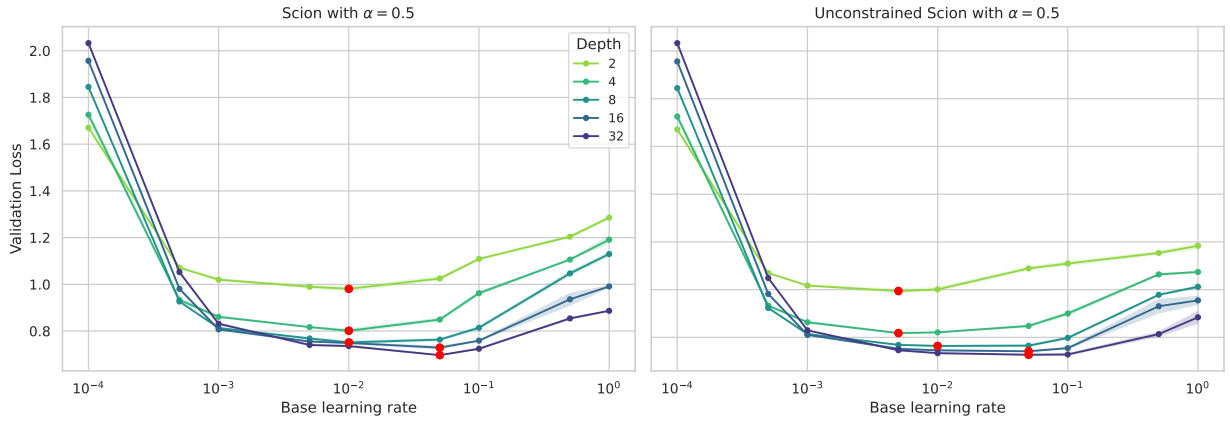


Figure 10: Scion and Unconstrained Scion on MLP-Mixer trained on CIFAR-10, with $\alpha = 0.5$, on 3 seeds. The curves display different behaviors from the nearly parallel trends observed in Figures 7 and 8. Despite these differences, the minimizers occur at similar locations, and the corresponding minimal values remain closely matched. For Scion (left plot), the relative difference in loss values for base learning rates 10^{-2} and 5×10^{-2} for the deepest model is approximately 6.3%. For Unconstrained Scion (right plot), the relative difference is approximately 2.7%.

3.6.3 DeiT on ImageNet

We trained a DeiT-base model adapted from Pethick et al. (2025b), which builds upon the original DeiT codebase of Touvron et al. (2021). For reference, the 12-layer baseline architecture by Touvron et al. (2021) achieves a top-1 test accuracy of 81.8% on ImageNet when trained using AdamW for 300 epochs. With our training setup, we similarly achieve an accuracy of 82.3% in 200 epochs, matching the reported results in Pethick et al. (2025b) (see Figure 11).

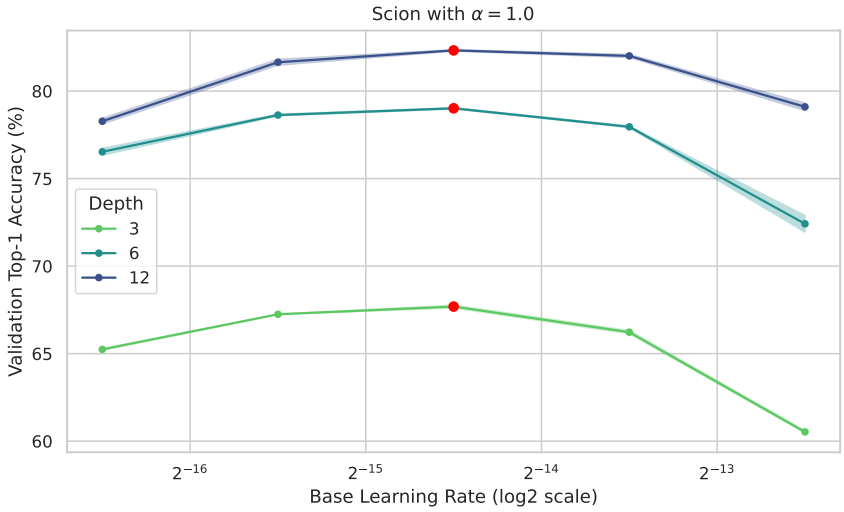


Figure 11: Scion on DeiT trained on ImageNet, with $\alpha = 1$, on 2 seeds. The similar trends and aligned optima of the top-1 accuracy curves across depths show that the optimal base learning rate is invariant with respect to depth. The best accuracy, achieved with depth $L = 12$, is 82.3%.

4 Width-wise Transfer with Spectral Constraints

4.1 Spectral conditions for feature learning

For this section, we will simplify the setup and focus our derivations on MLPs. In particular, we desire that the features and the updates have $\Theta(1)$ element size with respect to the width.

4.1.1 Problem setup

We consider an MLP with a fixed depth $L = \Theta(1)$, defined as

$$\begin{aligned} h^{(0)} &= W^{(0)}x \\ h^{(\ell)} &= W^{(\ell)}\phi(h^{(\ell-1)}) \quad (\forall \ell \in \{1, \dots, L\}) \\ f &= W^{(L+1)}\phi(h^{(L)}), \end{aligned} \tag{30}$$

where $x \in \mathbb{R}^{d_{\text{in}}}$ are the input data, $h^{(\ell)} \in \mathbb{R}^{d_\ell}, \ell \in \{0, \dots, L\}$ are the hidden states, and $f \in \mathbb{R}^{d_{\text{out}}}$ is the output after nonlinear activation ϕ. The embedding and un-embedding matrices are respectively $W^{(0)} \in \mathbb{R}^{d_0 \times d_{\text{in}}}$ and $W^{(L+1)} \in \mathbb{R}^{d_{\text{out}} \times d_L}$.

4.1.2 Spectral Scaling Condition

To ensure width-wise transfer, we adopt the conditions established by Yang et al. (2023a) for MLPs, which generalize to a broader range of architectures, including residual networks.

Desideratum 3 (Feature Learning)**.** *The hidden layers and their updates should be stable with the width:*

$$\|h^{(\ell)}\|_2^2 = \Theta(d_\ell) \text{ and } \|\Delta h^{(\ell)}\|_2^2 = \Theta(d_\ell) \quad \forall \ell = 1, \dots, L. \tag{31}$$

Feature learning can be ensured by the spectral scaling condition on the weight matrices and their updates:

$$\|W^{(\ell)}\|_{S_\infty}^2 = \Theta\left(\frac{d_\ell}{d_{\ell-1}}\right) \text{ and } \|\Delta W^{(\ell)}\|_{S_\infty}^2 = \Theta\left(\frac{d_\ell}{d_{\ell-1}}\right) \quad \forall \ell = 1, \dots, L. \tag{32}$$

Non-cancellation assumptions We make the following assumptions on the alignment between updates and the current parameters. For any layer ℓ, and training step t:

1. The current quantities and the lmo do not perfectly cancel

$$\|-\gamma W^{(\ell)} + \gamma \operatorname{lmo}(M_t^{(\ell)})\|_{\mathcal{S}_\infty}^2 = \Theta\left(\|\gamma W^{(\ell)}\|_{\mathcal{S}_\infty}^2 + \|\gamma \operatorname{lmo}(M_t^{(\ell)})\|_{\mathcal{S}_\infty}^2\right). \tag{33}$$

2. The different updates of the layer do not perfectly cancel.

$$\|\Delta h^{(\ell)}\|_2^2 = \Theta\left(\|\Delta W^{(\ell)}\phi(h^{(\ell-1)})\|_2^2 + \|W^{(\ell)}\Delta\phi(h^{(\ell-1)})\|_2^2 + \|\Delta W^{(\ell)}\Delta\phi(h^{(\ell-1)})\|_2^2\right). \tag{34}$$

These assumptions are empirically verified across widths and optimization steps in Figure 30.

4.2 Width Transfer for Scion

We provide an analysis of the width-transfer property of Scion, which was only demonstrated for Unconstrained Scion in Pethick et al. (2025b).

Proposition 3 (Scion and Unconstrained Scion verify Desideratum 3)**.** *Under the assumptions defined in the subsections 3.4.2 and 4.1.2, the updates of the features after a step of* Scion *or* Unconstrained Scion*, remain stable when the width d_ℓ becomes increasingly large.*

A demonstration of Proposition 3 is available in Appendix D.1, and an illustration of the width-wise transfer of the learning rate is given in Figure 12.

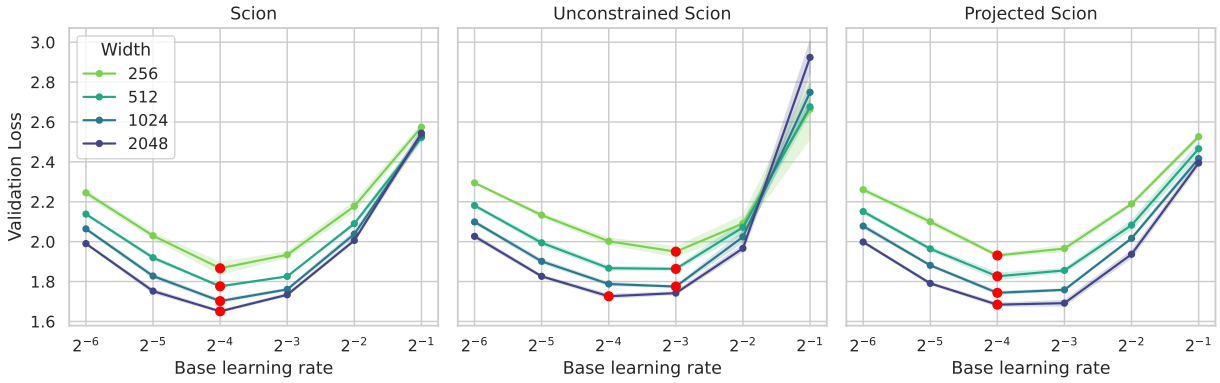


Figure 12: Width Transfer with Scion, Unconstrained Scion and Projected Scion on Shallow nanoGPT trained on Shakespeare-Char dataset, with depth 3, on 3 seeds. We observe that the minimizers of the curves, highlighted by the red dots, are generally well aligned. In the case where they differ slightly, the minimal values are nearly identical, indicating a flat region around the optimum. For Unconstrained Scion (middle plot), the relative difference in loss values for base learning rates 2^{-4} and 2^{-3} for the largest model is approximately 2.9%. Experimental details can be found in Table 4 in Appendix B.

4.3 Projected Scion

In this section, we consider an algorithm that enforces the constraints through projections, by directly clipping the singular values of the weight matrices to lie within a certain range. Doing so provides control of the singular values of the weights and their updates, which can help stabilize training (Newhouse et al., 2025). We provide the definition of spectral clipping below.

Definition 1 (Spectral Clipping)**.** *Let $W \in \mathbb{R}^{d\times n}$, and $W = U\Sigma V^\top$ be its singular value decomposition, where $\Sigma = diag(\sigma_1, \ldots, \sigma_{min(d,n)})$ is the diagonal matrix composed of the singular values of W, and U, V are orthogonal matrices. Let $a, b \in \mathbb{R}_+$ with $a < b$. The spectral clipping* $\text{spectral_clip}_{[a,b]} : \mathbb{R}^{d\times n} \to \mathbb{R}^{d\times n}$ *is defined as:*

$$\text{spectral_clip}_{[a,b]}(W) = U \,\text{clip}_{[a,b]}(\Sigma) V^\top \tag{35}$$

where $\text{clip}_{[a,b]}(\Sigma)$ *is the projection mapping of the singular values on* $[a, b]$*.*

Since computing the SVD is expensive in practice, especially for deep learning models with large weight matrices, we can reconstruct the clipping functions using the matrix sign function (Cesista, 2025) which can be approximated via the Newton-Schulz iterations (Kovarik, 1970; Björck & Bowie, 1971).

We can therefore study a variant of Scion, given in Algorithm 3, based on a projected version of SCG, where the update can be written as a composition of the spectral_clip function and the uSCG update.

Algorithm 3 Projected SCG

Input: Horizon n, initialization $\mathbf{\Theta}_1 \in \mathcal{D}$, $M_0 = 0$, momentum $\beta_t \in [0, 1)$, spectral constraints a and b with $a < b$, and stepsize $\gamma_t \in (0, 1)$

1: **for** $t = 1, \ldots, n$ **do**
2: Sample data $x \sim \mathcal{P}$
3: **for** $\theta^{(\ell)} \in \mathbf{\Theta}$ **do**
4: $M_t^{(\ell)} \leftarrow (1 - \beta_t)\nabla_{\theta_t^{(\ell)}} \mathcal{L} + \beta_t M_{t-1}^{(\ell)}$
5: $\theta_{t+1}^{(\ell)} \leftarrow \text{spectral_clip}_{[a,b]}(\theta_t^{(\ell)} + \gamma_t \,\text{lmo}(M_t^{(\ell)}))$
6: **end for**
7: **end for**

We also observe Algorithm 3 to exhibit width-wise hyperparameter-transfer in experiments, as detailed in the next subsection.

4.3.1 Width transfer for Projected Scion

Projected Scion makes it possible to establish an upper bound on the size of the feature updates that is independent of width. This provides a theoretical stability guarantee.

Proposition 4 (Width-wise stability of Projected Scion)**.** *Under the assumptions defined in Sections 3.4.2 and 4.1.2, the feature updates after a step of* Projected Scion *admit an upper bound that is independent of the width d_ℓ. In particular, for each layer ℓ,*

$$\|\Delta h^{(\ell)}\|_2^2 = \mathcal{O}(d_\ell) \tag{36}$$

with respect to the width d_ℓ.

Proposition 4 establishes the stability part of the width-wise scaling but it does not establish the matching lower bound to get $\|\Delta h^{(\ell)}\|_2^2 = \Theta(d_\ell)$. For the methods without projection considered in Section 4.2, the lower bound was obtainable by ruling out cancellations between the current parameters and the update. For Projected Scion, the projection introduces an additional nonlinearity that can result in systematic cancellation for small γ; details are provided in Appendix D.2 which includes an experiment that confirms

this cancellation happening. Establishing a matching lower bound for general spectral clipping therefore remains an open point in our analysis.

Figure 12 illustrates the empirically observed width-wise transfer property of Projected Scion.

5 Radius Transfer

Besides the learning rate, a remaining challenge lies in tuning the scales $\{\rho^{(\ell)}\}_{\ell\in\{0,\dots,L+1\}}$ of Scion and Unconstrained Scion. These radii appear explicitly in the lmo expressions scaling the layer-wise magnitude of the updates, and therefore play a crucial role in the optimization process.

In this section, we provide preliminary empirical evidence for radius transfer for Scion and Unconstrained Scion across both width and depth. We formalize the radius transfer pipeline into the reproducible Protocol below.

Protocol: Practical Learning Rate and Radius Transfer

1. **Apply Scaling Rules:** Apply the parameter and learning rate scaling rules defined in Section 3 and parametrize the radii. For instance, for an *(embedding → hidden → un-embedding)* architecture with tied embedding and un-embedding weights, parameterize the layer-wise radii configuration as $(a, 1, a)$, using a shared scalar factor $a > 0$.
2. **Low-Dimensional Sweep:** Define a small, computationally inexpensive version of the model (i.e. with small dimensions) and run a hyperparameter sweep to find the optimal learning rate and optimal a: (γ^*, a^*).
3. **Target Scale Deployment:** Train the large-scale target model directly using the optimal (γ^*, a^*), bypassing expensive tuning at scale.

We emphasize that this section is empirical and should be interpreted as an initial exploration of the phenomenon and of the practical protocol provided.

5.1 Radius and Depth Transfer

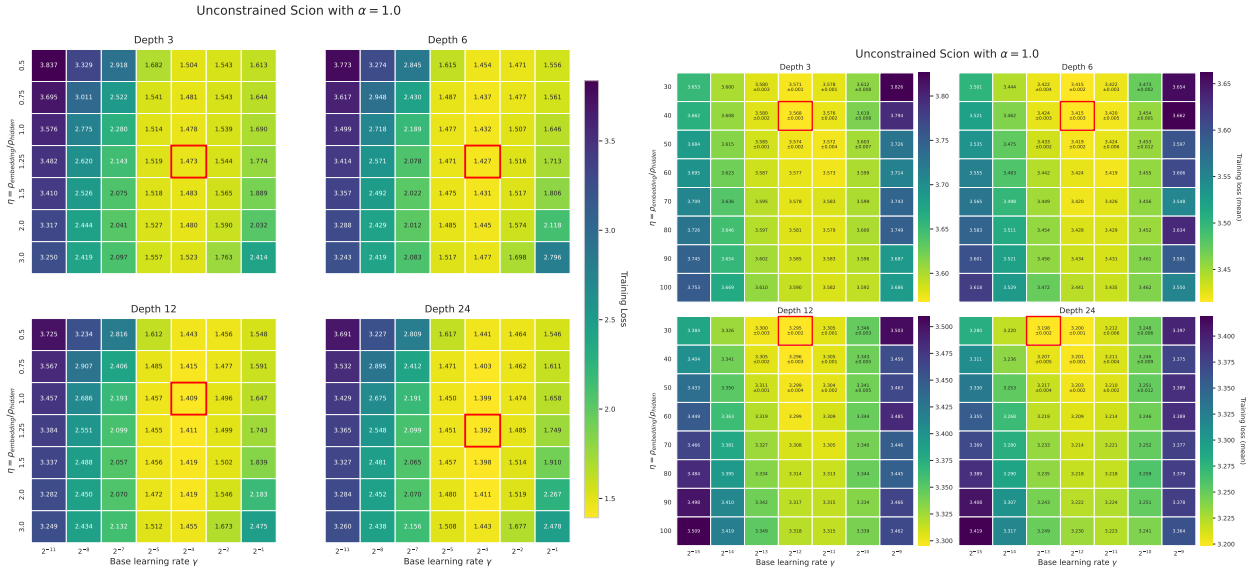
Large et al. (2024) define the modular norm recursively based on the model's architecture, which in particular allows normalization within this norm using a user-specified mass. Under this modular norm framework, the authors explore mass allocation and show that both the optimal mass ratio between hidden and extreme layers and the optimal learning rate transfer from small model to larger ones, both in depth and width, when training with Adam.

We conducted a similar experiment on Shallow nanoGPT on the Shakespeare-Char dataset, and on nanoGPT on FineWeb. Details of the experiments can be found in Table 4 and Table 2 respectively, in Appendix B. We trained multiple models of several depths, learning rates and ratios of radii $\eta = \frac{\rho_{\text{embedding}}}{\rho_{\text{hidden}}}$ where $\rho_{\text{embedding}}$ is the radius of the embedding and un-embedding layers and ρ_{hidden} is the radius of the hidden layers. The results are displayed in Figure 13a and Figure 13b.

Taken together, these experiments provide encouraging preliminary empirical evidence that the transfer of both the optimal learning rate and radii may occur. See also (Filatov et al., 2026, Section 3.4) for a similar experiment showing radius transfer across training horizons.

5.2 Radius and Width & Depth Transfer

In this section, we provide preliminary empirical evidence on the learning rate transfer of Scion across both the width and the depth of the model. This observation is empirical rather than theoretically established in our framework, since the width-and-depth-transfer analyses are derived under different architectural assumptions. Figure 14 illustrates this empirical behavior.



(a) Shakespeare-Char dataset.

(b) FineWeb dataset.

Figure 13: Preliminary empirical evidence for transfer of the ratio of the radii with Unconstrained Scion ($\alpha = 1$). The optimal combination of radii ratio and base learning rate is nearly identical across depths or lies within a flat region of the loss landscape, suggesting that this landscape remains invariant with respect to depth in the setting considered. *Left* (a): Trained on Shallow nanoGPT, for 1 seed. For depth 12, the relative difference in loss between the cell (η, base learning rate) $= (1.25, 2^{-4})$ and the cell $(1.0, 2^{-4})$ is 0.1%. Experimental details are in Table 4 in Appendix B. *Right* (b): Trained on nanoGPT. The cells with std values were trained on 3 seeds. For depth 24, the relative difference in loss between the cell (η, base learning rate) $= (40, 2^{-12})$ and the cell $(30, 2^{-13})$ is 0.06%. Experimental details are in Table 2 in Appendix B.

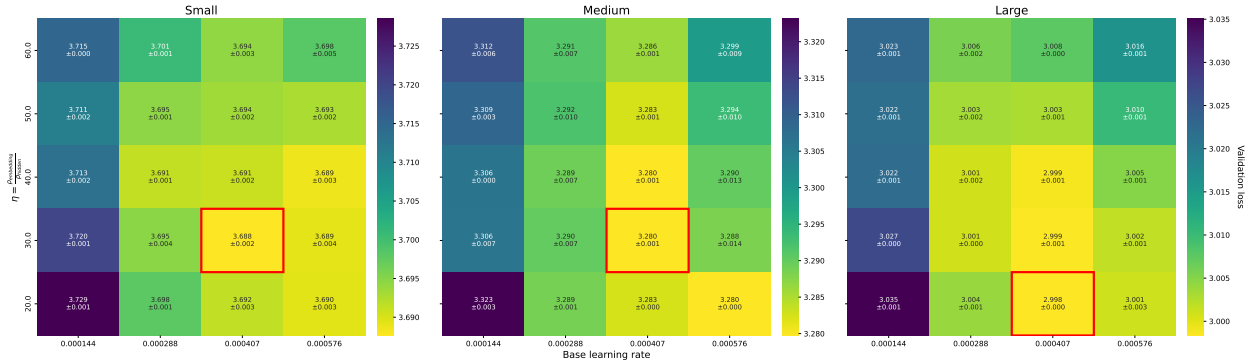


Figure 14: Preliminary empirical evidence for width and depth transfer with Scion, on nanoGPT, trained on FineWeb, with $\alpha = 1$, on 3 seeds. The Small model has depth 6 and width 384, the Medium one has depth 12 and width 768 and the Large one has depth 24 and width 1536. For the Large model, the relative difference in loss between the cell (η, base learning rate) $= (30, 0.000407)$ and the cell $(20, 0.000407)$ is 0.03%. Experimental details are in Table 2 in Appendix B.

The three models were trained for $5,100$ iterations. According to the Chinchilla scaling laws (Hoffmann et al., 2022), a compute-optimal training run requires approximately 20 tokens per parameter. Given our training configuration, where we consider a batch size of 512 and a sequence length of 1024, each training step processes $512 \times 1024 = 524,288$ tokens.

6 Conclusion

In this work, we investigated the hyperparameter-transfer behavior of Scion and its unconstrained variant, and we demonstrated that this optimizer supports both width and depth-wise transfer. Consistent with the findings of CompleteP (Dey et al., 2026), we observed that the setting $\alpha = 1$ yields the strongest performance and best transfer.

Our main contribution is to establish these transfer phenomena for the spectral optimizer Scion, in both its constrained and unconstrained variants, extending prior analyses of hyperparameter transfer.

Through a diverse set of experiments, we further showed that Scion can be parameterized to guarantee feature learning, operation in the non-lazy regime, and movement from initialization at the maximum stable learning rate.

Our experiments covered several deep neural network architectures and datasets, including nanoGPT trained on FineWeb, DeiT on ImageNet, and MLP-Mixer on CIFAR-10.

We finish by remarking that these results can also apply to Muon, provided that the components relying on Adam are scaled appropriately so that it remains compatible with the transfer regime.

6.1 Perspectives

Given the promising preliminary results observed in Section 5, it would be interesting to theoretically investigate the radius transfer property and derive a rigorous proof. Leveraging this hyperparameter property could prove highly beneficial for several downstream tasks. In particular, transferring the radius of a constrained set has direct implications for improving robustness against adversarial attacks (Goodfellow et al., 2015; Sokolić et al., 2017; Miyato et al., 2018), generalization bounds (Bartlett et al., 2017), or control on the Lipschitz continuity of neural networks (Large et al., 2024; Miyato et al., 2018). Extending to include other parametrizations of weight decay than the Frank-Wolfe step remains an interesting direction too (Chou, 2025).

Acknowledgments

This work uses computational resources from Framatome GPU clusters CRONOS and SELENA, two HPC systems used by Framatome and EDF Group for large-scale simulations and GPU-accelerated workloads. It additionally uses computational resources from the "Mésocentre" computing center of Université Paris-Saclay, CentraleSupélec and École Normale Supérieure Paris-Saclay supported by CNRS and Région Île-de-France (https://mesocentre.universite-paris-saclay.fr/). Some experiments were also performed using HPC resources from GENCI–IDRIS (Grant 2025-AD011016724).

References

Dario Amodei, Sundaram Ananthanarayanan, Rishita Anubhai, Jingliang Bai, Eric Battenberg, Carl Case, Jared Casper, Bryan Catanzaro, Qiang Cheng, Guoliang Chen, Jie Chen, Jingdong Chen, Zhijie Chen, Mike Chrzanowski, Adam Coates, Greg Diamos, Ke Ding, Niandong Du, Erich Elsen, Jesse Engel, Weiwei Fang, Linxi Fan, Christopher Fougner, Liang Gao, Caixia Gong, Awni Hannun, Tony Han, Lappi Vaino Johannes, Bing Jiang, Cai Ju, Billy Jun, Patrick LeGresley, Libby Lin, Junjie Liu, Yang Liu, Weigao Li, Xiangang Li, Dongpeng Ma, Sharan Narang, Andrew Ng, Sherjil Ozair, Yiping Peng, Ryan Prenger, Sheng Qian, Zongfeng Quan, Jonathan Raiman, Vinay Rao, Sanjeev Satheesh, David Seetapun, Shubho Sengupta, Kavya Srinet, Anuroop Sriram, Haiyuan Tang, Liliang Tang, Chong Wang, Jidong Wang, Kaifu Wang, Yi Wang, Zhijian Wang, Zhiqian Wang, Shuang Wu, Likai Wei, Bo Xiao, Wen Xie, Yan Xie, Dani Yogatama, Bin Yuan, Jun Zhan, and Zhenyao Zhu. Deep speech 2: end-to-end speech recognition in english and mandarin. In Proceedings of the 33rd International Conference on International Conference on Machine Learning - Volume 48, ICML'16, pp. 173–182. JMLR.org, 2016.

Peter L. Bartlett, Dylan J. Foster, and Matus J. Telgarsky. Spectrally-normalized margin bounds for neural networks. In I. Guyon, U. Von Luxburg, S. Bengio, H. Wallach, R. Fergus, S. Vishwanathan, and R. Garnett (eds.), Advances in Neural Information Processing Systems, volume 30. Curran Associates, Inc., 2017.

Jeremy Bernstein, Yu-Xiang Wang, Kamyar Azizzadenesheli, and Animashree Anandkumar. signSGD: Compressed optimisation for non-convex problems. In International Conference on Machine Learning, pp. 560–569. PMLR, 2018.

Åke Björck and Clazett Bowie. An iterative algorithm for computing the best estimate of an orthogonal matrix. SIAM Journal on Numerical Analysis, 8(2):358–364, 1971.

Blake Bordelon and Cengiz Pehlevan. Self-consistent dynamical field theory of kernel evolution in wide neural networks. Advances in Neural Information Processing Systems, 35:32240–32256, 2022.

Blake Bordelon, Hamza Chaudhry, and Cengiz Pehlevan. Infinite limits of multi-head transformer dynamics. Advances in Neural Information Processing Systems, 37:35824–35878, 2024a.

Blake Bordelon, Lorenzo Noci, Mufan Bill Li, Boris Hanin, and Cengiz Pehlevan. Depthwise hyperparameter transfer in residual networks: Dynamics and scaling limit. In The Twelfth International Conference on Learning Representations, 2024b.

David Carlson, Volkan Cevher, and Lawrence Carin. Stochastic spectral descent for restricted Boltzmann machines. In Artificial intelligence and statistics, pp. 111–119. PMLR, 2015a.

David Carlson, Ya-Ping Hsieh, Edo Collins, Lawrence Carin, and Volkan Cevher. Stochastic spectral descent for discrete graphical models. IEEE Journal of Selected Topics in Signal Processing, 10(2):296–311, 2015b.

David E Carlson, Edo Collins, Ya-Ping Hsieh, Lawrence Carin, and Volkan Cevher. Preconditioned spectral descent for deep learning. Advances in neural information processing systems, 28, 2015c.

Franz Louis Cesista. Fast, numerically stable, and auto-differentiable spectral clipping via Newton-Schulz iteration, 2025. URL `http://leloykun.github.io/ponder/spectral-clipping/`.

Lénaïc Chizat, Edouard Oyallon, and Francis Bach. On lazy training in differentiable programming. Advances in Neural Information Processing Systems, 32, 2019.

Jason Chuan-Chih Chou. Correction of decoupled weight decay. arXiv preprint arXiv:2512.08217, 2025.

DeepSeek-AI. DeepSeek-V4: Towards highly efficient million-token context intelligence, 2026.

Jacob Devlin, Ming-Wei Chang, Kenton Lee, and Kristina Toutanova. BERT: Pre-training of deep bidirectional transformers for language understanding. In Proceedings of the 2019 Conference of the North American Chapter of the Association for Computational Linguistics: Human Language Technologies, Volume 1 (Long and Short Papers), pp. 4171–4186, 2019.

Nolan Dey, Bin Claire Zhang, Lorenzo Noci, Mufan Li, Blake Bordelon, Shane Bergsma, Cengiz Pehlevan, Boris Hanin, and Joel Hestness. Don't be lazy: CompleteP enables compute-efficient deep transformers, 2026. URL https://arxiv.org/abs/2505.01618.

Andre Esteva, Brett Kuprel, Roberto A. Novoa, Justin Ko, Susan M. Swetter, Helen M. Blau, and Sebastian Thrun. Dermatologist-level classification of skin cancer with deep neural networks. Nature, 542(7639): 115–118, 2017.

Oleg Filatov, Jiangtao Wang, Jan Ebert, and Stefan Kesselheim. Optimal scaling needs optimal norm, 2026. URL https://arxiv.org/abs/2510.03871.

Marguerite Frank and Philip Wolfe. An algorithm for quadratic programming. Naval Research Logistics Quarterly, 3:95–110, 1956. URL https://api.semanticscholar.org/CorpusID:122654717.

Ian J. Goodfellow, Jonathon Shlens, and Christian Szegedy. Explaining and harnessing adversarial examples. In Yoshua Bengio and Yann LeCun (eds.), 3rd International Conference on Learning Representations (ICLR 2015), San Diego, CA, USA, May 7–9, 2015, Conference Track Proceedings, 2015.

Alex Graves, Abdel rahman Mohamed, and Geoffrey E. Hinton. Speech recognition with deep recurrent neural networks. 2013 IEEE International Conference on Acoustics, Speech and Signal Processing, pp. 6645–6649, 2013.

Vineet Gupta, Tomer Koren, and Yoram Singer. Shampoo: Preconditioned stochastic tensor optimization. In Jennifer Dy and Andreas Krause (eds.), 35th International Conference on Machine Learning, ICML 2018, 35th International Conference on Machine Learning, ICML 2018, pp. 2956–2964. International Machine Learning Society (IMLS), 2018. Publisher Copyright: © 2018 35th International Conference on Machine Learning, ICML 2018. All rights reserved.; 35th International Conference on Machine Learning, ICML 2018 ; Conference date: 10-07-2018 Through 15-07-2018.

Elad Hazan, Kfir Levy, and Shai Shalev-Shwartz. Beyond convexity: Stochastic quasi-convex optimization. Advances in Neural Information Processing Systems, 28, 2015.

Kaiming He, Xiangyu Zhang, Shaoqing Ren, and Jian Sun. Deep residual learning for image recognition. In Proceedings of the IEEE Conference on Computer Vision and Pattern Recognition (CVPR), pp. 770–778, 2016.

Geoffrey Hinton, Li Deng, Dong Yu, George Dahl, Abdel rahman Mohamed, Navdeep Jaitly, Andrew Senior, Vincent Vanhoucke, Phuongtrang Nguyen, Tara Sainath, and Brian Kingsbury. Deep neural networks for acoustic modeling in speech recognition: The shared views of four research groups. IEEE Signal Processing Magazine, 29:82–97, 2012.

Jordan Hoffmann, Sebastian Borgeaud, Arthur Mensch, Elena Buchatskaya, Trevor Cai, Eliza Rutherford, Diego de Las Casas, Lisa Anne Hendricks, Johannes Welbl, Aidan Clark, et al. Training compute-optimal large language models. arXiv preprint arXiv:2203.15556, 2022.

Guang Hu, Taotao Zhou, and Qianfeng Liu. Data-driven machine learning for fault detection and diagnosis in nuclear power plants: A review. Frontiers in Energy Research, 9:663296, 2021.

Rustem Islamov, Roman Machacek, Aurelien Lucchi, Antonio Silveti-Falls, Eduard Gorbunov, and Volkan Cevher. On the role of batch size in stochastic conditional gradient methods. arXiv preprint arXiv:2603.21191, 2026.

Keller Jordan, Jeremy Bernstein, Brendan Rappazzo, @fernbear.bsky.social, Boza Vlado, You Jiacheng, Franz Cesista, Braden Koszarsky, and @Grad62304977. Modded-NanoGPT: Speedrunning the NanoGPT baseline, 2024a. URL https://github.com/KellerJordan/modded-nanogpt.

Keller Jordan, Yuchen Jin, Vlado Boza, Jiacheng You, Franz Cesista, Laker Newhouse, and Jeremy Bernstein. Muon: An optimizer for hidden layers in neural networks, 2024b. URL https://kellerjordan.github.io/posts/muon/.

Kyle D. Julian and Mykel J. Kochenderfer. Guaranteeing safety for neural network-based aircraft collision avoidance systems. In 2019 IEEE/AIAA 38th Digital Avionics Systems Conference (DASC), pp. 1–10. IEEE, 2019.

Andrej Karpathy. nanoGPT. `https://github.com/karpathy/nanoGPT`, 2023. Accessed: 2025-01-25.

Kimi Team, Yifan Bai, Yiping Bao, Y. Charles, Cheng Chen, Guanduo Chen, Haiting Chen, Huarong Chen, Jiahao Chen, Ningxin Chen, et al. Kimi K2: Open agentic intelligence. arXiv preprint arXiv:2507.20534, 2025.

Kimi Team, Tongtong Bai, Yifan Bai, Yiping Bao, S. H. Cai, Yuan Cao, Y. Charles, H. S. Che, Cheng Chen, Guanduo Chen, et al. Kimi K2.5: Visual agentic intelligence. arXiv preprint arXiv:2602.02276, 2026a.

Kimi Team, Guangyu Chen, Yu Zhang, Jianlin Su, Weixin Xu, Siyuan Pan, Yaoyu Wang, Yucheng Wang, Guanduo Chen, Bohong Yin, et al. Attention residuals. arXiv preprint arXiv:2603.15031, 2026b.

Diederik P. Kingma and Jimmy Ba. Adam: A method for stochastic optimization. CoRR, abs/1412.6980, 2014.

Atli Kosson, Jeremy Welborn, Yang Liu, Martin Jaggi, and Xi Chen. Weight decay may matter more than muP for learning rate transfer in practice. arXiv preprint arXiv:2510.19093, 2025.

Zdislav Kovarik. Some iterative methods for improving orthonormality. SIAM Journal on Numerical Analysis, 7(3):386–389, 1970.

Alex Krizhevsky, Ilya Sutskever, and Geoffrey E. Hinton. ImageNet classification with deep convolutional neural networks. In F. Pereira, C. J. Burges, L. Bottou, and K. Q. Weinberger (eds.), Advances in Neural Information Processing Systems, volume 25. Curran Associates, Inc., 2012.

Tim Large, Yang Liu, Minyoung Huh, Hyojin Bahng, Phillip Isola, and Jeremy Bernstein. Scalable optimization in the modular norm. Advances in Neural Information Processing Systems, 37:73501–73548, 2024.

Takeru Miyato, Toshiki Kataoka, Masanori Koyama, and Yuichi Yoshida. Spectral normalization for generative adversarial networks. In 6th International Conference on Learning Representations (ICLR 2018), Vancouver, BC, Canada, April 30 – May 3, 2018, Conference Track Proceedings. OpenReview.net, 2018.

Laker Newhouse, R Preston Hess, Franz Cesista, Andrii Zahorodnii, Jeremy Bernstein, and Phillip Isola. Training transformers with enforced Lipschitz constants. arXiv preprint arXiv:2507.13338, 2025.

NVIDIA NeMo Team. Emerging optimizers. `https://github.com/NVIDIA-NeMo/Emerging-Optimizers`, 2025. NVIDIA NeMo, `https://docs.nvidia.com/nemo/emerging-optimizers/`.

Guilherme Penedo, Hynek Kydlíček, Loubna Ben Allal, Anton Lozhkov, Margaret Mitchell, Colin Raffel, Leandro Von Werra, and Thomas Wolf. The FineWeb datasets: Decanting the web for the finest text data at scale. In The Thirty-Eighth Conference on Neural Information Processing Systems Datasets and Benchmarks Track, 2024.

Thomas Pethick, Kimon Antonakopoulos, Antonio Silveti-Falls, Leena Chennuru Vankadara, and Volkan Cevher. Training neural networks at any scale. arXiv preprint arXiv:2511.11163, 2025a.

Thomas Pethick, Wanyun Xie, Kimon Antonakopoulos, Zhenyu Zhu, Antonio Silveti-Falls, and Volkan Cevher. Training deep learning models with norm-constrained LMOs. In Forty-Second International Conference on Machine Learning (ICML 2025), 2025b.

Shikai Qiu, Zixi Chen, Hoang Phan, Qi Lei, and Andrew Gordon Wilson. Hyperparameter transfer enables consistent gains of matrix-preconditioned optimizers across scales. arXiv preprint arXiv:2512.05620, 2025.

Liliang Ren, Yang Liu, Yelong Shen, and Weizhu Chen. Rethinking language model scaling under transferable hypersphere optimization. arXiv preprint arXiv:2603.28743, 2026.

Martin A. Riedmiller and Heinrich Braun. A direct adaptive method for faster backpropagation learning: the RPROP algorithm. IEEE International Conference on Neural Networks, pp. 586–591 vol.1, 1993.

Boris Shigida, Boris Hanin, and Andrey Gromov. Learning rate transfer in normalized transformers. arXiv preprint arXiv:2604.27077, 2026.

Karen Simonyan and Andrew Zisserman. Very deep convolutional networks for large-scale image recognition. CoRR, abs/1409.1556, 2014.

Varun Singh, Lucas Krauss, Sami Jaghouar, Matej Sirovatka, Charles Goddard, Fares Obied, Jack Min Ong, Jannik Straube, Aria Harley, Conner Stewart, et al. Arcee Trinity Large technical report. arXiv preprint arXiv:2602.17004, 2026.

Jure Sokolić, Raja Giryes, Guillermo Sapiro, and {Miguel R.D.} Rodrigues. Robust large margin deep neural networks. IEEE Transactions on Signal Processing, 65(16):4265–4280, August 2017. ISSN 1053-587X. doi: 10.1109/TSP.2017.2708039. Publisher Copyright: © 2017 IEEE.

Gang Sun and Shuyue Wang. A review of the artificial neural network surrogate modeling in aerodynamic design. Proceedings of the Institution of Mechanical Engineers, Part G: Journal of Aerospace Engineering, 233(16):5863–5872, 2019.

Ilya Sutskever, Oriol Vinyals, and Quoc V. Le. Sequence to sequence learning with neural networks. Advances in Neural Information Processing Systems, 27, 2014.

Christian Szegedy, Wei Liu, Yangqing Jia, Pierre Sermanet, Scott Reed, Dumitru Erhan, Vincent Vanhoucke, and Andrew Rabinovich. Going deeper with convolutions. In IEEE Conference on Computer Vision and Pattern Recognition (CVPR), pp. 1–9, 2015.

Chenwei Tang, Caiyang Yu, Yi Gao, Jianming Chen, Jiaming Yang, Jiuling Lang, Chuan Liu, Ling Zhong, Zhenan He, and Jiancheng Lv. Deep learning in nuclear industry: A survey. Big Data Mining and Analytics, 5(2):140–160, 2022.

Ilya O Tolstikhin, Neil Houlsby, Alexander Kolesnikov, Lucas Beyer, Xiaohua Zhai, Thomas Unterthiner, Jessica Yung, Andreas Steiner, Daniel Keysers, Jakob Uszkoreit, Mario Lucic, and Alexey Dosovitskiy. MLP-Mixer: An all-MLP architecture for vision. In M. Ranzato, A. Beygelzimer, Y. Dauphin, P.S. Liang, and J. Wortman Vaughan (eds.), Advances in Neural Information Processing Systems, volume 34, pp. 24261–24272. Curran Associates, Inc., 2021. URL https://proceedings.neurips.cc/paper_files/paper/2021/file/cba0a4ee5ccd02fda0fe3f9a3e7b89fe-Paper.pdf.

Eric J. Topol. High-performance medicine: The convergence of human and artificial intelligence. Nature Medicine, 25(1):44–56, 2019.

Hugo Touvron, Matthieu Cord, Matthijs Douze, Francisco Massa, Alexandre Sablayrolles, and Hervé Jégou. Training data-efficient image transformers & distillation through attention. In International Conference on Machine Learning, volume 139, pp. 10347–10357, July 2021.

Leena Chennuru Vankadara, Jin Xu, Moritz Haas, and Volkan Cevher. On feature learning in structured state space models. Advances in Neural Information Processing Systems, 37:86145–86179, 2024.

Ashish Vaswani, Noam Shazeer, Niki Parmar, Jakob Uszkoreit, Llion Jones, Aidan N. Gomez, Łukasz Kaiser, and Illia Polosukhin. Attention is all you need. Advances in Neural Information Processing Systems, 30, 2017.

Nikhil Vyas, Depen Morwani, Rosie Zhao, Itai Shapira, David Brandfonbrener, Lucas Janson, and Sham M. Kakade. SOAP: Improving and stabilizing Shampoo using Adam for language modeling. In International Conference on Learning Representations (ICLR), 2025.

Zhenda Xie, Yixuan Wei, Huanqi Cao, Chenggang Zhao, Chengqi Deng, Jiashi Li, Damai Dai, Huazuo Gao, Jiang Chang, Kuai Yu, et al. mHC: Manifold-constrained hyper-connections. arXiv preprint arXiv:2512.24880, 2025.

Ruihan Xu, Jiajin Li, and Yiping Lu. On the width scaling of neural optimizers under matrix operator norms I: Row/column normalization and hyperparameter transfer, 2026. URL https://arxiv.org/abs/2603.09952.

Greg Yang and Edward J. Hu. Tensor programs IV: Feature learning in infinite-width neural networks. In International Conference on Machine Learning, pp. 11727–11737. PMLR, 2021.

Greg Yang and Etai Littwin. Tensor programs IVb: Adaptive optimization in the infinite-width limit. In International Conference on Learning Representations (ICLR), 2023.

Greg Yang, Edward J. Hu, Igor Babuschkin, Szymon Sidor, Xiaodong Liu, David Farhi, Nick Ryder, Jakub Pachocki, Weizhu Chen, and Jianfeng Gao. Tensor programs V: Tuning large neural networks via zero-shot hyperparameter transfer. In Advances in Neural Information Processing Systems (NeurIPS), 2021.

Greg Yang, James B. Simon, and Jeremy Bernstein. A spectral condition for feature learning. arXiv preprint arXiv:2310.17813, 2023a.

Greg Yang, Dingli Yu, Chen Zhu, and Soufiane Hayou. Tensor programs VI: Feature learning in infinite-depth neural networks. In NeurIPS 2023 Workshop on Mathematics of Modern Machine Learning, 2023b.

Chenyu Zheng, Rongzhen Wang, Xinyu Zhang, and Chongxuan Li. Spectral condition for μP under width-depth scaling. arXiv preprint arXiv:2603.00541, 2026.

A Additional figures

A.1 Additional plots from the NanoGPT experiments

We trained multiple models where we vary the depth and the learning rate. Figure 15 illustrates the depth-wise hyperparameter transfer with $\alpha = 1.0$ and $\alpha = 0.5$, for Scion and Unconstrained Scion.

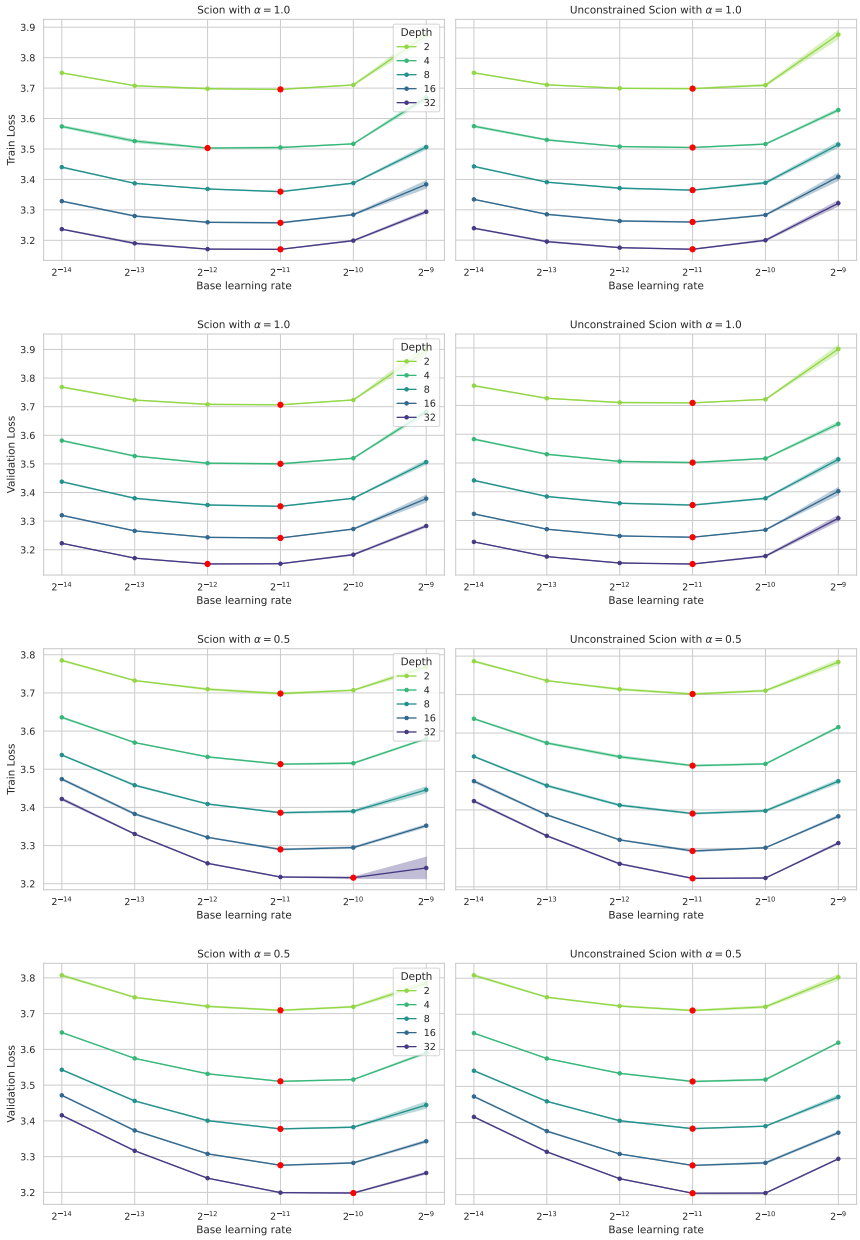


Figure 15: Scion (left column) and Unconstrained Scion (right column) on nanoGPT trained on FineWeb, on 3 seeds. The top rows correspond to $\alpha = 1.0$ and the bottom rows to $\alpha = 0.5$. The minimizers of the different curves, indicated by red dots, are strongly aligned across depths. When they do not exactly coincide, the corresponding loss values remain very close, indicating a flat loss region around the optimum. The validation loss relative errors are reported in Figures 7 and 8. The training loss relative error with Scion is approximately 0.050% with $\alpha = 1$ and depth $L = 4$, and 0.052% with $\alpha = 0.5$ and depth $L = 32$.

A.2 Additional plots from the MLP-Mixer experiments

Figure 16 illustrates the hyperparameter transfer in depth with $\alpha = 1.0$ and $\alpha = 0.5$ for Scion and Unconstrained Scion.

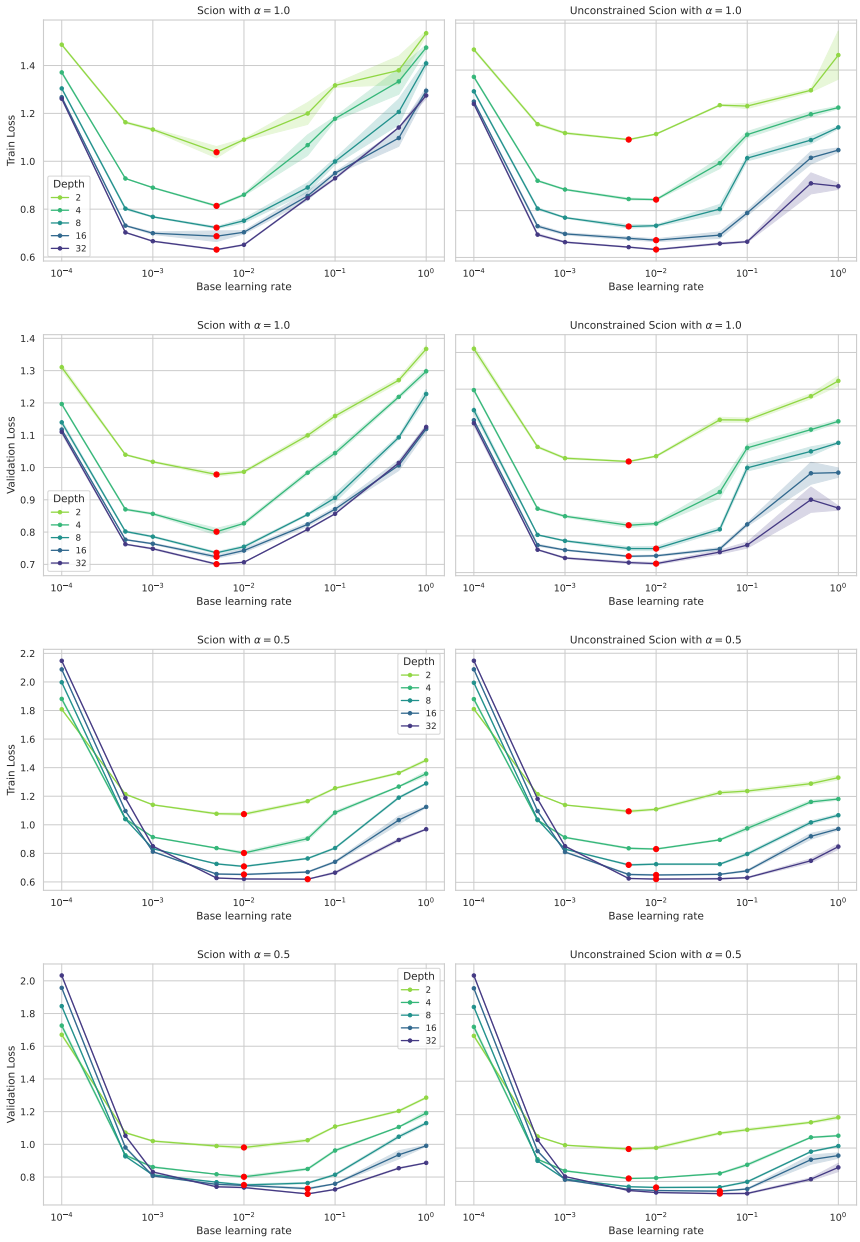


Figure 16: Scion (left columns) and Unconstrained Scion (right columns) on MLP-Mixer trained on CIFAR-10, on 3 seeds. The top rows correspond to $\alpha = 1.0$ and the bottom rows to $\alpha = 0.5$. Compared to the FineWeb experiments, the loss curves are less parallel across depths, indicating greater heterogeneity in optimization dynamics. Nevertheless, the minimizers of the curves, indicated by red dots, remain largely aligned. When deviations occur, they lie within a flat region of the loss landscape, where the achieved loss values remain very close. The validation loss relative errors are reported in Figures 9 and 10. The training loss relative error with Unconstrained Scion with $\alpha = 1$ for depth $L = 32$ is approximately 1.4%. With $\alpha = 0.5$, the relative errors for the deepest models are 1.5% and 0.67% with Scion and Unconstrained Scion respectively.

B Experimental details

NanoGPT We ran experiments on a snapshot of the speed-running model modded-nanoGPT of Jordan et al. (2024a), which is an evolution of the original nanoGPT of Karpathy (2023). Specifically, it replaces positional embeddings with rotary embeddings, uses RMSNorm in place of LayerNorm, uses a linear learning rate decay scheduler and employs a ScaledReLU^2 activation function. As this architecture ties the embedding and un-embedding weights, and following Recommendation 3.1 of Pethick et al. (2025b), we configured Scion and Unconstrained Scion using the Sign norm for the embedding and un-embedding layers and the Spectral norm for the hidden layers: `Sign` $\to$ `Spectral` $\to$ `Sign`. The models are trained on the FineWeb dataset (Penedo et al., 2024), for 5100 iterations with a batch size of 512 sequences of length 1024, totaling approximately 2.67×10^9 tokens. According to Chinchilla scaling laws (Hoffmann et al., 2022), this data budget is compute optimal for a model with roughly 133×10^6 parameters, which corresponds to a depth of 19 layers. Our evaluation across depths 2, 4, 8, 16, and 32 thus allows us to analyze model performance in both the under-parameterized regime and the over-parameterized regime, with depth 16 serving as our closest near-optimal baseline.

The details on the hyperparameters can be found in Table 2. The experiments were conducted on four H100 GPUs.

Shallow nanoGPT We also consider a nanoGPT model (Karpathy, 2023) where we additionally remove the weight sharing between the first and last layer. Following Pethick et al. (2025b), we configured Scion and Unconstrained Scion with a `Spectral` $\to$ `Spectral` $\to$ `Sign` norm configuration across the embedding, hidden and un-embedding layers. The hyperparameters can be found in Table 4. The experiments were performed using four H100 GPUs.

MLP-Mixer MLP-Mixer is an alternative architecture to transformers and is based entirely on MLPs. It is reported to achieve performance comparable to that of Convolutional Neural Networks and Transformers. Each Mixer layer consists of a token-mixing MLP, and a channel-mixing MLP, with skip-connections. Each of these MLP has two layers and a GELU activation function (Gaussian Error Linear Units function, defined as $GELU(x) = x\,\Phi(x)$ where Φ is the Cumulative Distribution Function for the Gaussian distribution). We replaced the Layer norm from Tolstikhin et al. (2021) with RMSNorm.

We used random cropping and data augmentation, by generating mixed samples on CIFAR-10. The training was performed on 300 epochs, with a batch size of 2048. We used a cosine learning rate scheduler with a linear warm-up. The embedding dimension is set to 128, the hidden widths of the token-mixing MLP and the channel-mixing MLP are 64 and 512 respectively.

Why not convolutions? We can note here that Scion does not provide spectral norm constraint guarantees to convolutional kernels, which also motivates the choice of this architecture. Indeed, the current Scion algorithm applies its constraints to the reshaped kernel tensor, rather than to the linear convolution operator, which corresponds to a large block-Toeplitz matrix. Since the spectral norm of the reshaped kernel is not the spectral norm of the induced convolution operator, the constraint enforced by the lmo is not applicable to the operator norm. Therefore, Scion cannot provide reliable spectral constraints for convolutional layers in practice.

Following Recommendation 3.1 of Pethick et al. (2025b) for computer vision tasks, we used the Spectral norm for the first and hidden layers and Sign for the last layer: `Spectral` $\to$ `Spectral` $\to$ `Sign`.

The details on the hyperparameters can be found in Table 5. The experiments were conducted on four V100 GPUs.

DeiT The DeiT-base model utilized in this work was adapted from the codebase of Pethick et al. (2025b), which originates from the official DeiT implementation developed by Touvron et al. (2021). Following Pethick et al. (2025b), we used the norm configuration `Spectral` $\to$ `Spectral` $\to$ `Sign`. Additionally, the architecture substituted LayerNorm with RMSNorm, scaled the GELU activation function by a factor of $\sqrt{2}$, and uses bias parameters, which slightly differs from the setup of our other experiments. See Table 3 for details on the hyperparameters. The experiments were conducted on 4×4 H100 GPUs.

Table 2: NanoGPT hyperparameters.

Hyperparameter	Unconstrained Scion and Scion
Width	768
Head dim	128
Activation function	ScaledReLU^2
Vocabulary size	50304
Dataset	FineWeb
Batch size	512
Block size	1024
Iterations n	5100
Warmdown	28.5%
Stepsize schedule	Constant then linear decay
Averaging parameter β	0.9
Radii	3000/50/3000

Table 3: DeiT hyperparameters.

Hyperparameter	Scion
Head dim	64
Activation function	$\sqrt{2}\cdot$ GELU
Normalization function	RMSNorm
Sequence length	197
Dataset	ImageNet-1k
Batch size	4096
Epochs	200
Stepsize schedule	Constant then cosine decay
Averaging parameter β	0.9
Radii	25/25/500

Table 4: Shallow nanoGPT hyperparameters.

Hyperparameter	Unconstrained Scion, Scion and Projected Scion
Depth (in the width-transfer experiments)	3
Width (in the depth-transfer experiments)	256
Head dim	64
Activation function	$\sqrt{2}\cdot$ GELU
Vocabulary size	65
Dataset	Shakespeare-Char
Batch size	32
Block size	1024
Iterations n	122
Stepsize schedule	Linear decay
Averaging parameter β	0.9
Radii (in the width-transfer experiments)	1/3/10

Table 5: MLP-Mixer hyperparameters.

Hyperparameter	Unconstrained Scion and Scion
Dataset	CIFAR-10
Embedding dimension	128
Token-mixing MLP hidden width	64
Channel-mixing MLP hidden width	512
Activation	GELU
Batch size	2048
Learning rate schedule	Cosine decay with linear warm-up
Training epochs n	300
Averaging parameter β	0.9
Radii	25/25/500

Table 6: Residual Network hyperparameters (for the relative distance from linearization analysis in Figure 6).

Hyperparameter	Unconstrained Scion and Scion
Dataset	MNIST
Layers per branch	2
Activation	ReLU
Batch size	128
Iterations n	1
Averaging parameter β	0.9

Table 7: Residual Network hyperparameters (for the weight alignment experiments in Figures 26, 27, 28, and 29).

Hyperparameter	Unconstrained Scion and Scion
Dataset	CIFAR-10
Layers per branch	1
Width	300
Activation	ReLU
Batch size	1024
Learning rates γ and γ_Z	10^{-2}
Averaging parameter β	0.9
Depth factor α	1
Radii	1/1/1

Table 8: MLP hyperparameters (for the weight alignment experiments in Figure 30).

Hyperparameter	Scion and Projected Scion
Dataset	CIFAR-10
Depth	3
Activation	ReLU
Batch size	1024
Learning rate γ	10^{-2}
Averaging parameter β	0.9
Radii	1/1/1
Interval $[a, b]$ for Projected Scion	[0, 1]

C Proofs of Complete Scion from Section 3.4

We recall Desiderata 1 and 2 and demonstrate in the following that they hold for Scion and Unconstrained Scion.

C.1 Depth transfer desiderata

Desideratum 1 (Stable Initialization)**.** *The hidden layers and the output remain stable (preventing signals from exploding or vanishing as they pass through many layers) at the initialization when L and d_ℓ become increasingly large:*

$$(\forall \ell \in \{1, \dots, L\}) \ \frac{1}{d_\ell}\|h^{(\ell)}\|_2^2 \in \Theta(1) \ \text{ and } \ \|f\|_2^2 \in \mathcal{O}(1), \quad \text{as } \ d_\ell \to \infty, L \to \infty. \tag{7}$$

Desideratum 2 (Stable Feature Update)**.** [4] *The weights of each residual block should contribute with order $1/L$ to feature movements, and each non-residual block should contribute with constant order (i.e. each non-residual block has a meaningful impact on the residual stream):*

$$\begin{aligned} &\frac{1}{\sqrt{d_\ell}}\|\Delta_{\theta_{\mathcal{F}}^{(\ell)}, Z^{(\ell)}} h^{(\ell)}\|_2 \in \Theta\left(\frac{1}{L}\right) \quad (\forall \ell \in \{1, \dots, L\}), \\ &\frac{1}{\sqrt{d_0}}\|\Delta W^{(0)} x\|_2 \in \Theta(1), \\ &\frac{1}{\sqrt{d_{\text{out}}}}\|\Delta W^{(L+1)} h^{(L)}\|_2 \in \Theta(1), \end{aligned} \tag{8}$$

where Δ designates the variation of the parameters between two successive iterations.

In the following, we will use the following argument: $\forall a, b > 0, (a+b)^2 = \Theta(a^2 + b^2)$. Indeed:

$$\begin{aligned} &(a+b)^2 = \mathcal{O}(a^2+b^2) \text{ since } (a+b)^2 = a^2 + 2ab + b^2 \leq 2(a^2+b^2). \\ \text{and} \quad &(a+b)^2 = \Omega(a^2+b^2) \text{ since } (a+b)^2 = a^2 + 2ab + b^2 \geq a^2 + b^2 \text{ with } a, b > 0, \\ \text{therefore}: \ &(a+b)^2 = \Theta(a^2+b^2), \forall a, b > 0. \end{aligned} \tag{37}$$

C.2 Assumptions and tools

Throughout this section, we maintain the same assumptions introduced in the main body of the paper in Section 3.4.2. For brevity, these foundational assumptions are not repeated here.

Update expression of $W^{(\ell)}$ Since we consider a residual network, we need to compute, for every layer ℓ

$$\Delta W^{(\ell)} = \gamma \, \text{lmo}(\nabla_{W^{(\ell)}} \mathcal{L}) \quad \text{with Unconstrained Scion} \tag{38}$$

$$\Delta W^{(\ell)} = -\gamma W^{(\ell)} + \gamma \, \text{lmo}(\nabla_{W^{(\ell)}} \mathcal{L}) \quad \text{with Scion} \tag{39}$$

We compute the expression for $\text{lmo}(\nabla_{\text{W}^{(\ell)}} \mathcal{L})$.

$$\nabla_{W^{(\ell)}} \mathcal{L} = \frac{\partial \mathcal{L}}{\partial W^{(\ell)}} = \frac{\partial \mathcal{L}}{\partial h^{(\ell)}} \frac{\partial h^{(\ell)}}{\partial W^{(\ell)}} = \frac{\partial \mathcal{L}}{\partial h^{(\ell)}} \frac{1}{L^\alpha} \phi(h^{(\ell-1)})^\top.$$

According to lemma C.5 of Pethick et al. (2025b), the lmo of the rank one gradient with batch size one can be written as:

$$\text{lmo}\left(\frac{\partial \mathcal{L}}{\partial h^{(\ell)}} \phi(h^{(\ell-1)})^\top\right) = -\rho^{(\ell)} \sqrt{\frac{d_\ell}{d_{\ell-1}}} \frac{\frac{\partial \mathcal{L}}{\partial h^{(\ell)}}}{\|\frac{\partial \mathcal{L}}{\partial h^{(\ell)}}\|_2} \frac{\phi(h^{(\ell-1)})^\top}{\|\phi(h^{(\ell-1)})\|_2}. \tag{40}$$

[4] The corresponding Desideratum in Dey et al. (2026) has $\frac{1}{d_\ell}\|\Delta_{\theta^{(\ell)}} h^{(\ell)}\|_2^2 = \Theta(\frac{1}{L})$, which slightly differs from ours, as we discuss in Appendix E.

Therefore, in the case of our residual model, and by using the scale-invariance property of the lmo, we have

$$\mathrm{lmo}(\nabla_{W^{(\ell)}}\mathcal{L}) = -\rho^{(\ell)}\sqrt{\frac{d_\ell}{d_{\ell-1}}}\frac{\frac{\partial\mathcal{L}}{\partial h^{(\ell)}}}{\|\frac{\partial\mathcal{L}}{\partial h^{(\ell)}}\|_2}\frac{\phi(h^{(\ell-1)})^\top}{\|\phi(h^{(\ell-1)})\|_2} \quad (\forall \ell \in \{1,\dots,L\}), \tag{41}$$

$$\mathrm{lmo}(\nabla_{W^{(0)}}\mathcal{L}) = -\rho^{(0)}\sqrt{\frac{d_0}{d_{\text{in}}}}\frac{\frac{\partial\mathcal{L}}{\partial h^{(0)}}}{\|\frac{\partial\mathcal{L}}{\partial h^{(0)}}\|_2}\frac{x^\top}{\|x\|_2}, \tag{42}$$

$$\mathrm{lmo}(\nabla_{W^{(L+1)}}\mathcal{L}) = -\rho^{(L+1)}\sqrt{\frac{d_{\text{out}}}{d_L}}\frac{\frac{\partial\mathcal{L}}{\partial f}}{\|\frac{\partial\mathcal{L}}{\partial f}\|_2}\frac{\phi(h^{(L)})^\top}{\|\phi(h^{(L)})\|_2}. \tag{43}$$

Update expression of $Z^{(\ell)}$ Similarly, let us suppose we learn the $\{Z^{(\ell)}\}_{\ell\in\{1,\dots,L\}}$ with the associated learning rate γ_Z and radii $\{\rho_{Z\ell}\}_{\ell\in\{1,\dots,L\}}$. Then, we have

$$\nabla_{Z^{(\ell)}}\mathcal{L} = \frac{\partial\mathcal{L}}{\partial h^{(\ell)}}\frac{\partial h^{(\ell)}}{\partial Z^{(\ell)}} = \frac{\partial\mathcal{L}}{\partial h^{(\ell)}}h^{(\ell-1)^\top}.$$

Therefore,

$$\Delta Z^{(\ell)} = \gamma_Z\,\mathrm{lmo}(\nabla_{Z^{(\ell)}}\mathcal{L}) = -\gamma_Z\rho_{Z\ell}\sqrt{\frac{d_\ell}{d_{\ell-1}}}\frac{\frac{\partial\mathcal{L}}{\partial h^{(\ell)}}}{\|\frac{\partial\mathcal{L}}{\partial h^{(\ell)}}\|_2}\frac{h^{(\ell-1)^\top}}{\|h^{(\ell-1)}\|_2} \quad (\forall \ell \in \{1,\dots,L\}). \tag{44}$$

C.3 Proof that Desideratum 1 holds for Scion and Unconstrained Scion

Proposition 1 (Scion and Unconstrained Scion verify Desideratum 1)**.** *Under the assumptions defined in the subsection 3.4.2, the hidden layers and the output remain stable at the initialization when L and d_ℓ become increasingly large.*

We provide here the complete demonstration that the Desideratum 1 is satisfied for Scion and Unconstrained Scion.

Proof. Let $\ell \in \{1,\dots,L\}$. Using the alignment of the weights (Equation (14)) and the scale of the activation function ϕ assumptions (Equation (13)), we have

$$\begin{aligned}
\|h^{(\ell)}\|_2^2 &= \Theta(\|Z^{(\ell)}h^{(\ell-1)}\|_2^2 + \frac{1}{L^{2\alpha}}\|W^{(\ell)}\phi(h^{(\ell-1)})\|_2^2) \qquad \text{from Equation (15)}\\
&= \Theta\left(\|Z^{(\ell)}\|_{\mathcal{S}_\infty}^2\|h^{(\ell-1)}\|_2^2 + \frac{1}{L^{2\alpha}}\|W^{(\ell)}\|_{\mathcal{S}_\infty}^2\|h^{(\ell-1)}\|_2^2\right) \qquad \text{from Equation (14) and Equation (13)}\\
&= \Theta\left((\|Z^{(\ell)}\|_{\mathcal{S}_\infty}^2 + \frac{1}{L^{2\alpha}}\|W^{(\ell)}\|_{\mathcal{S}_\infty}^2)\|h^{(\ell-1)}\|_2^2\right)\\
&= \Theta\left(\prod_{k=1}^{\ell}(\|Z^{(k)}\|_{\mathcal{S}_\infty}^2 + \frac{1}{L^{2\alpha}}\|W^{(k)}\|_{\mathcal{S}_\infty}^2)\|h^{(0)}\|_2^2\right).
\end{aligned}$$

Remark: In the above derivation, the assumptions we use are invoked once per layer and composed over L layers. *A priori*, constants hidden by $\Theta(\cdot)$ that are not uniform in ℓ or L could compound into a factor growing or collapsing with L. We emphasize that our assumptions are stated as holding with constants uniform in ℓ and L, empirically validated by Figure 27 across multiple depths.

Moreover, we can control these equivalence constants as follows, to prevent their accumulation. Let $r_\ell = \frac{\|h^{(\ell)}\|_2^2}{\|h^{(\ell-1)}\|_2^2} = 1 + 2L^{-\alpha}c_\ell + L^{-2\alpha}s_\ell$ with $c_\ell = \frac{\langle h^{(\ell-1)}, W^{(\ell)}\phi(h^{(\ell-1)})\rangle}{\|h^{(\ell-1)}\|_2^2}$ and $s_\ell = \frac{\|W^{(\ell)}\phi(h^{(\ell-1)})\|_2^2}{\|h^{(\ell-1)}\|_2^2}$. By Cauchy

Schwarz, we have that $|c_\ell| \leq \sqrt{(s_\ell)}$. By Lipschitz continuity of ϕ and using Equation (12), we have that $s_\ell \leq L_\phi^2 \|W^{(\ell)}\|_{\mathcal{S}_\infty}^2 \leq S$ with S being a constant uniform in ℓ and L. Then, we have

$$(1 - L^{-\alpha}\sqrt{S})^2 \leq \quad r_\ell \leq \quad (1 + L^{-\alpha}\sqrt{S})^2 \tag{45}$$

With $\alpha = 1$, we have

$$\begin{array}{ccccc} (1 - L^{-1}\sqrt{S})^{2L} & \leq & \prod_{\ell=1}^L r_\ell = \frac{\|h^{(L)}\|_2^2}{\|h^{(0)}\|_2^2} & \leq & (1 + L^{-1}\sqrt{S})^{2L} \\ e^{-2\sqrt{S}}(1 + o(1)) & \leq & \frac{\|h^{(L)}\|_2^2}{\|h^{(0)}\|_2^2} & \leq & e^{2\sqrt{S}}. \end{array} \tag{46}$$

Therefore, both directions hold with constants independent of L and ℓ. For $\alpha = \frac{1}{2}$, we have $e^{-2\sqrt{SL}} \leq \frac{\|h^{(L)}\|_2^2}{\|h^{(0)}\|_2^2} \leq e^{2\sqrt{SL}}$ which is not enough. Using Taylor expansion, we have $\log r_\ell = 2L^{-1/2}c_\ell + L^{-1}s_\ell - \frac{1}{2}\left(2L^{-1/2}c_\ell + L^{-1}s_\ell\right)^2 + \mathcal{O}(L^{-3/2}) = 2L^{-1/2}c_\ell + L^{-1}(s_\ell - 2c_\ell^2) + \mathcal{O}(L^{-3/2})$. Since s_ℓ and c_ℓ are bounded by constant, we have $\log r_\ell = 2L^{-1/2}c_\ell + \mathcal{O}(L^{-1})$. Then, $\log \frac{\|h^{(L)}\|_2^2}{\|h^{(0)}\|_2^2} = \sum_{\ell=1}^L \log r_\ell = 2L^{-1/2}\sum_{\ell=1}^L c_\ell + \mathcal{O}(1)$. Since $c_\ell = \frac{\langle h^{(\ell-1)}, W^{(\ell)}\phi(h^{(\ell-1)})\rangle}{\|h^{(\ell-1)}\|_2^2}$ form a martingale difference sequence in ℓ and $W^{(\ell)}$ is generated from a sign-symmetric distribution with variance σ^2/d_ℓ, we have that, conditionally on the previous state $h^{(\ell-1)}$, c_ℓ is a random variable with mean $\mathbb{E}[c_\ell|h^{(\ell-1)}] = 0$ and variance $\mathrm{Var}(c_\ell|h^{(\ell-1)}) \leq \frac{L_\phi^2\sigma^2}{d_\ell}$. Hence $\sum_{\ell=1}^L c_\ell = \mathcal{O}_{\mathbb{P}}(\sqrt{L/d})$ and $2L^{-1/2}\sum_{\ell=1}^L c_\ell = \mathcal{O}_{\mathbb{P}}(d^{-1/2})$ uniformly in L. And $\frac{\|h^{(L)}\|_2^2}{\|h^{(0)}\|_2^2} = e^{\mathcal{O}(1)}e^{\mathcal{O}_{\mathbb{P}}(d^{-1/2})} = e^{\mathcal{O}(1)}(1+o_{\mathbb{P}}(1))$. By orthogonality of martingale increments, with $d_{\min} = \min_\ell d_\ell$, we have $\mathbb{E}\Big[\Big(\sum_{\ell=1}^L c_\ell\Big)^2\Big] \leq L_\phi^2\sigma^2\sum_{\ell=1}^L \frac{1}{d_\ell} \leq \frac{L_\phi^2\sigma^2 L}{d_{\min}}$. Hence, $2L^{-1/2}\sum_{\ell=1}^L c_\ell = \mathcal{O}_{\mathbb{P}}(d_{\min}^{-1/2})$ uniformly in L. Together with the $\mathcal{O}(1)$ term, this gives $\frac{\|h^{(L)}\|_2^2}{\|h^{(0)}\|_2^2} = e^{\mathcal{O}(1)}\, e^{\mathcal{O}_{\mathbb{P}}(d_{\min}^{-1/2})}$, which is $e^{\mathcal{O}(1)}(1 + o_{\mathbb{P}}(1))$ as soon as $d_{\min} \to \infty$. Since $\|h^{(0)}\|_2^2 = \Theta(d_0)$, we obtain with high probability $\|h^{(L)}\|_2^2 = \Theta(d_0)$ uniformly in L (and $= \Theta(d)$ if all widths satisfy $d_\ell = \Theta(d)$).

From the alignment of the weights assumption (Equation (14)), combined with the initialization of the weights (Equation (12)), we have $\|h^{(0)}\|_2^2 = \Theta(\|W^{(0)}\|_{\mathcal{S}_\infty}^2\|x\|_2^2) = \Theta\left(\frac{d_0}{d_{\text{in}}}d_{\text{in}}\right) = \Theta(d_0)$. Then,

$$\begin{aligned} \|h^{(\ell)}\|_2^2 &= \Theta\left(\prod_{k=1}^{\ell}(\|Z^{(k)}\|_{\mathcal{S}_\infty}^2 + \frac{1}{L^{2\alpha}}\|W^{(k)}\|_{\mathcal{S}_\infty}^2)d_0\right) \\ &= \Theta\left(\prod_{k=1}^{\ell}(\frac{d_k}{d_{k-1}} + \frac{1}{L^{2\alpha}}\frac{d_k}{d_{k-1}})d_0\right) \\ &= \Theta\left(\prod_{k=1}^{\ell}(\frac{d_k}{d_{k-1}} \times (1 + \frac{1}{L^{2\alpha}}))d_0\right) \\ &= \Theta\left(\frac{d_\ell}{d_0}\prod_{k=1}^{\ell}(1 + \frac{1}{L^{2\alpha}})d_0\right) \\ &= \Theta\left(d_\ell\prod_{k=1}^{\ell}(1 + \frac{1}{L^{2\alpha}})\right). \end{aligned}$$

Then, $\frac{1}{d_L}\|h^{(L)}\|_2^2 = \Theta\left((1 + \frac{1}{L^{2\alpha}})^L\right)$ converges when L goes to infinity if and only if $\alpha \geq \frac{1}{2}$. Indeed, if we denote $y = \left(1 + \frac{1}{L^{2\alpha}}\right)^L$, then, by considering Taylor expansion, we have $\ln(y) = L\ln\left(1 + \frac{1}{L^{2\alpha}}\right) = L\left(\frac{1}{L^{2\alpha}} - \frac{1}{2L^{4\alpha}} + \mathcal{O}(\frac{1}{L^{6\alpha}})\right) = L^{1-2\alpha} - \frac{1}{2}L^{1-4\alpha} + \mathcal{O}(L^{1-6\alpha})$. Therefore,

$$\begin{cases} \ln(y) \to \infty \text{ and } y \to \infty & \text{if } \alpha < \frac{1}{2} \\ \ln(y) \to 1 \text{ and } y \to e & \text{if } \alpha = \frac{1}{2} \\ \ln(y) \to 0 \text{ and } y \to 1 & \text{if } \alpha > \frac{1}{2}. \end{cases}$$

Therefore,

$$\frac{1}{d_\ell}\|h^{(\ell)}\|_2^2 = \Theta(1) \quad \forall \ell \in \{1, \dots, L\} \text{ for } \alpha \geq \frac{1}{2}. \tag{47}$$

For $f = W^{(L+1)}\phi(h^{(L)})$, using the alignment of the weights and the scale of the activation function ϕ assumptions, we have

$$\|f\|_2^2 = \Theta(\|W^{(L+1)}\|_{\mathcal{S}_\infty}^2 \|h^{(L)}\|_2^2) \qquad \text{from Equation (14) and Equation (13).}$$

Then, using the initialization of the weights and the previous derivations of $\|h^{(L)}\|_2^2$, we have

$$\begin{aligned}\|f\|_2^2 &= \Theta\left(\frac{d_{\text{out}}}{d_L} \times d_L\right) \qquad \text{from Equation (12) and Equation (47)} \\ &= \Theta(1) \\ &= \mathcal{O}(1).\end{aligned}$$

These derivations are the same for Scion, since they only relate to the initialization of the model. □

C.4 Proof that Desideratum 2 holds for Scion and Unconstrained Scion

Proposition 2 (Scion and Unconstrained Scion verify Desideratum 2)**.** *Under the assumptions defined in subsection 3.4.2, for* Scion *or* Unconstrained Scion*, for any training step t, the weights of each block contribute with order $1/L$ to feature movements, and each non-residual block contributes with constant order when L becomes increasingly large.*

We provide here the complete demonstration that the Desideratum 2 is satisfied for Unconstrained Scion and Scion.

C.4.1 Unconstrained Scion case

Proof. Let $\ell \in \{1, \dots, L\}$. For Unconstrained Scion, we use the expressions of the updates $\Delta W^{(\ell)}$ and $\Delta Z^{(\ell)}$ as in Equation (38), that are written as

$$\Delta W^{(\ell)} = \gamma \,\text{lmo}(\nabla_{W^{(\ell)}}\mathcal{L}) \tag{48}$$

$$\Delta Z^{(\ell)} = \gamma_Z \,\text{lmo}(\nabla_{Z^{(\ell)}}\mathcal{L}). \tag{49}$$

Writing the expression of the layer $h^{(\ell)}$ in function of the previous $h^{(\ell-1)}$, we have

$$\begin{aligned}\Delta_{W^{(\ell)},Z^{(\ell)}} h^{(\ell)} &= h_{t+1}^{(\ell)} - h_t^{(\ell)} \\ &= Z_{t+1}^{(\ell)} h_{t+1}^{(\ell-1)} + L^{-\alpha} W_{t+1}^{(\ell)} \phi(h_{t+1}^{(\ell-1)}) - Z_t^{(\ell)} h_t^{(\ell-1)} - L^{-\alpha} W_t^{(\ell)} \phi(h_t^{(\ell-1)}).\end{aligned}$$

Since we are only looking at the change with the update of $W^{(\ell)}$ and $Z^{(\ell)}$, we have $h_{t+1}^{(\ell-1)} = h_t^{(\ell-1)}$. Therefore,

$$\begin{aligned}\Delta_{W^{(\ell)},Z^{(\ell)}} h^{(\ell)} &= Z_{t+1}^{(\ell)} h_t^{(\ell-1)} + L^{-\alpha} W_{t+1}^{(\ell)} \phi(h_t^{(\ell-1)}) - Z_t^{(\ell)} h_t^{(\ell-1)} - L^{-\alpha} W_t^{(\ell)} \phi(h_t^{(\ell-1)}) \\ &= \Delta Z^{(\ell)} h_t^{(\ell-1)} + L^{-\alpha} W_{t+1}^{(\ell)} \phi(h_t^{(\ell-1)}) - L^{-\alpha} W_t^{(\ell)} \phi(h_t^{(\ell-1)}) \\ &= \Delta Z^{(\ell)} h_t^{(\ell-1)} + L^{-\alpha} (W_t^{(\ell)} + \Delta W^{(\ell)}) \phi(h_t^{(\ell-1)}) - L^{-\alpha} W_t^{(\ell)} \phi(h_t^{(\ell-1)}) \\ &= \Delta Z^{(\ell)} h_t^{(\ell-1)} + L^{-\alpha} \Delta W^{(\ell)} \phi(h_t^{(\ell-1)}).\end{aligned}$$

By using the expressions of $\Delta W^{(\ell)}$ and $\Delta Z^{(\ell)}$ from Equation (48) and Equation (49) combined with the expressions of the associated LMOs in Equation (41) and Equation (44), we have

$$\|\Delta_{W^{(\ell)},Z^{(\ell)}} h^{(\ell)}\|_2^2 = \Theta\left(\|\Delta Z^{(\ell)} h_t^{(\ell-1)} + L^{-\alpha}\Delta W^{(\ell)}\phi(h_t^{(\ell-1)})\|_2^2\right)$$
$$= \Theta\left(\left\|\sqrt{\frac{d_\ell}{d_{\ell-1}}}\gamma_Z \frac{\frac{\partial \mathcal{L}}{\partial h^{(\ell)}}}{\|\frac{\partial \mathcal{L}}{\partial h^{(\ell)}}\|_2}\|(h_t^{(\ell-1)})\|_2 + L^{-\alpha}\sqrt{\frac{d_\ell}{d_{\ell-1}}}\gamma \frac{\frac{\partial \mathcal{L}}{\partial h^{(\ell)}}}{\|\frac{\partial \mathcal{L}}{\partial h^{(\ell)}}\|_2}\|\phi(h_t^{(\ell-1)})\|_2\right\|_2^2\right).$$

We note that $\Delta Z^{(\ell)} h^{(\ell-1)}$ and $L^{-\alpha}\Delta W^{(\ell)}\phi(h^{(\ell-1)})$ are both non-positive multiples of $\frac{\partial \mathcal{L}}{\partial h^{(\ell)}}$, which allows us to write

$$\|\Delta_{W^{(\ell)},Z^{(\ell)}} h^{(\ell)}\|_2^2 = \Theta\left(\left\|\sqrt{\frac{d_\ell}{d_{\ell-1}}}\gamma_Z \frac{\frac{\partial \mathcal{L}}{\partial h^{(\ell)}}}{\|\frac{\partial \mathcal{L}}{\partial h^{(\ell)}}\|_2}\|(h_t^{(\ell-1)})\|_2\right\|_2^2 + L^{-2\alpha}\left\|\sqrt{\frac{d_\ell}{d_{\ell-1}}}\gamma \frac{\frac{\partial \mathcal{L}}{\partial h^{(\ell)}}}{\|\frac{\partial \mathcal{L}}{\partial h^{(\ell)}}\|_2}\|\phi(h_t^{(\ell-1)})\|_2\right\|_2^2\right)$$
$$= \Theta\left(\frac{d_\ell}{d_{\ell-1}}\gamma_Z^2\|h_t^{(\ell-1)}\|_2^2 + L^{-2\alpha}\frac{d_\ell}{d_{\ell-1}}\gamma^2\|\phi(h_t^{(\ell-1)})\|_2^2\right).$$

Using the scale of the activation function assumption (Equation (13)), and the Desideratum 1 (Equation (47)), we have

$$\|\Delta_{W^{(\ell)},Z^{(\ell)}} h^{(\ell)}\|_2^2 = \Theta\left(\frac{d_\ell}{d_{\ell-1}}\gamma_Z^2\|h_t^{(\ell-1)}\|_2^2 + L^{-2\alpha}\frac{d_\ell}{d_{\ell-1}}\gamma^2\|h_t^{(\ell-1)}\|_2^2\right)$$
$$= \Theta\left(d_\ell\gamma_Z^2 + L^{-2\alpha}d_\ell\gamma^2\right)$$
$$= \Theta\left(d_\ell(\gamma_Z^2 + L^{-2\alpha}\gamma^2)\right).$$

So, $\frac{1}{d_\ell}\|\Delta_{W^{(\ell)},Z^{(\ell)}} h^{(\ell)}\|_2^2 = \Theta(\gamma_Z^2 + L^{-2\alpha}\gamma^2)$.

Therefore, if we want the entries of $\Delta h^{(\ell)}$ to be in $\Theta(1/L)$, we need to have

$$\gamma = \gamma_{\text{base}} L^{\alpha-1}, \text{ and } \gamma_Z = \gamma_{Z\,\text{base}} L^{-1}. \tag{50}$$

Now, let us consider the embedding layer $h^{(0)} = W^{(0)}x$.

Using the update expression $\Delta W^{(0)}$, from Equation (48), with the expression of the associated lmo in Equation (42), we have

$$\|\Delta W^{(0)}x\|_2^2 = \Theta\left(\gamma^2\frac{d_0}{d_{\text{in}}}\|x\|_2^2\right) = \Theta\left(\gamma^2 d_0\right) = \gamma^2\Theta(d_0).$$

Therefore, we do not need to scale the learning rate of the first weight $W^{(0)}$ in order to respect Desideratum 2, and

$$\gamma_{W^{(0)}} = \gamma_{W^{(0)}\,\text{base}}. \tag{51}$$

Finally, for the output layer $f = W^{(L+1)}\phi(h^{(L)})$, using the update expression $\Delta W^{(L+1)}$ from Equation (48) with the associated lmo expressions in Equation (43), and Desideratum 1 (Equation (47)) applied to $h^{(L)}$, we have

$$\|\Delta W^{(L+1)}h^{(L)}\|_2^2 = \Theta\left(\gamma^2\frac{d_{\text{out}}}{d_L}\frac{\|\frac{\partial \mathcal{L}}{\partial f}\|_2^2}{\|\frac{\partial \mathcal{L}}{\partial f}\|_2^2}\frac{\|\phi(h^{(L)})\|_2^2}{\|\phi(h^{(L)})\|_2^2}\|h^{(L)}\|_2^2\right)$$
$$= \Theta\left(\gamma^2\frac{d_{\text{out}}}{d_L}\|h^{(L)}\|_2^2\right)$$
$$= \gamma^2\Theta\left(d_{\text{out}}\right).$$

Therefore, we do not need to scale the learning rate of the last weight $W^{(L+1)}$ in order to respect Desideratum 2.

$$\gamma_{W^{(L+1)}} = \gamma_{W^{(L+1)}\text{base}}. \tag{52}$$

□

C.4.2 SCION case

Proof. Let $\ell \in \{1, \dots, L\}$. For SCION, we use the expressions of the updates $\Delta W^{(\ell)}$ and $\Delta Z^{(\ell)}$ as in Equation (39), that are written as

$$\Delta W^{(\ell)} = -\gamma W^{(\ell)} + \gamma \operatorname{lmo}(\nabla_{W^{(\ell)}} \mathcal{L}) \tag{53}$$

$$\Delta Z^{(\ell)} = -\gamma_Z Z^{(\ell)} + \gamma_Z \operatorname{lmo}(\nabla_{Z^{(\ell)}} \mathcal{L}). \tag{54}$$

Then,

$$\begin{aligned}
\|\Delta_{W^{(\ell)},Z^{(\ell)}} h^{(\ell)}\|_2^2 &= \|\Delta Z^{(\ell)} h_t^{(\ell-1)} + L^{-\alpha} \Delta W^{(\ell)} \phi(h_t^{(\ell-1)})\|_2^2 \\
&= \Theta\left(\|\Delta Z^{(\ell)} h_t^{(\ell-1)}\|_2^2 + \|L^{-\alpha} \Delta W^{(\ell)} \phi(h_t^{(\ell-1)})\|_2^2\right) \qquad \text{from Equation (16)} \\
&= \Theta\Big(\|(-\gamma_Z Z^{(\ell)} + \gamma_Z \operatorname{lmo}(\nabla_{Z^{(\ell)}} \mathcal{L})) h_t^{(\ell-1)}\|_2^2 \\
&\quad + \|L^{-\alpha}(-\gamma W^{(\ell)} + \gamma \operatorname{lmo}(\nabla_{W^{(\ell)}} \mathcal{L}))\phi(h_t^{(\ell-1)})\|_2^2\Big) \\
&= \Theta\Big(\|\gamma_Z Z^{(\ell)} h_t^{(\ell-1)}\|_2^2 + \|\gamma_Z \operatorname{lmo}(\nabla_{Z^{(\ell)}} \mathcal{L}) h_t^{(\ell-1)}\|_2^2 \\
&\quad + \|L^{-\alpha} \gamma W^{(\ell)} \phi(h_t^{(\ell-1)})\|_2^2 + \|L^{-\alpha} \gamma \operatorname{lmo}(\nabla_{W^{(\ell)}} \mathcal{L}) \phi(h_t^{(\ell-1)})\|_2^2\Big). \quad \text{from Equation (18)}
\end{aligned}$$

We saw in the unconstrained case that the second and fourth terms are in $\Theta(d_\ell(\gamma_Z^2 + L^{-2\alpha}\gamma^2))$.

For the third term, using the alignment of the weights (Equation (14)) and the scale of the activation function ϕ (Equation (13)) assumptions, we have

$$\begin{aligned}
\|L^{-\alpha} \gamma W^{(\ell)} \phi(h_t^{(\ell-1)})\|_2^2 &= \Theta\left(L^{-2\alpha}\gamma^2 \|W^{(\ell)}\|_{\mathcal{S}_\infty}^2 \|\phi(h_t^{(\ell-1)})\|_2^2\right) \\
&= \Theta\left(L^{-2\alpha}\gamma^2 \|W^{(\ell)}\|_{\mathcal{S}_\infty}^2 \|h_t^{(\ell-1)}\|_2^2\right).
\end{aligned}$$

Then, using the initialization of the weights in Equation (12) and the Desideratum 1 in Equation (47), we have

$$\begin{aligned}
\|L^{-\alpha} \gamma W^{(\ell)} \phi(h_t^{(\ell-1)})\|_2^2 &= \Theta\left(L^{-2\alpha}\gamma^2 \frac{d_\ell}{d_{\ell-1}} d_{\ell-1}\right) \\
&= \Theta\left(L^{-2\alpha}\gamma^2 d_\ell\right).
\end{aligned}$$

Similarly, for the first term, we have

$$\begin{aligned}
\|\gamma_Z Z^{(\ell)} h_t^{(\ell-1)}\|_2^2 &= \Theta\left(\gamma_Z^2 \|Z^{(\ell)}\|_{\mathcal{S}_\infty}^2 \|h_t^{(\ell-1)}\|_2^2\right) \\
&= \Theta\left(\gamma_Z^2 \frac{d_\ell}{d_{\ell-1}} d_{\ell-1}\right) \\
&= \Theta\left(\gamma_Z^2 d_\ell\right).
\end{aligned}$$

Finally, we have

$$\|\Delta_{W^{(\ell)},Z^{(\ell)}} h^{(\ell)}\|_2^2 = \Theta\left(d_\ell(\gamma_Z^2 + L^{-2\alpha}\gamma^2)\right).$$

We can conclude in the same way as in the unconstrained case.

Now, let us consider the embedding layer $h^{(0)} = W^{(0)}x$. With Scion, using the update expression of $W^{(0)}$ in Equation (53), combined with the associated lmo expression in Equation (42), we have

$$\begin{aligned}\Delta W^{(0)} &= -\gamma W^{(0)} + \gamma \text{lmo}(\nabla_{W^{(0)}}\mathcal{L}) \\ &= -\gamma W^{(0)} - \gamma\rho^{(0)}\sqrt{\frac{d_0}{d_{\text{in}}}}\frac{\frac{\partial \mathcal{L}}{\partial h^{(0)}}}{\|\frac{\partial \mathcal{L}}{\partial h^{(0)}}\|_2}\frac{x^\top}{\|x\|_2}.\end{aligned}$$

Then, using the alignment of the weights (Equation (14)) and the initialization of $W^{(0)}$ (Equation (12)) assumptions, we have

$$\begin{aligned}\|\Delta W^{(0)}x\|_2^2 &= \Theta\left(\gamma^2\|W^{(0)}x\|_2^2 + \gamma^2\frac{d_0}{d_{\text{in}}}\|x\|_2^2\right) \quad \text{from Equation (18)} \\ &= \Theta\left(\gamma^2\|W^{(0)}\|_{\mathcal{S}_\infty}^2\|x\|_2^2 + \gamma^2\frac{d_0}{d_{\text{in}}}\|x\|_2^2\right) \quad \text{(Claim 1 in Yang et al. (2023a))} \\ &= \Theta\left(\gamma^2\frac{d_0}{d_{\text{in}}}d_{\text{in}} + \gamma^2\frac{d_0}{d_{\text{in}}}d_{\text{in}}\right) \\ &= \Theta\left(2\gamma^2 d_0\right) \\ &= \gamma^2\Theta\left(d_0\right).\end{aligned}$$

We can conclude similarly to the unconstrained case.

Finally, for the output layer $f = W^{(L+1)}\phi(h^{(L)})$, if we use the update expression of $W^{(L+1)}$ in Equation (53), combined with the associated lmo expression in Equation (43),we have

$$\Delta W^{(L+1)} = -\gamma W^{(L+1)} - \gamma\rho^{(L+1)}\sqrt{\frac{d_{\text{out}}}{d_L}}\frac{\frac{\partial \mathcal{L}}{\partial f}}{\|\frac{\partial \mathcal{L}}{\partial f}\|_2}\frac{\phi(h^{(L)})^\top}{\|\phi(h^{(L)})\|_2}.$$

Then, using the alignment of the weights (Equation (14)), the initialization of $W^{(L+1)}$ (Equation (12)) and the Desideratum 1 (Equation (47)) applied to $h^{(L)}$, we have

$$\begin{aligned}\|\Delta W^{(L+1)}h^{(L)}\|_2^2 &= \Theta\left(\gamma^2\|W^{(L+1)}h^{(L)}\|_2^2 + \gamma^2\|\text{lmo}(\nabla_{W^{(L+1)}}\mathcal{L})h^{(L)}\|_2^2\right) \quad \text{(from Equation (18))} \\ &= \Theta\left(\gamma^2\|W^{(L+1)}\|_{\mathcal{S}_\infty}^2\|h^{(L)}\|_2^2 + \gamma^2 d_{\text{out}}\right) \\ &= \Theta\left(\gamma^2\frac{d_{\text{out}}}{d_L}d_L + \gamma^2 d_{\text{out}}\right) \\ &= \Theta\left(\gamma^2 d_{\text{out}}\right).\end{aligned}$$

And we can conclude the same way as in the unconstrained case.

□

C.5 Proof that Desiderata 1 and 2 hold for any step t

The proof of Desideratum 2 relies on the results in Desideratum 1, which is stated only for initialization. In other words, in Appendix C.4.1 and C.4.2, we only proved Desideratum 2 for the step $t = 1$.

In this section, we demonstrate that Desideratum 1 holds for any step t by induction, which implied that Desideratum 2 holds for any step t as well.

Proof. Let us show by induction that, for all steps t we have $\|h_t^{(\ell)}\|_2^2 = \Theta(d_\ell)$, $\|W_t^{(\ell)}\|_{\mathcal{S}_\infty}^2 = \Theta(\frac{d_\ell}{d_{\ell-1}})$, and $\|Z_t^{(\ell)}\|_{\mathcal{S}_\infty}^2 = \Theta(\frac{d_\ell}{d_{\ell-1}})$. The initialization step is already verified by Desideratum 1. Now, let us assume that $\|h_t^{(\ell)}\|_2^2 = \Theta(d_\ell)$ holds at step t. Then,

$$\begin{aligned}
\|h_{t+1}^{(\ell)}\|_2^2 &= \|Z_{t+1}^{(\ell)} h_{t+1}^{(\ell-1)} + \frac{1}{L^\alpha} W_{t+1}^{(\ell)} \phi(h_{t+1}^{(\ell-1)})\|_2^2 \\
&= \Theta\left(\|Z_{t+1}^{(\ell)} h_{t+1}^{(\ell-1)}\|_2^2 + \frac{1}{L^{2\alpha}} \|W_{t+1}^{(\ell)} \phi(h_{t+1}^{(\ell-1)})\|_2^2\right) \qquad \text{from Equation (15)} \\
&= \Theta\left(\|Z_{t+1}^{(\ell)}\|_{\mathcal{S}_\infty}^2 \|h_{t+1}^{(\ell-1)}\|_2^2 + \frac{1}{L^{2\alpha}} \|W_{t+1}^{(\ell)}\|_{\mathcal{S}_\infty}^2 \|h_{t+1}^{(\ell-1)}\|_2^2\right) \qquad \text{from Equation (14) and Equation (13)} \\
&= \Theta\left(\left(\|Z_{t+1}^{(\ell)}\|_{\mathcal{S}_\infty}^2 + \frac{1}{L^{2\alpha}} \|W_{t+1}^{(\ell)}\|_{\mathcal{S}_\infty}^2\right) \|h_{t+1}^{(\ell-1)}\|_2^2\right) \\
&= \Theta\left(\prod_{k=1}^{\ell} \left(\|Z_{t+1}^{(k)}\|_{\mathcal{S}_\infty}^2 + \frac{1}{L^{2\alpha}} \|W_{t+1}^{(k)}\|_{\mathcal{S}_\infty}^2\right) \|h_{t+1}^{(0)}\|_2^2\right).
\end{aligned} \tag{55}$$

And, under the assumption that the updates do not perfectly cancel current quantities (Equation (17)), we have, for all layers ℓ,

$$\begin{aligned}
\|Z_{t+1}^{(\ell)}\|_{\mathcal{S}_\infty}^2 &= \|Z_t^{(\ell)} + \Delta Z^{(\ell)}\|_{\mathcal{S}_\infty}^2 \\
&= \Theta\left(\|Z_t^{(\ell)}\|_{\mathcal{S}_\infty}^2 + \|\Delta Z^{(\ell)}\|_{\mathcal{S}_\infty}^2\right) \\
&= \Theta\left(\frac{d_\ell}{d_{\ell-1}} + \frac{d_\ell}{d_{\ell-1}}\right) \qquad \text{by induction, and using Equation (12).} \\
&= \Theta\left(\frac{d_\ell}{d_{\ell-1}}\right).
\end{aligned} \tag{56}$$

Similarly, we have, for all layers ℓ,

$$\|W_{t+1}^{(\ell)}\|_{\mathcal{S}_\infty}^2 = \Theta\left(\frac{d_\ell}{d_{\ell-1}}\right). \tag{57}$$

Besides,

$$\|h_{t+1}^{(0)}\|_2^2 = \|W_{t+1}^{(0)} x\|_2^2 = \Theta\left(\|W_{t+1}^{(0)}\|_{\mathcal{S}_\infty}^2 \|x\|_2^2\right) = \Theta\left(\frac{d_0}{d_{\text{in}}} d_{\text{in}}\right) = \Theta(d_0). \tag{58}$$

Therefore,

$$\begin{aligned}
\|h_{t+1}^{(\ell)}\|_2^2 &= \Theta\left(\prod_{k=1}^{\ell} \left(\|Z_{t+1}^{(k)}\|_{\mathcal{S}_\infty}^2 + \frac{1}{L^{2\alpha}} \|W_{t+1}^{(k)}\|_{\mathcal{S}_\infty}^2\right) \|h_{t+1}^{(0)}\|_2^2\right) \\
&= \Theta\left(\prod_{k=1}^{\ell} \left(\frac{d_k}{d_{k-1}} + \frac{1}{L^{2\alpha}} \frac{d_k}{d_{k-1}}\right) d_0\right) \\
&= \Theta\left(d_\ell \underbrace{\left(1 + \frac{1}{L^{2\alpha}}\right)^\ell}_{\Theta(1) \text{ with } \alpha \geq \frac{1}{2}}\right) \\
&= \Theta(d_\ell),
\end{aligned} \tag{59}$$

which ends the proof.
We note that this also naturally leads to $\|f\|_2^2 = \mathcal{O}(1)$, following the same steps as in Appendix C.3. □

D Proofs of the Width Transfer from Section 4

We recall Desideratum 3 and demonstrate that it holds for Scion, extending the prior width-transfer results derived by Pethick et al. (2025b) for Unconstrained Scion.

Desideratum 3 (Feature Learning)**.** *The hidden layers and their updates should be stable with the width:*

$$\|h^{(\ell)}\|_2^2 = \Theta(d_\ell) \text{ and } \|\Delta h^{(\ell)}\|_2^2 = \Theta(d_\ell) \quad \forall \ell = 1, \dots, L. \tag{31}$$

D.1 Proof of the width transfer with Scion, from Section 4.2

Proposition 3 (Scion and Unconstrained Scion verify Desideratum 3)**.** *Under the assumptions defined in the subsections 3.4.2 and 4.1.2, the updates of the features after a step of* Scion *or* Unconstrained Scion*, remain stable when the width d_ℓ becomes increasingly large.*

Proof. Let $\ell \in \{1, \dots, L\}$. With Scion, the update of the weight matrix $W^{(\ell)}$ can be written as:

$$\Delta W^{(\ell)} = -\gamma W^{(\ell)} + \gamma \, \mathrm{lmo}(\nabla_{W_t^{(\ell)}} \mathcal{L}).$$

By using Equation (34) and Equation (33) combined with the expression of the lmo in Equation (41), we have

$$\begin{aligned} \|\Delta h^{(\ell)}\|_2^2 = \Theta \Big(& \gamma^2 \|W^{(\ell)} \phi(h^{(\ell-1)})\|_2^2 + \gamma^2 \frac{d_\ell}{d_{\ell-1}} \|\phi(h^{(\ell-1)})\|_2^2 \\ & + \|W^{(\ell)} \Delta\phi(h^{(\ell-1)})\|_2^2 + \|\Delta W^{(\ell)} \Delta\phi(h^{(\ell-1)})\|_2^2 \Big). \end{aligned} \tag{60}$$

By using the alignment of the weights (Equation (14)), the initialization of the weights $W^{(\ell)}$ (Equation (12)), and the scale of the activation function ϕ assumption in Equation (13), we have

$$\|h^{(\ell)}\|_2 = \Theta(\|W^{(\ell)}\|_{\mathcal{S}_\infty} \|h^{(\ell-1)}\|_2) = \Theta(\sqrt{d_\ell}).$$

With the scale of the activation function ϕ assumption in Equation (13), we also have:

$$\|\phi(h^{(\ell)})\|_2^2 = \Theta(d_\ell). \tag{61}$$

Therefore, by using the weight alignment assumption in Equation (14) and the weight initialization as in Equation (12), we have

$$\begin{aligned} \|W^{(\ell)} \phi(h^{(\ell-1)})\|_2^2 &= \Theta(\|W^{(\ell)}\|_{S_\infty}^2 \|\phi(h^{(\ell-1)})\|_2^2) \\ &= \Theta\left(\frac{d_\ell}{d_{\ell-1}} \|h^{(\ell-1)}\|_2^2 \right) \\ &= \Theta\left(\frac{d_\ell}{d_{\ell-1}} d_{\ell-1} \right) \\ &= \Theta\left(d_\ell \right). \end{aligned} \tag{62}$$

Likewise,

$$\begin{aligned} \|W^{(\ell)} \Delta\phi(h^{(\ell-1)})\|_2^2 &= \Theta\left(\frac{d_\ell}{d_{\ell-1}} \|\Delta\phi(h^{(\ell-1)})\|_2^2 \right) \\ &= \mathcal{O}\left(\frac{d_\ell}{d_{\ell-1}} \|\Delta h^{(\ell-1)}\|_2^2 \right) \\ &\qquad \text{(Lipschitz activation function).} \end{aligned} \tag{63}$$

To write the term, $\Delta W^{(\ell)} \Delta\phi(h^{(\ell-1)})$, we can decompose the weight update $\Delta W^{(\ell)}$ and use the lmo expression of Equation (41), to get

$$\begin{aligned} \Delta W^{(\ell)} \Delta\phi(h^{(\ell-1)}) = & -\gamma\rho^{(\ell)} \sqrt{\frac{d_\ell}{d_{\ell-1}}} \frac{(\frac{\partial \mathcal{L}}{\partial h^{(\ell)}})}{\|\frac{\partial \mathcal{L}}{\partial h^{(\ell)}}\|_2} \frac{\phi(h^{(\ell-1)})^\top}{\|\phi(h^{(\ell-1)})\|_2} \Delta\phi(h^{(\ell-1)}) \\ & - \gamma W^{(\ell)} \Delta\phi(h^{(\ell-1)}). \end{aligned}$$

So,

$$\begin{aligned}\|\Delta W^{(\ell)}\Delta\phi(h^{(\ell-1)})\|_2^2 &= \mathcal{O}\left(\gamma^2\frac{d_\ell}{d_{\ell-1}}\left\|\frac{(\frac{\partial\mathcal{L}}{\partial h^{(\ell)}})}{\|\frac{\partial\mathcal{L}}{\partial h^{(\ell)}}\|_2}\frac{\phi(h^{(\ell-1)})^\top}{\|\phi(h^{(\ell-1)})\|_2}\Delta\phi(h^{(\ell-1)})\right\|_2^2\right.\\ &\quad\left.+\gamma^2\|W^{(\ell)}\Delta\phi(h^{(\ell-1)})\|_2^2\right)\\ &= \mathcal{O}\left(\gamma^2\frac{d_\ell}{d_{\ell-1}}\left\|\frac{(\frac{\partial\mathcal{L}}{\partial h^{(\ell)}})}{\|\frac{\partial\mathcal{L}}{\partial h^{(\ell)}}\|_2}\frac{\phi(h^{(\ell-1)})^\top}{\|\phi(h^{(\ell-1)})\|_2}\Delta\phi(h^{(\ell-1)})\right\|_2^2\right.\\ &\quad\left.+\gamma^2\frac{d_\ell}{d_{\ell-1}}\|\Delta\phi(h^{(\ell-1)})\|_2^2\right).\end{aligned}$$

By using the fact that the activation function ϕ is Lipschitz, we have

$$\begin{aligned}\|\Delta W^{(\ell)}\Delta\phi(h^{(\ell-1)})\|_2^2 &= \mathcal{O}\left(\gamma^2\frac{d_\ell}{d_{\ell-1}}\left\|\frac{(\frac{\partial\mathcal{L}}{\partial h^{(\ell)}})}{\|\frac{\partial\mathcal{L}}{\partial h^{(\ell)}}\|_2}\frac{\phi(h^{(\ell-1)})^\top}{\|\phi(h^{(\ell-1)})\|_2}\Delta\phi(h^{(\ell-1)})\right\|_2^2\right.\\ &\quad\left.+\gamma^2\frac{d_\ell}{d_{\ell-1}}\|\Delta h^{(\ell-1)}\|_2^2\right).\end{aligned}$$

We rewrite the first term and use the Lipschitz continuity of the activation function ϕ, to get

$$\begin{aligned}\gamma^2\frac{d_\ell}{d_{\ell-1}}\left\|\frac{(\frac{\partial\mathcal{L}}{\partial h^{(\ell)}})}{\|\frac{\partial\mathcal{L}}{\partial h^{(\ell)}}\|_2}\frac{\phi(h^{(\ell-1)})^\top}{\|\phi(h^{(\ell-1)})\|_2}\Delta\phi(h^{(\ell-1)})\right\|_2^2 &= \Theta\left(\gamma^2\frac{d_\ell}{d_{\ell-1}}\|\Delta\phi(h^{(\ell-1)})\|_2^2\right)\\ &= \mathcal{O}\left(\gamma^2\frac{d_\ell}{d_{\ell-1}}\|\Delta h^{(\ell-1)}\|_2^2\right).\end{aligned}$$

Therefore,

$$\begin{aligned}\|\Delta W^{(\ell)}\Delta\phi(h^{(\ell-1)})\|_2^2 &= \mathcal{O}\left(\gamma^2\frac{d_\ell}{d_{\ell-1}}\|\Delta h^{(\ell-1)}\|_2^2+\gamma^2\frac{d_\ell}{d_{\ell-1}}\|\Delta h^{(\ell-1)}\|_2^2\right)\\ &= \mathcal{O}\left(2\gamma^2\frac{d_\ell}{d_{\ell-1}}\|\Delta h^{(\ell-1)}\|_2^2\right).\end{aligned}$$

Finally, we can incorporate all these derivated terms into the expression of $\|\Delta h^{(\ell)}\|_2^2$ from Equation (60), and we have

$$\begin{aligned}\|\Delta h^{(\ell)}\|_2^2 &= \Theta\left(\gamma^2\|W^{(\ell)}\phi(h^{(\ell-1)})\|_2^2+\gamma^2\frac{d_\ell}{d_{\ell-1}}\|\phi(h^{(\ell-1)})\|_2^2\right.\\ &\quad\left.+\|W^{(\ell)}\Delta\phi(h^{(\ell-1)})\|_2^2+\|\Delta W^{(\ell)}\Delta\phi(h^{(\ell-1)})\|_2^2\right)\\ &= \mathcal{O}\left(\gamma^2 d_\ell+\gamma^2 d_\ell+\frac{d_\ell}{d_{\ell-1}}\|\Delta h^{(\ell-1)}\|_2^2\right.\\ &\quad\left.+2\gamma^2\frac{d_\ell}{d_{\ell-1}}\|\Delta h^{(\ell-1)}\|_2^2\right).\end{aligned}$$

Thus,

$$\|\Delta h^{(\ell)}\|_2^2 = \mathcal{O}\left(2\gamma^2 d_\ell+(1+2\gamma^2)\frac{d_\ell}{d_{\ell-1}}\|\Delta h^{(\ell-1)}\|_2^2\right). \tag{64}$$

By induction, we can show that

$$\begin{aligned}\|\Delta h^{(\ell)}\|_2^2 &= \mathcal{O}\left(d_\ell \times (2\gamma^2)(1+\sum_{j=1}^{\ell-1}(1+2\gamma^2)^j)\right)\\ &= \mathcal{O}\left(d_\ell \times (2\gamma^2)(\sum_{j=0}^{\ell-1}(1+2\gamma^2)^j)\right).\end{aligned}$$

We provide here the details of the recursion:

• Initialization: For $\ell = 1$, we have:

$$\begin{aligned}\|\Delta h^{(1)}\|_2^2 &= \mathcal{O}\left(2\gamma^2 d_1 + (1+2\gamma^2)\frac{d_1}{d_{\text{in}}}\|\Delta x\|_2^2\right)\\ &= \mathcal{O}\left(2\gamma^2 d_1\right).\end{aligned}$$

• Induction step: Let us suppose that $\|\Delta h^{(\ell)}\|_2^2 = \mathcal{O}\left(d_\ell \times (2\gamma^2)(1+\sum_{j=1}^{\ell-1}(1+2\gamma^2)^j)\right)$.

Then:

$$\begin{aligned}\|\Delta h^{(\ell+1)}\|_2^2 &= \mathcal{O}\left(2\gamma^2 d_{\ell+1} + (1+2\gamma^2)\frac{d_{\ell+1}}{d_\ell}\|\Delta h^{(\ell)}\|_2^2\right) \quad \text{(from Equation (64))}\\ &= \mathcal{O}\left(2\gamma^2 d_{\ell+1} + (1+2\gamma^2)\frac{d_{\ell+1}}{d_\ell} \times d_\ell \times (2\gamma^2)(1+\sum_{j=1}^{\ell-1}(1+2\gamma^2)^j)\right)\\ &\quad \text{(heredity hypothesis)}\\ &= \mathcal{O}\left(2\gamma^2 d_{\ell+1} + (1+2\gamma^2) d_{\ell+1} \times (2\gamma^2)(1+\sum_{j=1}^{\ell-1}(1+2\gamma^2)^j)\right)\\ &= \mathcal{O}\left(2\gamma^2 d_{\ell+1} \times \left(1 + (1+2\gamma^2) \times (1+\sum_{j=1}^{\ell-1}(1+2\gamma^2)^j)\right)\right)\\ &= \mathcal{O}\left(2\gamma^2 d_{\ell+1} \times \left(1 + (1+2\gamma^2) \times (\sum_{j=0}^{\ell-1}(1+2\gamma^2)^j)\right)\right)\\ &= \mathcal{O}\left(2\gamma^2 d_{\ell+1} \times \left(1 + (\sum_{j=0}^{\ell-1}(1+2\gamma^2)^{j+1})\right)\right)\\ &= \mathcal{O}\left(2\gamma^2 d_{\ell+1} \times (1+\sum_{j=1}^{\ell}(1+2\gamma^2)^j)\right),\end{aligned}$$

which completes the proof by induction.

Also, since $\|W^{(\ell)}\Delta\phi(h^{(\ell-1)})\|_2^2 + \|\Delta W^{(\ell)}\Delta\phi(h^{(\ell-1)})\|_2^2 \geq 0$, we have

$$\|\Delta h^{(\ell)}\|_2^2 = \Omega\left(2\gamma^2 d_\ell\right).$$

Then, we have, by symmetry

$$\Delta h_i^{(\ell)^2} = \frac{1}{d_\ell}\|\Delta h^{(\ell)}\|_2^2 = \mathcal{O}\left(2\gamma^2 \sum_{j=0}^{\ell-1}(1+2\gamma^2)^j\right).$$

Thus,

$$\Delta h_i^{(\ell)^2} = \frac{1}{d_\ell}\|\Delta h^{(\ell)}\|_2^2 = \Omega\left(2\gamma^2\right).$$

Therefore, we have the maximal update condition since $\Delta h_i^{(\ell)^2} = \Theta(1)$ with respect to the width of the layer d_ℓ. Also, the optimal learning rate satisfying this condition is independent of the hidden-layer widths.

□

D.2 Proof from Section 4.3.1

Before proving Proposition 4, we first establish the following lemma.

Lemma 1 (Norm control)**.** *For every vector v and matrix A with the clipping interval $[a, b]$ fixed independently of the width, we have*

$$\|\text{spectral_clip}_{[a,b]}(A)v\|_2^2 = \Theta(\|v\|_2^2). \tag{65}$$

Proof. Let $M = \text{spectral_clip}_{[a,b]}(A)$. Let us denote $A = U\Sigma V^\top$ and $M = U\Lambda V^\top$ the singular value decompositions of A and M respectively with U, V orthogonal, $\Sigma = \text{diag}(\sigma_i)$ the diagonal matrix containing the singular values of A and its clipped version $\Lambda = \text{diag}(\lambda_i)$ with $\lambda_i = \text{clip}_{[a,b]}\sigma_i$. Let us also denote $w = V^\top v$. Then,

$$\begin{aligned} \|\Lambda w\|_2^2 &= \sum_i \lambda_i^2 w_i^2 \\ \text{and } a^2\|w\|_2^2 \le \|\Lambda w\|_2^2 &\le b^2\|w\|_2^2. \end{aligned} \tag{66}$$

Since $\|w\|_2^2 = \|v\|_2^2$, we have $a^2\|v\|_2^2 \le \|\Lambda V^\top v\|_2^2 \le b^2\|v\|_2^2$. Then, by isometry of the orthogonal matrix U, we can conclude with

$$\begin{aligned} &a^2\|v\|_2^2 \le \|U\Lambda V^\top v\|_2^2 \le b^2\|v\|_2^2 \\ \text{i.e.}\quad &a^2\|v\|_2^2 \le \|\text{spectral_clip}_{[a,b]}(A)v\|_2^2 \le b^2\|v\|_2^2. \end{aligned} \tag{67}$$

□

Proposition 4 (Width-wise stability of Projected Scion)**.** *Under the assumptions defined in Sections 3.4.2 and 4.1.2, the feature updates after a step of* Projected Scion *admit an upper bound that is independent of the width d_ℓ. In particular, for each layer ℓ,*

$$\|\Delta h^{(\ell)}\|_2^2 = \mathcal{O}(d_\ell) \tag{36}$$

with respect to the width d_ℓ.

Proof. With the projected version of Scion on an interval $[a, b]$, the update can be written as

$$W_{t+1}^{(\ell)} = \text{spectral_clip}_{[a,b]}(W_t^{(\ell)} + \gamma\,\text{lmo}[\nabla_{W_t^{(\ell)}}\mathcal{L}]). \tag{68}$$

Moreover, by definition of the spectral clipping, if a and b are fixed independently of the width (meaning $a, b = \Theta(1)$), we have, for any matrix A,

$$\|\text{spectral_clip}_{[a,b]}(A)\|_{\mathcal{S}_\infty}^2 = \Theta(1). \tag{69}$$

In the following, we cannot apply this argument as it is to matrices for which we are interested in their scaling with the width. As the width scales, the spectral norm of the matrix could vanish, and, depending on the choice of a, we have no guarantee that the spectral norm will remain of constant order with respect to the width. Therefore, we will use:

$$\|\text{spectral_clip}_{[a,b]}(A)\|_{\mathcal{S}_\infty}^2 = \mathcal{O}(1). \tag{70}$$

As in the derivations with the Scion update from Appendix D.1, we want to evaluate

$$\|\Delta h^{(\ell)}\|_2^2 = \Theta\left(\|\Delta W^{(\ell)}\phi(h^{(\ell-1)})\|_2^2 + \|W^{(\ell)}\Delta\phi(h^{(\ell-1)})\|_2^2 + \|\Delta W^{(\ell)}\Delta\phi(h^{(\ell-1)})\|_2^2\right). \tag{71}$$

The second term can be computed straightforwardly to end up with

$$\|W^{(\ell)}\Delta\phi(h^{(\ell-1)})\|_2^2 = \mathcal{O}\left(\frac{d_\ell}{d_{\ell-1}}\|\Delta h^{(\ell-1)}\|_2^2\right). \tag{72}$$

For the first term, we have

$$\begin{aligned}
\|\Delta W^{(\ell)}\phi(h^{(\ell-1)})\|_2^2 &= \|(\text{spectral_clip}_{[a,b]}(W^{(\ell)} + \gamma\,\text{lmo}(\nabla_{W^{(\ell)}}\mathcal{L})) - W^{(\ell)})\phi(h^{(\ell-1)})\|_2^2 \\
&= \mathcal{O}\left(\|\text{spectral_clip}_{[a,b]}(W^{(\ell)} + \gamma\,\text{lmo}(\nabla_{W^{(\ell)}}\mathcal{L}))\phi(h^{(\ell-1)})\|_2^2 + \|W^{(\ell)}\phi(h^{(\ell-1)})\|_2^2\right) \\
&\quad \text{from Equation (78)} \\
&= \mathcal{O}\left(\|\phi(h^{(\ell-1)})\|_2^2 + \|W^{(\ell)}\phi(h^{(\ell-1)})\|_2^2\right) \\
&\quad \text{(from Equation (65))} \\
&= \mathcal{O}\left(\|h^{(\ell-1)}\|_2^2 + \|W^{(\ell)}\|_{\mathcal{S}_\infty}^2\|\phi(h^{(\ell-1)})\|_2^2\right) \\
&\quad \text{(scale of activation function Equation (13) and alignment assumption Equation (14))} \\
&= \mathcal{O}(d_{\ell-1} + \frac{d_\ell}{d_{\ell-1}}d_{\ell-1}) \\
&= \mathcal{O}(d_{\ell-1} + d_\ell).
\end{aligned} \tag{73}$$

For the third term, we have

$$\begin{aligned}
\left\|\Delta W^{(\ell)}\Delta\phi(h^{(\ell-1)})\right\|_2^2 &= \left\|\text{spectral_clip}_{[a,b]}\left(W_t^{(\ell)} + \gamma\,\text{lmo}(\nabla_{W_t^{(\ell)}}\mathcal{L})\right)\Delta\phi(h^{(\ell-1)}) - W_t^{(\ell)}\Delta\phi(h^{(\ell-1)})\right\|_2^2 \\
&= \mathcal{O}\left(\left\|\text{spectral_clip}_{[a,b]}\left(W_t^{(\ell)} + \gamma\,\text{lmo}(\nabla_{W_t^{(\ell)}}\mathcal{L})\right)\Delta\phi(h^{(\ell-1)})\right\|_2^2 + \left\|W_t^{(\ell)}\Delta\phi(h^{(\ell-1)})\right\|_2^2\right) \\
&\quad \text{from Equation (78)} \\
&= \mathcal{O}\left(\left\|\Delta\phi(h^{(\ell-1)})\right\|_2^2 + \left\|W_t^{(\ell)}\Delta\phi(h^{(\ell-1)})\right\|_2^2\right) \\
&\quad \text{(from Equation (65))} \\
&= \mathcal{O}\left((1 + \frac{d_\ell}{d_{\ell-1}})\|\Delta h^{(\ell-1)}\|_2^2\right). \\
&\quad \text{(from the Lipschitz continuity of } \phi \text{ and we re-use the bound of Equation (72)).}
\end{aligned} \tag{74}$$

Therefore,

$$\|\Delta h^{(\ell)}\|_2^2 = \mathcal{O}\left(d_\ell + d_{\ell-1} + (1 + \frac{d_\ell}{d_{\ell-1}})\|\Delta h^{(\ell-1)}\|_2^2\right). \tag{75}$$

With the assumption that d_ℓ and $d_{\ell-1}$ are of the same order, and by induction, we have

$$\|\Delta h^{(\ell)}\|_2^2 = \mathcal{O}(d_\ell). \tag{76}$$

□

Proposition 4 establishes an upper bound on the feature updates but lacks a lower bound. The lower bound argument used for Scion without projections relies on a non-cancellation assumption that does not hold after spectral clipping. In particular, at some point of the proof, we would need to have the following assumption

$$\begin{aligned}
&\left\|\left(\text{spectral_clip}_{[a,b]}(W^{(\ell)} + \gamma\,\text{lmo}(M_t^{(\ell)})) - W^{(\ell)}\right)\phi(h^{(\ell-1)})\right\|_2^2 \\
=\ &\Theta\left(\|\text{spectral_clip}_{[a,b]}(W^{(\ell)} + \gamma\,\text{lmo}(M_t^{(\ell)}))\phi(h^{(\ell-1)})\|_2^2 + \|W^{(\ell)}\phi(h^{(\ell-1)})\|_2^2\right),
\end{aligned} \tag{77}$$

which does not hold in practice (see for instance Figure 17). Indeed, if the learning rate is too small, the left term cancels and the lower bound does not hold. Therefore, we only have:

$$\begin{aligned} &\left\| \left(\text{spectral_clip}_{[a,b]}(W^{(\ell)} + \gamma\, \text{lmo}(M_t^{(\ell)})) - W^{(\ell)} \right) \phi(h^{(\ell-1)}) \right\|_2^2 \\ = \;& \mathcal{O}\left(\|\text{spectral_clip}_{[a,b]}(W^{(\ell)} + \gamma\, \text{lmo}(M_t^{(\ell)}))\phi(h^{(\ell-1)})\|_2^2 + \|W^{(\ell)}\phi(h^{(\ell-1)})\|_2^2 \right). \end{aligned} \tag{78}$$

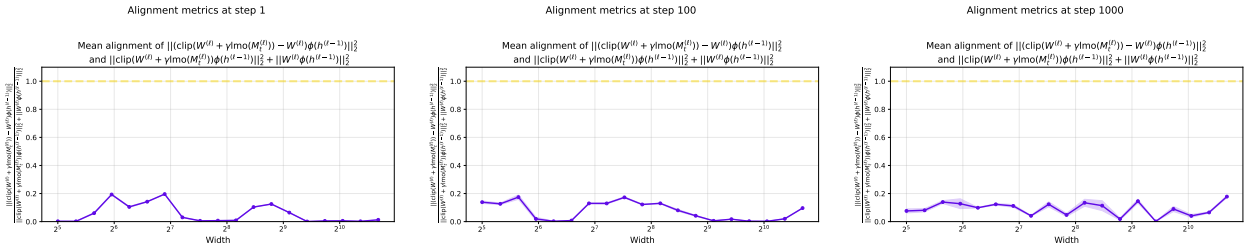


Figure 17: Cancellation of the clipping update of $W^{(\ell)}\phi(h^{(\ell-1)})$ and the current features. The network is an MLP trained with Projected Scion on CIFAR-10, over 5 trials. The layer of interest is the second hidden layer. The plots are shown at different training steps and across a wide range of network widths. Experimental details can be found in Table 8.

E CompleteP style analysis

In this part, we analyze the scaling behavior of the network's hidden states using the heuristics found in Dey et al. (2026). Hence, the $Z^{(\ell)}$ matrices are not learned and are fixed as identity. The hidden-layer width is constant, and training is restricted to the $W^{(\ell)}$ operators.

CompleteP assumptions Following the analysis of Dey et al. (2026), we will assume that for every step t, hidden representations from different iterations have constant-order correlations, normalized gradients remain strongly aligned across layers, and gradients from different optimization steps are asymptotically uncorrelated. That is,

$$\phi(h_t^{(\ell)})^\top \phi(h_{t'}^{(\ell)}) = \Theta(d_\ell) \qquad \forall \ell, \forall (t, t'), \tag{79}$$

and, denoting $g_t^{(\ell)} = \frac{\partial \mathcal{L}}{\partial h_t^{(\ell)}}$,

$$\left\langle \frac{g_t^{(\ell)}}{\|g_t^{(\ell)}\|}, \frac{g_t^{(k)}}{\|g_t^{(k)}\|} \right\rangle = \Theta(1) \qquad \forall (\ell, k), \forall t, \tag{80}$$

while gradients from different steps are uncorrelated.

Proposition 5. *For all iterations $t > 0$, under the CompleteP correlation assumptions, the normalized squared ℓ_2-norm change of the final layer hidden state satisfies:*

$$\frac{1}{d_L} \|\Delta h_t^{(L)}\|_2^2 = \Theta(1).$$

Proof. Let $t > 0$ and write the definition of $h^{(L)}(t)$ to get

$$h_t^{(L)} = h_t^{(0)} + L^{-\alpha} \sum_{\ell=0}^{L-1} W_t^{(\ell)} \phi(h_t^{(\ell)}).$$

Inserting $W_t^{(\ell)} = W_0^{(\ell)} + \sum_{t<t'} \Delta W_{t'}^{(\ell)}$ (unrolling the recursion) then gives

$$h_t^{(L)} = h_t^{(0)} + L^{-\alpha} \sum_{\ell=0}^{L-1} W_0^{(\ell)} \phi(h_t^{(\ell)}) + \underbrace{L^{-\alpha} \sum_{\ell=0}^{L-1} \sum_{t'<t} \Delta W_{t'}^{(\ell)} \phi(h_t^{(\ell)})}_{\Delta h_t^{(L)}}.$$

In CompleteP Desideratum 2 (Dey et al., 2026), they aim to show that $\|\Delta h_t^{(L)}\|_{RMS}^2 = \Theta(1)$ for all $t > 0$. Using Unconstrained Scion, the update has the form

$$\Delta W_{t'}^{(\ell)} = W_{t'+1}^{(\ell)} - W_{t'}^{(\ell)} = \gamma \frac{g_{t'}^{(\ell+1)}}{\|g_{t'}^{(\ell+1)}\|_2} \left[\frac{\phi(h_{t'}^{(\ell)})}{\|\phi(h_{t'}^{(\ell)})\|_2} \right]^\top.$$

Plugging this into the expression for $\Delta h_t^{(L)}$, we find

$$\Delta h_t^{(L)} = L^{-\alpha} \sum_{\ell=0}^{L-1} \sum_{t'<t} \gamma \frac{g_{t'}^{(\ell+1)}}{\|g_{t'}^{(\ell+1)}\|_2} \left[\frac{\phi(h_{t'}^{(\ell)})}{\|\phi(h_{t'}^{(\ell)})\|_2} \right]^\top \phi(h_t^{(\ell)}).$$

Note that, for each ℓ, CompleteP claims that the coordinates of $\phi(h_t^{(\ell)})$ and $\phi(h_{t'}^{(\ell)})$ have $\Theta(1)$ correlation, so that $\phi(h_{t'}^{(\ell)})^\top \phi(h_t^{(\ell)}) = \Theta(d_\ell)$, while $\|\phi(h^{(\ell)}(t'))\|_2 = \Theta(\sqrt{d_\ell})$. We also make this correlation assumption here (Equation (79)), and, by taking the norm squared and applying this yields

$$\begin{aligned}
\|\Delta h_t^{(L)}\|_2^2 &= L^{-2\alpha} \left\| \sum_{\ell=0}^{L-1} \sum_{t'<t} \gamma \frac{g_{t'}^{(\ell+1)}}{\|g_{t'}^{(\ell+1)}\|_2} \left[\frac{\phi(h_{t'}^{(\ell)})}{\|\phi(h_{t'}^{(\ell)})\|_2} \right]^\top \phi(h_t^{(\ell)}) \right\|_2^2 \\
&= L^{-2\alpha} \gamma^2 d_L \left\| \sum_{\ell=0}^{L-1} \sum_{t'<t} \frac{g_{t'}^{(\ell+1)}}{\|g_{t'}^{(\ell+1)}\|_2} \right\|_2^2 \\
&= L^{-2\alpha} \gamma^2 d_L \Theta(L^2)
\end{aligned}$$

where the last equality follows because the layer gradients are strongly correlated across layers but uncorrelated across time steps (Equation (80)).

Hence, with $\gamma = \gamma_{\text{base}} L^{\alpha-1}$, we have $\|\Delta h_t^{(L)}\|_2^2 = \Theta(d_L)$, and therefore $\frac{1}{d_L}\|\Delta h_t^{(L)}\|_2^2 = \Theta(1)$.

Note that for a sign update with the CompleteP scaling (Dey et al., 2026), we would get $1/L^2$ for the RMS norm squared of the update.

□

F Coordinate Checks on nanoGPT

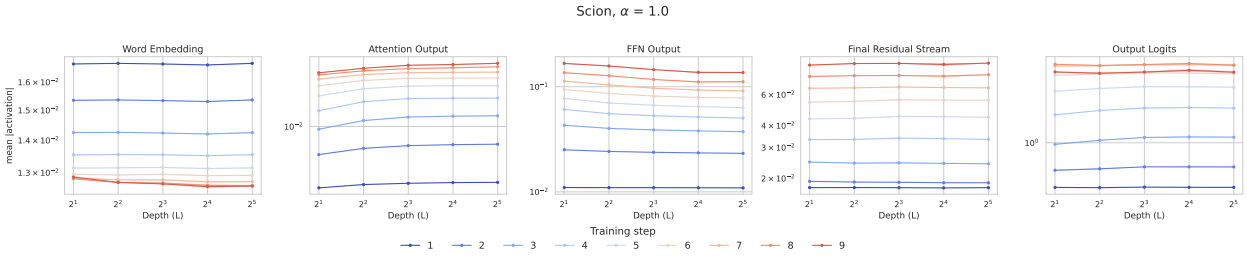


Figure 18: Coordinate check for SCION, on FineWeb, with $\alpha = 1.0$, and base learning rate $\gamma_{\text{base}} = 2^{-11}$.

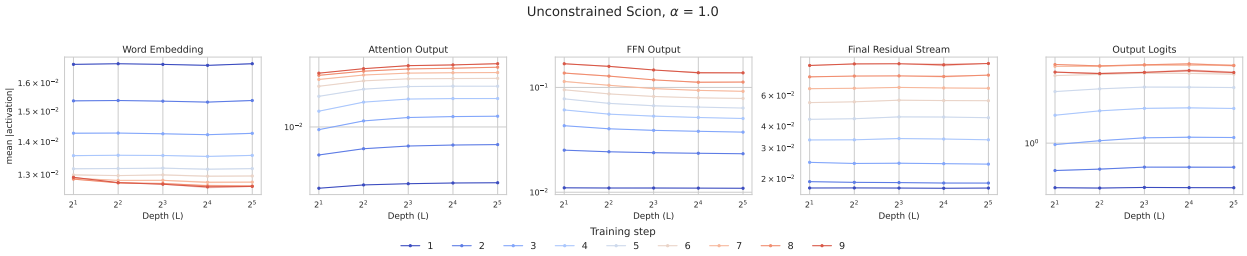


Figure 19: Coordinate check for UNCONSTRAINED SCION, on FineWeb, with $\alpha = 1.0$, and base learning rate $\gamma_{\text{base}} = 2^{-11}$.

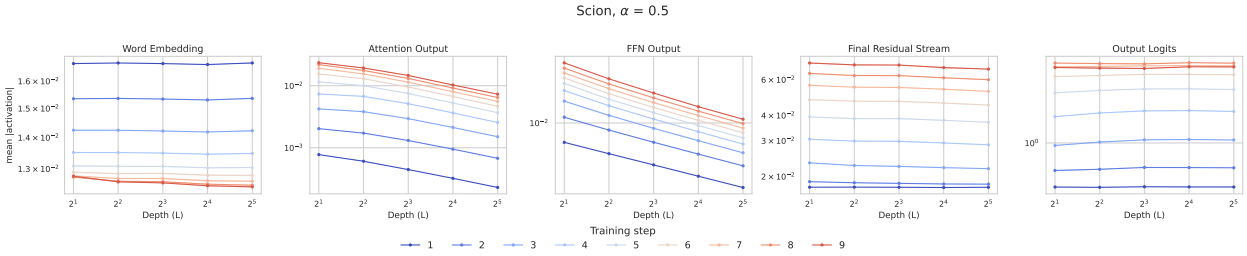


Figure 20: Coordinate check for SCION, on FineWeb, with $\alpha = 0.5$, and base learning rate $\gamma_{\text{base}} = 2^{-11}$.

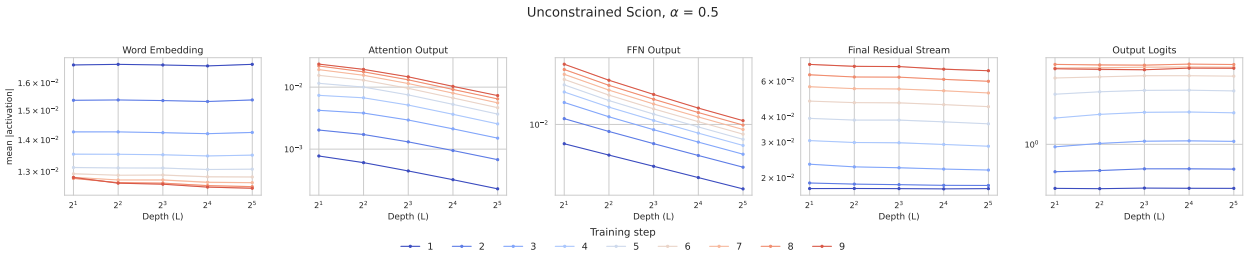


Figure 21: Coordinate check for UNCONSTRAINED SCION, on FineWeb, with $\alpha = 0.5$, and base learning rate $\gamma_{\text{base}} = 2^{-11}$.

G Additional Experiments

G.1 NanoGPT with Z

To further evaluate the proposed depth-wise learning rate scaling developed in the analysis of Section 3 when the matrices $Z^{(\ell)}$ are trained, we repeat the nanoGPT experiments while learning $Z^{(\ell)}$ in every hidden layer. As shown in Figure 22, the loss curves remain approximately parallel and their minima occur at similar base learning rates across depths, providing empirical evidence that the proposed learning rate scaling transfers when $Z^{(\ell)}$ is learned.

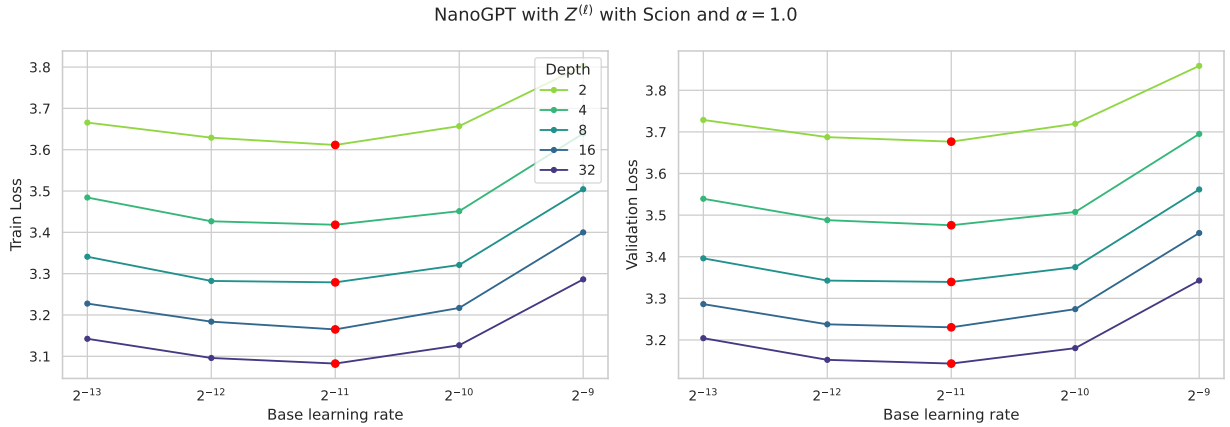


Figure 22: Scion on nanoGPT with $Z^{(\ell)}$ trained on FineWeb, with $\alpha = 1$, on 1 seed. Well depth-aligned and parallel loss curves indicate that the optimal base learning rate remains invariant with depth. The experimental details are the same as in Table 2, and the $Z^{(\ell)}$ matrices are therefore of shape 768×768 for every hidden layer ℓ.

G.2 NanoGPT without any scale of the learning rates

To assess whether the depth-dependent learning rate scaling is necessary for transfer, we repeat the nanoGPT depth sweep without applying any depth-dependent correction. The results are displayed in Figure 23, where we observe that the optimal learning rate shifts as the depth increases, in contrast to the approximately depth-invariant optimum obtained with the proposed scaling. This empirically shows that removing the prescribed learning rate scalings leads to a loss of depth-wise transfer. We test $\alpha = 1/2$ since, for $\alpha = 1$, the scaling factor is just 1.

G.3 Variability across seeds

To further assess the stability across depth observed in the experiments, we plot in Figures 24 and 25 the optimal learning rate for each depth, together with error bars capturing the variability across three seeds.

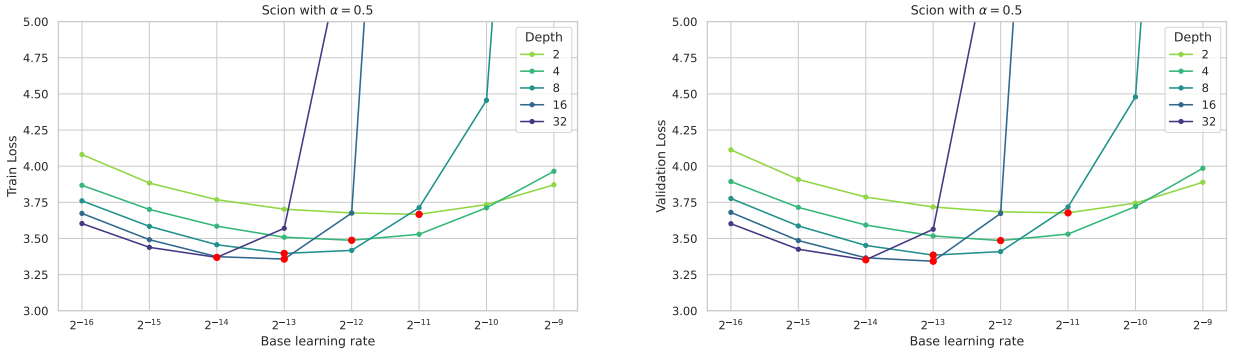


Figure 23: SCION on nanoGPT with $Z^{(\ell)}$ trained on FineWeb, with $\alpha = 0.5$, without any scaling of the learning rates ($\gamma = \gamma_{\text{base}}$ and $\gamma_Z = \gamma_{Z\,\text{base}}$), on 1 seed. We observe the shift of the optimal learning rate as depth increases. The experimental details are in Table 2.

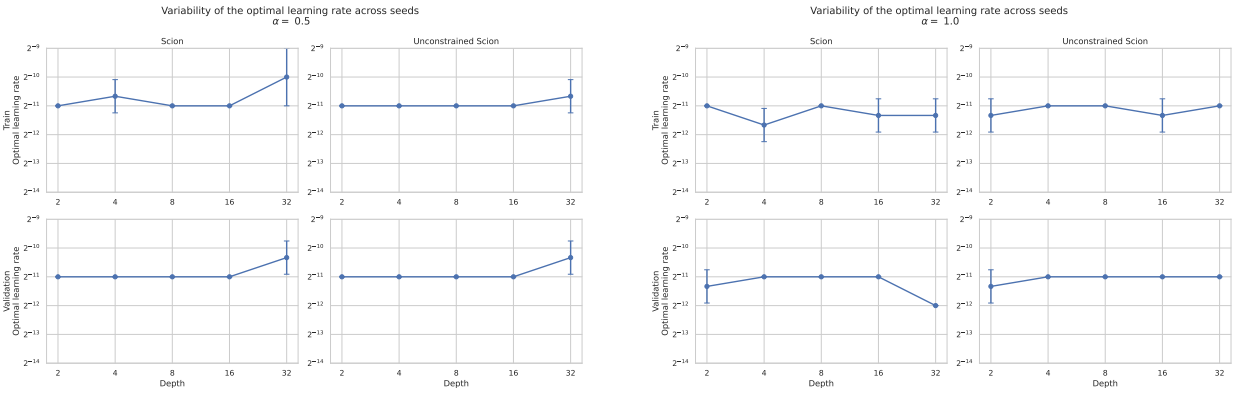


Figure 24: Variability across seeds of the optimal learning rates per depths with SCION and UNCONSTRAINED SCION for $\alpha = 0.5$ (*left plots*) and $\alpha = 1$ (*right plots*) on nanoGPT trained on FineWeb. The experimental details are in Table 2.

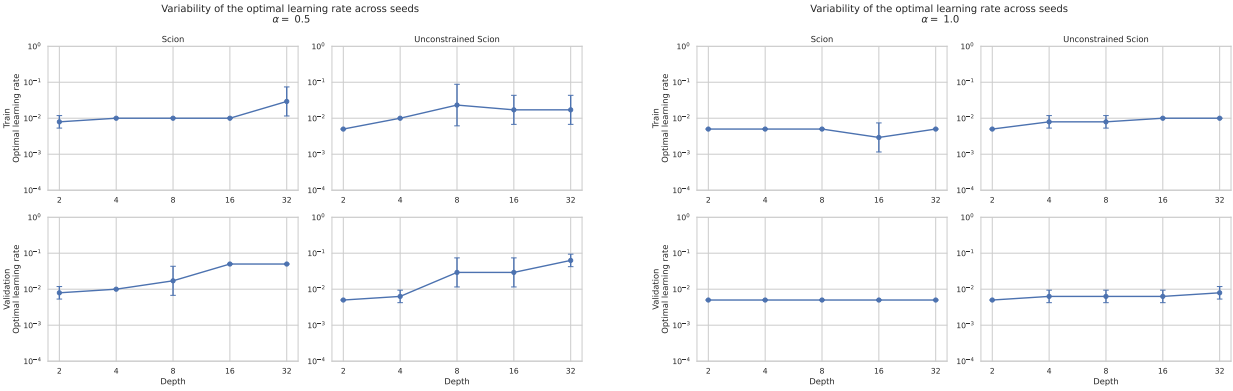


Figure 25: Variability across seeds of the optimal learning rates per depths with SCION and UNCONSTRAINED SCION for $\alpha = 0.5$ (*left plots*) and $\alpha = 1$ (*right plots*) on MLP-Mixer trained on CIFAR-10. The experimental details are in Table 5.

H Weight alignment and non-cancellation

The experiments presented below are performed under a training regime that is closer to standard practice than the one adopted in Yang et al. (2023a). Our implementation builds on the code provided by the authors, where we modify the experimental setup so that all network layers are updated jointly over multiple optimization steps. By contrast, the experiments in Yang et al. (2023a) are restricted to a single optimization step, with only the layer of interest being updated and all remaining layers held fixed.

H.1 Alignment of the weights with the incoming vector

In Figure 26, we report

$$\frac{\|W^{(\ell)}\phi(h^{(\ell-1)})\|_2}{\|W^{(\ell)}\|_{\mathcal{S}_\infty}\|\phi(h^{(\ell-1)})\|_2} \quad \text{and} \quad \frac{\|Z^{(\ell)}\phi(h^{(\ell-1)})\|_2}{\|Z^{(\ell)}\|_{\mathcal{S}_\infty}\|\phi(h^{(\ell-1)})\|_2} \tag{81}$$

for various depths and iteration steps.

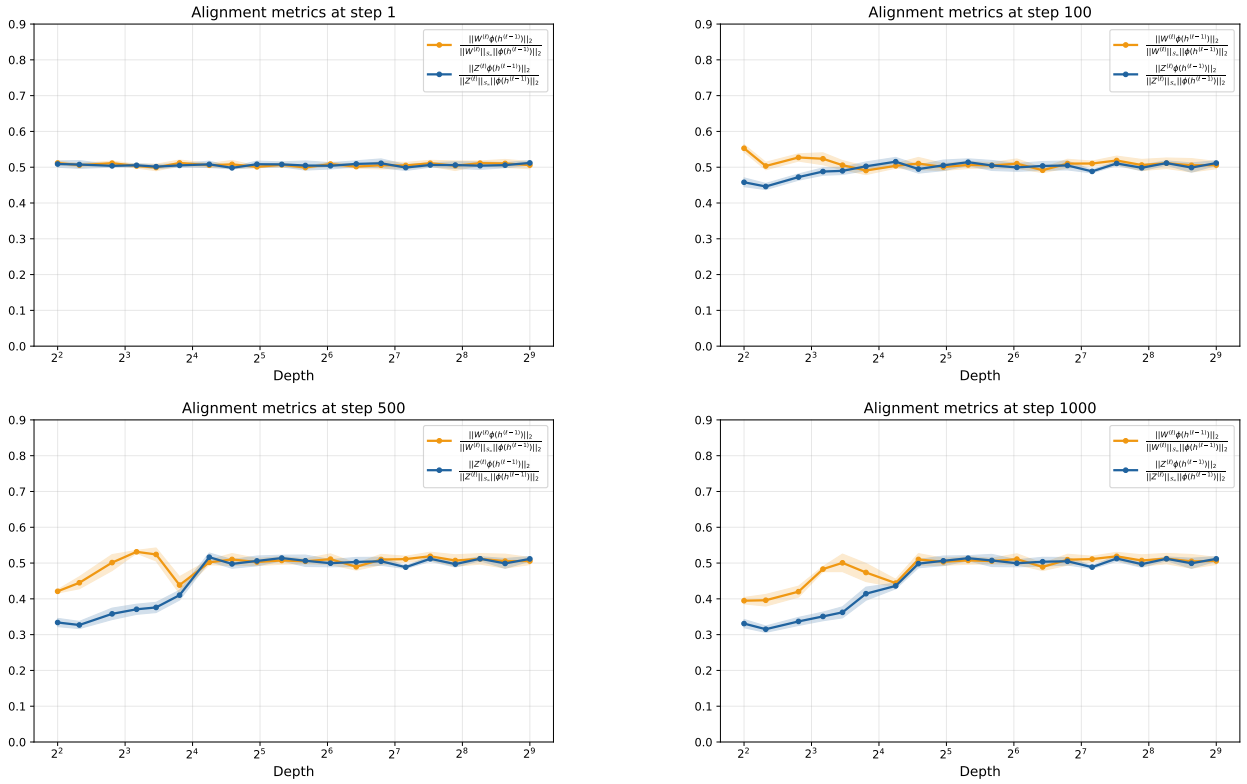


Figure 26: Alignment of weights $W^{(\ell)}$ and $Z^{(\ell)}$ with the vector $\phi(h^{(\ell-1)})$, across a wide range of depths L, on CIFAR-10. Both $W^{(\ell)}$ and $Z^{(\ell)}$ exhibit strong alignment regardless of depth. The network is a ResNet where we learn the matrices $Z^{(\ell)}$, trained with Unconstrained Scion on CIFAR-10, on 5 trials. The layer of interest here is the third hidden layer. Experimental details can be found in Table 7.

These experiments provide an empirical assessment of Assumption 14 beyond initialization and throughout training.

H.2 Alignment of the sum of the residual block with the previous state

In Figure 27, we report

$$\frac{\|h^{(\ell)}\|_2^2}{\|Z^{(\ell)}h^{(\ell-1)}\|_2^2 + \frac{1}{L^{2\alpha}}\|W^{(\ell)}\phi(h^{(\ell-1)})\|_2^2}. \tag{82}$$

for various depths and iteration steps.

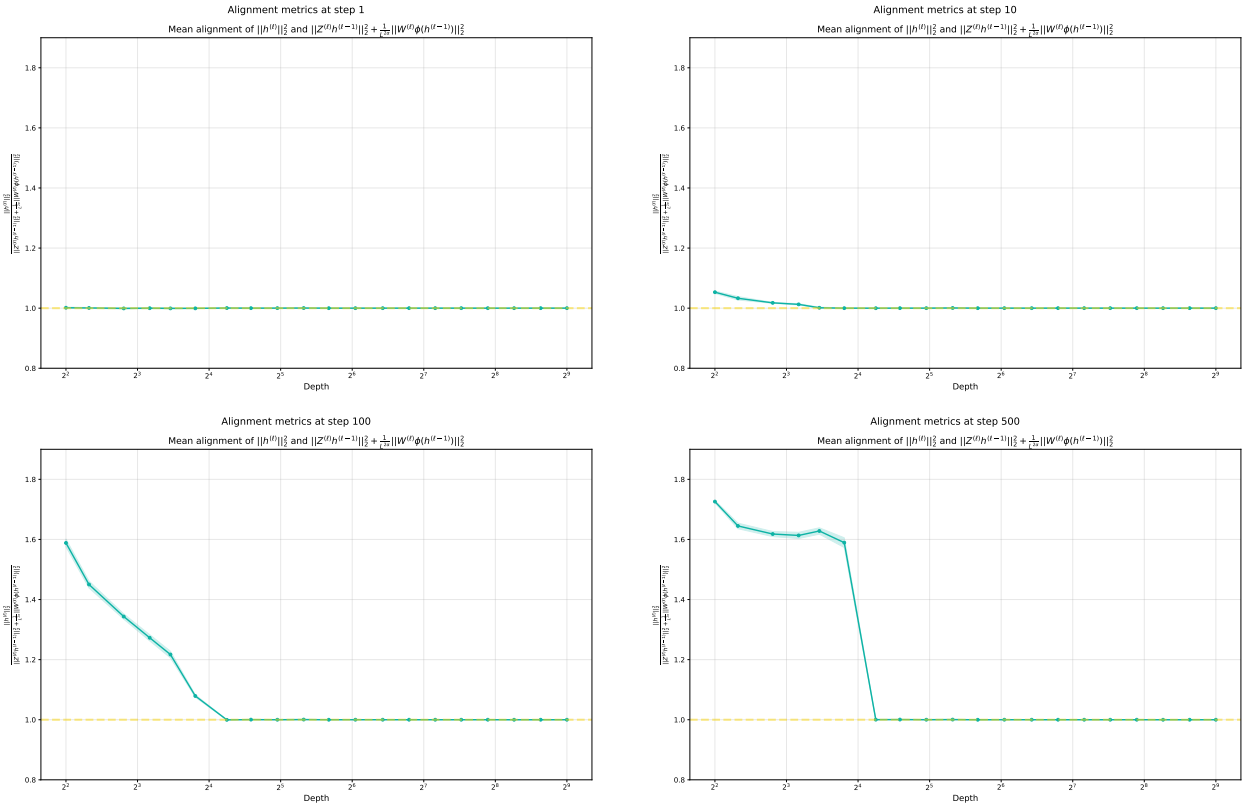


Figure 27: Alignment of the hidden features $h^{(\ell)}$ with the sum of the previous block and the residual block, scaled by the factor $L^{-\alpha}$, across a wide range of depths L, on CIFAR-10. Despite the non stability we observe at small depth, we still note that the ratio is always above 1, which empirically shows that the lower bound holds. The network is a ResNet where we learn the matrices $Z^{(\ell)}$, trained with Unconstrained Scion on CIFAR-10, on 5 trials. The layer of interest here is the third hidden layer. Experimental details can be found in Table 7.

H.3 Alignment of the updates of the layer with Unconstrained Scion

In Figure 28, we report

$$\frac{\|\Delta_{W^{(\ell)},Z^{(\ell)}} h^{(\ell)}\|_2^2}{\|\Delta Z^{(\ell)} h^{(\ell-1)}\|_2^2 + \frac{1}{L^{2\alpha}} \|\Delta W^{(\ell)} \phi(h^{(\ell-1)})\|_2^2} \tag{83}$$

for various depths and iteration steps, where the weights are updated with Unconstrained Scion.

H.4 Alignment of the updates of the layer with Scion

In Figure 29, we report

$$\frac{\|\Delta_{W^{(\ell)},Z^{(\ell)}} h^{(\ell)}\|_2^2}{\|\Delta Z^{(\ell)} h^{(\ell-1)}\|_2^2 + \frac{1}{L^{2\alpha}} \|\Delta W^{(\ell)} \phi(h^{(\ell-1)})\|_2^2} \tag{84}$$

for various depths and iteration steps, where the weights are updated with Scion.

We also report

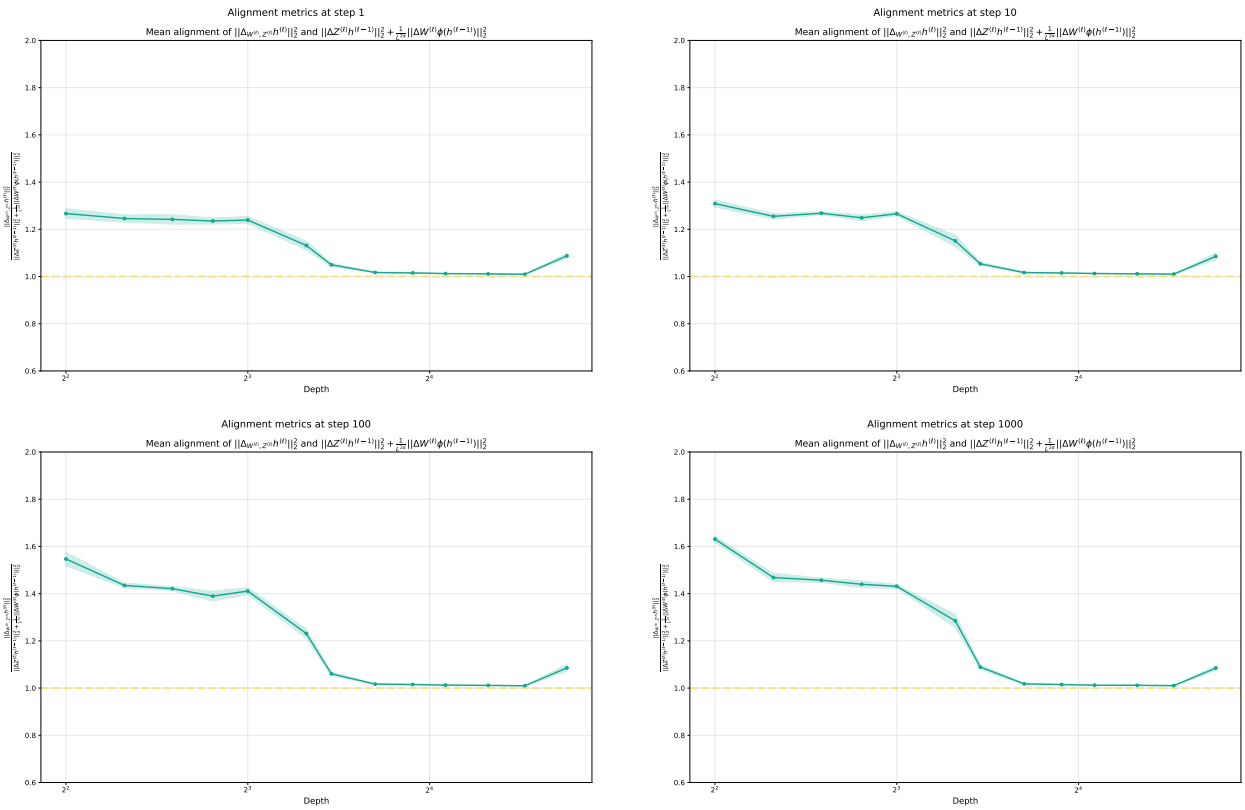


Figure 28: Alignment of the update of the hidden features $\Delta_{W^{(\ell)},Z^{(\ell)}} h^{(\ell)}$ with the sum of the updates applied to the layer ℓ, across a wide range of depths L, on CIFAR-10. Despite the non stability we observe at small depth, we still note that the ratio is always above 1, which empirically show that the lower bound holds. The network is a ResNet where we learn the matrices $Z^{(\ell)}$, trained with Unconstrained Scion, on CIFAR-10, on 5 trials. The layer of interest here is the third hidden layer. Experimental details can be found in Table 7.

$$\text{and} \quad \frac{\|\Delta W^{(\ell)}\phi(h^{(\ell-1)})\|_2^2}{\|\gamma * W^{(\ell)}\phi(h^{(\ell-1)})\|_2^2 + \|\gamma \operatorname{lmo}(M_t^{W^{(\ell)}})\phi(h^{(\ell-1)})\|_2^2} \\ \frac{\|\Delta Z^{(\ell)} h^{(\ell-1)}\|_2^2}{(\|\gamma_Z * Z^{(\ell)} h^{(\ell-1)}\|_2^2 + \|\gamma_Z \operatorname{lmo}(M_t^{Z^{(\ell)}})h^{(\ell-1)}\|_2^2}. \tag{85}$$

H.5 Alignment of the updates of the layer with Scion for the width transfer

In Figure 30, we study the non-cancellation properties of the updates of Scion, as we scale the width of the MLP. We report:

$$\frac{\|\Delta h^{(\ell)}\|_2^2}{\|\Delta W^{(\ell)}\phi(h^{(\ell-1)})\|_2^2 + \|W^{(\ell)}\Delta\phi(h^{(\ell-1)})\|_2^2 + \|\Delta W^{(\ell)}\Delta\phi(h^{(\ell-1)})\|_2^2}, \tag{86}$$

for various network widths and iteration steps t, where the weights are updated with Scion.

We also report the alignment of the current quantities with the update,

$$\frac{\|-\gamma W^{(\ell)} + \gamma \operatorname{lmo}(M_t^{(\ell)})\|_{\mathcal{S}_\infty}^2}{\|\gamma W^{(\ell)}\|_{\mathcal{S}_\infty}^2 + \|\gamma \operatorname{lmo}(M_t^{(\ell)})\|_{\mathcal{S}_\infty}^2}. \tag{87}$$

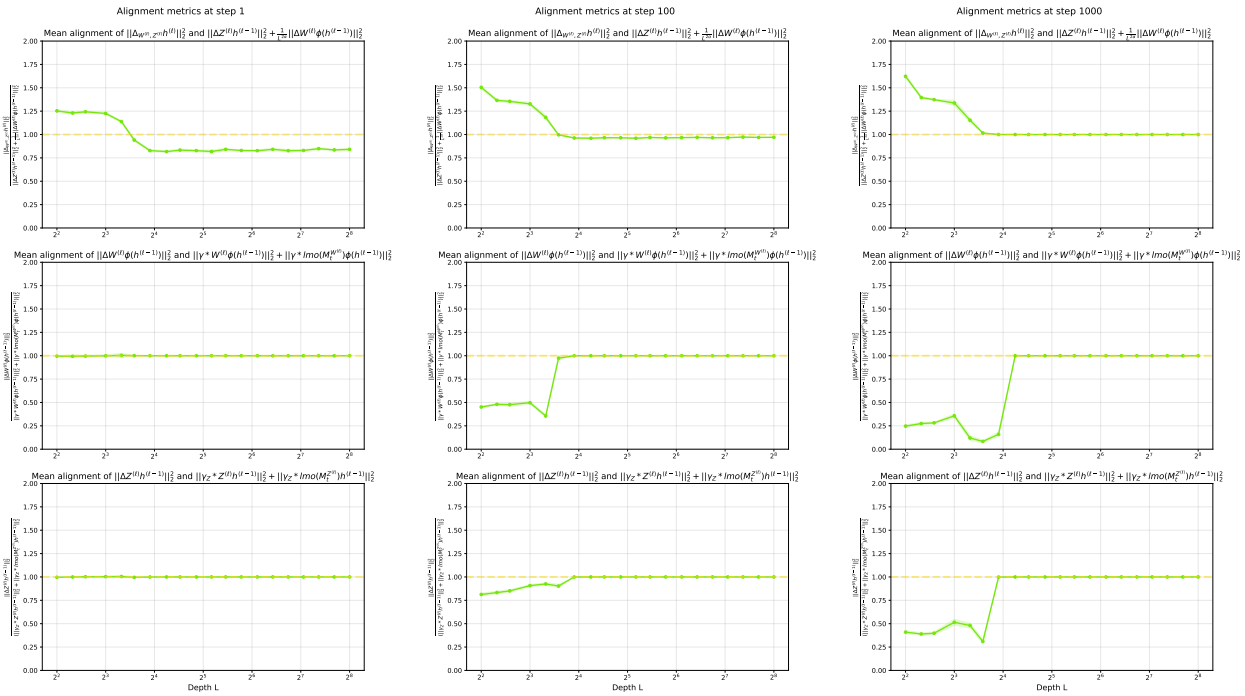


Figure 29: *First row:* Alignment of the update of the hidden features $\Delta_{W^{(\ell)},Z^{(\ell)}} h^{(\ell)}$ with the sum of the updates applied to the layer ℓ, across a wide range of depths L, on CIFAR-10. *Second row:* Alignment of the update of $W^{(\ell)}$ with the sum of the current $W^{(\ell)}$ and $\mathrm{lmo}(M_t^{W^{(\ell)}})$. *Third row:* Alignment of the update of $Z^{(\ell)}$ with the sum of the current $Z^{(\ell)}$ and $\mathrm{lmo}(M_t^{Z^{(\ell)}})$. Despite the non stability we observe at small depth, we still note that the ratio stabilizes at larger depth to a constant close to 1, which empirically show that the alignment is a reasonable assumption. The network is a ResNet where we learn the matrices $Z^{(\ell)}$, trained with Scion, on CIFAR-10, on 5 trials. The layer of interest here is the third hidden layer. Experimental details can be found in Table 7.

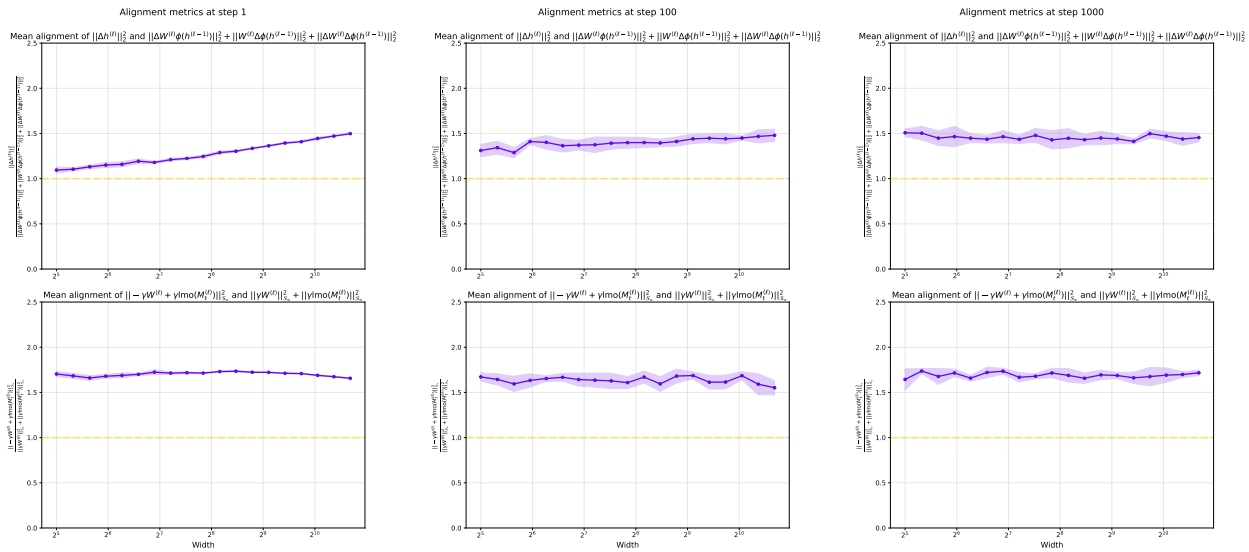


Figure 30: *First row:* Alignment between the update of the hidden features $\Delta h^{(\ell)}$ and the three terms appearing from the update of $W^{(\ell)}\phi(h^{(\ell-1)})$, across a range of network widths, on CIFAR-10. *Second row:* Alignment between the update of $W^{(\ell)}$ and the sum of the squared spectral norms of $W^{(\ell)}$ and the corresponding lmo. The network is an MLP trained with Scion on CIFAR-10, over 5 trials. The layer of interest is the second hidden layer. The plots are shown at different training steps and across a wide range of network widths. Experimental details can be found in Table 8.